Corrosion and Corrosion-Fatigue Behavior of 7075 Aluminum Alloys Studied By *In Situ* X-Ray Tomography

by

Tyler Stannard

A Dissertation Presented in Partial Fulfillment
of the Requirements for the Degree
Doctor of Philosophy

Approved October 2017 by the
Graduate Supervisory Committee:

Nikhilesh Chawla, Chair
Kiran Solanki
Ramasis Goswami
Yongming Liu

ARIZONA STATE UNIVERSITY
December 2017

ABSTRACT

7XXX Aluminum alloys have high strength to weight ratio and low cost. They are used in many critical structural applications including automotive and aerospace components. These applications frequently subject the alloys to static and cyclic loading in service. Additionally, the alloys are often subjected to aggressive corrosive environments such as saltwater spray. These chemical and mechanical exposures have been known to cause premature failure in critical applications. Hence, the microstructural behavior of the alloys under combined chemical attack and mechanical loading must be characterized further. Most studies to date have analyzed the microstructure of the 7XXX alloys using two dimensional (2D) techniques. While 2D studies yield valuable insights about the properties of the alloys, they do not provide sufficiently accurate results because the microstructure is three dimensional and hence its response to external stimuli is also three dimensional (3D). Relevant features of the alloys include the grains, subgrains, intermetallic inclusion particles, and intermetallic precipitate particles. The effects of microstructural features on corrosion pitting and corrosion fatigue of aluminum alloys has primarily been studied using 2D techniques such as scanning electron microscopy (SEM) surface analysis along with post-mortem SEM fracture surface analysis to estimate the corrosion pit size and fatigue crack initiation site. These studies often limited the corrosion-fatigue testing to samples in air or specialized solutions, because samples tested in NaCl solution typically have fracture surfaces covered in corrosion product. Recent technological advancements allow observation of the microstructure, corrosion and crack behavior of aluminum alloys in solution in three

dimensions over time (4D). *In situ* synchrotron X-Ray microtomography was used to analyze the corrosion and cracking behavior of the alloy in four dimensions to elucidate crack initiation at corrosion pits for samples of multiple aging conditions and impurity concentrations. Additionally, chemical reactions between the 3.5 wt% NaCl solution and the crack surfaces were quantified by observing the evolution of hydrogen bubbles from the crack. The effects of the impurity particles and age-hardening particles on the corrosion and fatigue properties were examined in 4D.

DEDICATION

I dedicate this dissertation to everyone who has shown tremendous faith in me by funding my educational endeavors for the last 8 years. Without all of you this would not have been possible.

This includes my parents Christopher Stannard and Heather Spencer, my grandparents Robert and Angela Stannard, and my aunt Elizabeth Mercado. I dedicate this to William and Mary Dyrkacz and ASM International for creating the William and Mary Dyrkacz materials engineering scholarship. I dedicate this to the Engineers Club of the West Valley for their scholarship provided through Glendale Community College. I dedicate this to Dr. Mary Anderson-Rowland for creation of the Motivated Engineering Transfer Students' center at Arizona State University which provided scholarships and valuable career resources. I dedicate this to the Science Foundation Arizona for their fellowship which paid me taught me in detail about scientific community outreach. I also dedicate this to the Taxpayers of the United States via the Federal Government, the National Science Foundation and the Department of Defense Office of Naval Research for funding basic research.

ACKNOWLEDGMENTS

I thank Professor Nikhilesh Chawla for continued guidance and support. It has been a pleasure working under his tutelage. In addition to his mentorship, Dr. Chawla has given me access to valuable research facilities and helped me to win three different prestigious fellowships. Dr. Chawla also supports me by encouraging me when I am facing difficulties in my research. I wish to thank the members of my dissertation committee, Dr. Ramasis Goswami, Dr. Yongming Liu, and Dr. Kiran Solanki, for examining my research and providing useful feedback. I thank Dr. Jason Williams for the numerous technical insights and assistance he has provided, which were invaluable in carrying out this research work. I thank Dr. Sudhanshu S. Singh for his advice in research and Dr. James Mertens for his instruction regarding X-ray tomography. I thank Dr. Hrishikesh Bale with his assistance in diffraction contrast tomography imaging. I thank Dr. X. Xiao and Dr. F. De Carlo for their guidance and assistance in X-Ray tomography research at the 2BM X-Ray Synchrotron Tomography facility at Argonne National Laboratory.

I am grateful for financial support for this work granted by the Office of Naval Research under grant N000141010350. I thank the National Science Foundation for their generous grant from the Graduate Research Fellowship program for financial support of my Ph.D. work. I gratefully acknowledge the use of facilities within the Center for Solid State Science at Arizona State University and the Center for 4D Materials Science. I thank the Chawla research group members for their assistance and friendship in this

research. I thank my family, friends and fiancée for their emotional and financial support in this research.

This research used resources of the Advanced Photon Source, a U.S. Department of Energy (DOE) Office of Science User Facility operated for the DOE Office of Science by Argonne National Laboratory under Contract No. DE-AC02-06CH11357. This material is based upon work supported by the National Science Foundation under Grant No. DGE 1311230. Any opinions, findings, and conclusions or recommendations expressed in this material are those of the author and do not necessarily reflect the views of the National Science Foundation.

TABLE OF CONTENTS

Page

LIST OF TABLES

Table Page

LIST OF FIGURES

Figure Page

Figure Page

Figure Page

Figure Page

Figure Page

Figure Page

Figure Page

Figure Page

Figure Page

Figure Page

1 INTRODUCTION

Corrosion-related failures of metal components costs about $2.2 trillion dollars or 3% of the worldwide gross domestic product annually [1]. Considering the majority of aircraft component failures are due to corrosion and fatigue-related failures, there is a tremendous need for research to prevent these failures [2–5]. Many corrosion and fatigue failure-prone aircraft components such as fuselage, wings, and supporting structures are made of aluminum alloys. The aluminum alloys were chosen for numerous reasons including their high strength-to-weight ratio, low raw material costs, and low machining costs [6]. Specifically, the 7XXX-series aluminum alloys may be the most ubiquitous of the high strength alloys due to its relatively low cost. One common application of 7XXX-series aluminum alloys is for components in aircraft which are deployed from aircraft carriers in the ocean. Such environments have caused numerous component failures due to the high stress loading during exposure to aggressively corrosive saltwater ocean spray.

Many studies have been performed to improve failure modelling and alloy design capabilities. In fact, fatigue studies of 7075-T6 alloy have been found from as early as 1944 [7]. Most of the studies to date have used two dimensional (2D) techniques to observe the failure mechanisms. While these studies have elucidated many aspects of the material microstructure and its effects on failure phenomena, there are still many aspects of the failure mechanisms which would need to be characterized *in situ* in three dimensions or more for truly comprehensive confirmation. As recently as 1999, nondestructive 3D techniques have enabled the study of material microstructure and

failure phenomena [8]. Within the last ten years, X-ray tomography studies of fatigue in noncorrosive environments have quantified the effects of inclusion particles on the fatigue crack growth rate [9–14]. Stress corrosion cracking and corrosion fatigue tests have shown hydrogen bubbles within the cracks [15–18]. Examinations of corrosion pits in 3D have shown the progress of corrosion in 2024 and 7050 aluminum alloys [19–21].

Therefore, *in situ* 3D X-ray tomography was chosen as the primary method to investigate the effects of microstructural features on corrosion-pitting and corrosion fatigue with a focus on the inclusion particles and precipitates. Furthermore, post-mortem focused ion beam analysis was used to verify the inclusion corrosion. Follow-up studies using a novel technique called laboratory-based X-ray diffraction contrast tomography was used to determine the effects of grain boundary positions and orientations in 3D. An additional technique called vertical-scanning light interferometry was used to view the corrosion initiation effects in 2D at nanometer resolution. Together, these combined studies have created a more complete understanding of the effects of each major microstructural feature in 7XXX aluminum alloys including inclusions, precipitates, dispersoids, grain orientations, and grain boundaries.

2 LITERATURE REVIEW

2.1 Aluminum Alloys

7XXX Aluminum alloys have high strength to weight ratio and low cost. They are used in many critical structural applications including automotive and aerospace components, including aircraft wings and fuselage. Many varieties of aluminum alloys

are in use, including 2XXX, 5XXX, 6XXX and 7XXX series. Each alloy uses different alloying elements for strengthening the generally weak, but low-density aluminum metal. The 7XXX series has the highest strength, generally on the order of 400 – 500 MPa. 7XXX alloys are wrought product which are extruded into shape during solidification, then precipitation heat treated for strength.

2.1.1 Second Phase Particles in 7XXX-Series Aluminum Alloys

In 7XXX alloys the solidification step allows formation of constituent particles of varying compositions including inclusions, dispersoids and precipitates. Each type of particle has significant effects on the metallurgical performance. 7XXX-TXXX is the typical nomenclature for an individual alloy type. The numbers in the 7XXX designation represent slight variations in chemical composition of different, but similar alloy types strengthened with Mg, Zn, and Cu as the primary elements for precipitation strengthening intermetallic particles, while the numbers in the -TXXX designation represent the heat treatment procedures used to strengthen the alloys [22].

Inclusions in 7XXX alloys are nuisance impurity particles which solidify from the melt before the metal matrix. The inclusion particles are present due to the presence of Si and Fe impurities which are not easily soluble in the alloy and are expensive to remove [23]. These particles are on the order of 10s of microns and have significant effects on the alloy damage properties [12]. Two of the most common inclusion types in 7XXX alloys are Mg_2Si, Al_7Cu_2Fe [24–26].

Additionally, particles on the order of 0.2 – 0.5 um called dispersoids solidify before the grains and serve to maintain a small grain size in the alloy by preventing recrystallization after hot rolling. These particles form by prompt reaction between the aluminum and transition metals such as chromium, manganese, or zirconium to form relatively insoluble phases [27]. Dispersoids in 7075 are typically $Al_{12}Mg_2Cr$ or Al_7Cr. [26]. The grain refinement caused by the dispersoids serves to strengthen the alloy by the Hall-Petch relationship [28].

Precipitation hardening is the primary mechanism used for strengthening of aluminum alloys. Only alloy systems with significant maximum solubility limits on the order of several percent, in addition to a rapid decrease in solubility with decreasing temperature can be strengthened by precipitation hardening. The precipitation hardening procedure involves heating the alloy to a temperature at which the alloying elements are uniformly distributed as a single phase, followed by a rapid quenching to secure a metastable single-phase state. Next, the alloy is heated to a lower temperature at which the second phase alloying elements precipitate out as uniformly distributed second phase particles. These intermetallic particles serve to strengthen the alloy by limiting the slip of dislocations during plastic deformation. When the particles initiate, they are too small to prevent the dislocation motion. As the particles grow, they reach a point of maximum strength improvement at which they are semicoherent with the surrounding crystal lattice, resulting in stress surrounding the particle. At this point, some of the particles pin the dislocations while others are sheared. As the aging continues, the particles become incoherent with the surrounding lattice and at that point, the dislocations can only be

pinned or form loops upon deformation and thus their strengthening capabilities are reduced. The precipitates in 7XXX alloys consist of $Mg(Cu_xZn_{1-x})_2$ with exact composition and structure in the face-centered cubic matrix changing dependent upon aging condition. The general structure of the precipitates changes during heat treatment from coherent GP zones for the under-aged condition to semi-coherent η' for peak-aged, to incoherent hexagonal closed-packed η for the over-aged condition [29–31]. -T6XX tempers represent peak-aged alloys while -T7XX tempers represent over-aged alloys. -TX51 tempers of the 7XXX alloys are stretched by 1 to 5% to reduce residual stress gradients within the plate and create more sites for earlier precipitate nucleation, especially at grain boundaries [32].

2.2 Corrosion Behavior of 7XXX Series Aluminum Alloys

Aluminum rapidly passivates at room temperature within a millisecond of exposure to oxidizing environments such as water or air to form a protective oxide film 2 – 4 nm thick, with the thickness dependent upon temperature [33]. These alloys are particularly susceptible to corrosion in chloride-containing solutions such as seawater, because the chloride ions in solution can rapidly break down thinner regions of the passive layer, leading to corrosion pitting in localized regions [34–37].

The film-breaking mechanism is the primary mechanism of corrosion pit initiation in nearly neutral pH chloride-containing solution. The film breaking mechanism suggest that chloride ions adsorb on and weaken the passive film, followed by the Cl^- and H^+ ions reacting with the underlying substrate, ultimately leading to preferential corrosion pitting

and subsequent reduction of pH within the pit due to high concentrations of aluminum corrosion byproducts [35–39]. The chemical reactions which can occur to cause dissolution of the aluminum metal are described below. Generally, the bare metal at the tip of a pit or crack in a neutral or slightly alkaline solution oxidizes [39]. For low local chloride ion concentrations, the aluminum reacts with the water in solution to form H^+ and Al_2O_3:

$$\mathbf{Al + 3H_2O \rightarrow Al_2O_3 + 6H^+ + 6e^-} \quad (1)$$

For chloride concentration at or above 1 M, the chlorine has been proposed to interact with the Al^{3+} from (1) to undergo hydrolysis [37,40]:

$$\mathbf{Al^{3+} + H_2O \longleftrightarrow Al(OH)^{2+}} \quad (2)$$

In which case, aluminum hydroxide would then react with chloride:

$$Al(OH)^{2+} + Cl^- \rightarrow Al(OH)Cl^+ \quad (3)$$

Next, the chloride compound would react with water to produce local acidity:

$$Al(OH)Cl^+ + H_2O \longleftrightarrow Al(OH_2)Cl + H^+ \quad (4)$$

Al(OH)Cl and $Al(OH)_2Cl_2$ compounds have been observed at the tips of pits in pure Al in 1 M NaCl solution of pH 11 using nuclear magnetic resonance spectroscopy. The local pH at the pit tip was ~3, which was in agreement with the pH of bulk aluminum hydroxide salt solutions [38]. $AlCl_3$ has also been theorized to form, but this may be more probable in highly acidic solutions or solutions near the ~5 M saturation point of NaCl in H_2O since the $AlCl_3$ is highly acidic, with a pH around -0.3 [37,41,42]. Additional solid byproducts caused by the corrosion of the aluminum are created by ionization of the bare surface and rapid hydrolysis of aluminum to form Al_2O_3, $Al(OH)_3$ and $Al(OH)_2Cl$

byproducts, which have a larger volume than the original Al matrix and lead to a thick, cracked oxide on heavily corroded surfaces [37,40]. The film breaking mechanism serves as a good explanation for corrosion pit initiation and growth, but further research is needed to find why corrosion pits only occur in selected locations, such as certain inclusions on the alloy surface but not others.

Defects in the passive layer as well as differences in chemical composition of inclusions, precipitates, pores and grain boundaries relative to the matrix are known to affect the corrosion properties in aluminum alloys because they serve as inhomogeneous sites with a weakened passive layer [15,31,35,37,43–51]. For instance, corrosion pitting is believed to occur semi-randomly on the surface of the alloy at Fe-rich and Mg-rich impurity particles called inclusions [35,37,43,47,48,52–57]. The Mg- and Fe-rich intermetallic impurity particles in 7075 Al alloys cause the formation of corrosion pits because they have different chemistry leading to differences in electrochemical potential from the surrounding matrix an can occasionally cause defects in the passive layer which promote faster corrosion [12,54,55,58]. Mg-bearing inclusions such as Mg_2Si are initially anodic with respect to the matrix, with Mg preferentially dissolving from the matrix followed by the remaining Si becoming cathodic with respect to the matrix and forming a pit [56]. In Mg_2Si, the corrosion reaction occurs first by dissolution of the Mg from the Mg_2Si particle, followed by enhanced dissolution of the matrix surrounding the cathodic Si-rich remnant which remains in the matrix [53]. The overall corrosion reaction expected for dissolution of Mg is expected to be [59],

$$\mathrm{Mg} + 2\mathrm{H_2O} \rightarrow \mathrm{Mg(OH)_2} + 4\mathrm{H^+} + 4e^- \quad (2)$$

The Fe-bearing inclusions such as Al_7Cu_2Fe are noble and have a higher corrosion potential compared to the matrix, leading to preferential corrosion of the matrix surrounding the inclusions [49,54,55,60].

Additionally, the structure and chemistry of the precipitates affects the corrosion behavior in 7xxx alloys [49,55]. Focused-ion-beam tomography observations of precipitates in 7075 alloy have suggested that larger precipitates form at grain boundaries and inclusions than within the bulk alloy because they are heterogeneous sites with decreased activation energy for precipitate nucleation during hardening heat treatments [35,61,62]. These larger precipitates can have different chemistry and structure than the smaller precipitates within the grains [31,44]. For instance, in alloys in the over-aged condition, larger η precipitates with increased copper content have been observed versus standard peak-aged alloy at both the bulk and grain boundaries of the alloy [31,63]. Therefore, the confluence of grain boundaries and inclusions may serve to form precipitates which are much larger than the surrounding bulk, leading to areas of significantly different electrochemical potential, a wider precipitate-free zone, and a weakened passive layer where corrosion can occur at a much higher rate than the surrounding grains [48,64,65].

Some studies have also investigated grain size and orientation effects on corrosion properties. For instance, recent studies of corrosion in high purity aluminum and natural-aged aluminum alloy of varying grain sizes has suggested that corrosion rate decreases with decreasing grain size [57,66], which may be due to larger, more heterogeneous particles form at the grain boundaries. Nonetheless, when the alloys are heat-treated, the

precipitates can grow and subsequently alter the pit growth-precipitate relationships. Therefore, the over-aged alloys can exhibit exacerbated corrosion near grain boundaries versus the peak-aged alloys [35,48,64,65,67]. Additionally, studies of single crystal Al-Cu alloys have suggested that increasing alloying element concentration leads to decreased crystallographic effects on corrosion rates and morphology within the grains [68,69].

2.3 Mechanisms of Corrosion Fatigue

7075 Al alloys are susceptible to damage by corrosion pitting which can reduce the fatigue resistance of the material [70–72]. Additionally, in the peak-aged condition 7075 alloys suffer a significant reduction in resistance to environmentally assisted cracking, which has been attributed to hydrogen embrittlement [73,74]. Local interactions of the matrix with the anodic Mg_2Si inclusion particles or the cathodic Al_7Fe_2Cu inclusion particles at the areas of weakened passive film also serve to accelerate the corrosion locally, causing pit formation and subsequent fatigue life reduction [75].

Most studies of corrosion-fatigue have examined used bulk measurement techniques such as extensometers to measure crack growth, followed by post-mortem fractography [76,77]. The mechanism for corrosion fatigue is believed to be dominated by adsorption of hydrogen at the crack tip during cyclic loading assisting leading to emission of dislocations and promoting localized cleavage fracture [78–81]. Changes in crack tip pH and local electrochemistry have also been measured *in situ* using bulk techniques to improve understanding of corrosion cracking mechanisms [82–84]. These studies have

confirmed that the solution pH of the crack tips stabilizes at a value of approximately 3.5 for monotonic loading, but in corrosion fatigue the cyclic loading may prevent equilibrium conditions from occurring due to "pumping" of the solution from the crack tip at the bottom of the load [83,84]. The pH=3.5 is assumed to come from dissolution of the aluminum matrix to increase the concentration of Al^{3+} ions and possibly $Al(OH)_3$ solubility products within the crack tip leading to increased $[H^+]$ in solution. While measuring the pH in the tip of a small corrosion fatigue crack is currently difficult, observation of the bubbles may also provide insights regarding localized corrosion in the crack tip. For instance, one indicator of hydrogen evolution is gas bubbles which evolve during the corrosion reactions.

The inclusions in aluminum alloys have a significant effect on fatigue behavior. Typically, fatigue cracks in air initiate at the Fe-bearing inclusions [85–87]. Thus, the purity of the aluminum alloy can have a significant effect on the fatigue strength and fracture toughness. For instance, Alcoa 7475 has a lower concentration of inclusion elements than 7075 by a factor of 4, with the rest of the alloying elements having very similar concentrations, yielding an approximately 40% greater fracture toughness [88,89].

Most studies of corrosion pitting in Al7075 have used two dimensional methods, such as area measurement of the pit on the corroded surface [70] or depth measurement via examination of the fracture surface [58,90–92]. Efforts to measure pit structure effect on fatigue, such as post-mortem SEM studies of the fracture surface [58,90–92] and confocal microscope analysis of the corrosion pits [93], have demonstrated that the shape of the corrosion pit affects the fatigue crack initiation life.

For 7075 samples corroded in 3.5 wt% NaCl, the tendency for fatigue crack initiation in air from pits, inclusions, or other matrix flaws has been observed to change with aging condition: peak-aged samples have mixed crack initiation sites and overaged samples have a greater tendency for fatigue crack initiation at the pits [70,71]. For samples corroded and tested in NaCl solution, the cracking mechanism may occur by a combination of anodic slip dissolution and hydrogen embrittlement [64,94].

Since the solubility of hydrogen in aluminum is low, with concentrations of 3000 ppm or less resulting after various high fugacity hydrogen charging methods in pure Al foils, relatively few of the H^+ ions must enter the metal for embrittlement to occur [95,96]. However, high entropy sites such as grain boundaries, precipitates, and inclusion may alloy alloyed aluminum to absorb more hydrogen. The change in preferred crack initiation site with respect to aging condition may be due to an increased effect of hydrogen embrittlement for peak-aged alloy versus over-aged alloy [65,70].

2.3.1 Hydrogen Environment Embrittlement Mechanisms

The three most relevant mechanistic theories of environmental hydrogen embrittlement are hydrogen-enhanced decohesion (HEDE), hydrogen-enhanced localized plasticity (HELP), and adsorption-induced dislocation emission (AIDE) [79,97]. HEDE was the first hydrogen embrittlement theory to emerge, proposing that the hydrogen atoms move into the lattice and weaken the interatomic bonds. HEDE was developed to explain the change from ductile fracture to brittle cleavage fracture in iron upon addition of hydrogen environment [98–101]. HELP theory suggests that solute hydrogen promotes

deformation by assisting dislocation motion when a sample is loaded in a hydrogen-containing environment [102]. Hydrogen's facilitation of dislocation motion was proven in aluminum and other metals using *in situ* environmental TEM loading in H_2 atmosphere, with one caveat that the high energy electron beam drastically increased the fugacity of the hydrogen at the specimen beyond by several orders of magnitude, far beyond tests in high pressure hydrogen without an electron beam [103–106]. AIDE suggests that adsorption of embrittling atomic species on fresh metal crack surfaces causes emission of dislocations; [107,108]. The differences in cracking between different precipitate sizes of aluminum may be explained by the HELP mechanism of hydrogen embrittlement.

The increase in crack initiation sites for peak-aged alloy may be due to a more pronounced effect of the hydrogen-enhanced localized plasticity (HELP) mechanism. Experimental observations and modelling of the HELP mechanism suggest that hydrogen atoms in aluminum bind to edge dislocation cores in the lattice, forming dilatational fields around the cores which improve dislocation mobility and reduce partial separation distances, causing slip planarity and shear localization [109–112]. The HELP mechanism reduces the repulsive forces between dislocations and precipitates due to the shielding of the dislocation core by solute hydrogen, allowing for pileups to form at precipitates under lower stress [113]. This phenomenon may be evident in the change in SCC slip mode of aluminum alloys from sharp crack tip planar slip in under-aged and peak-aged alloys to blunt crack tip wavy slip in overaged alloys [114]. In the peak-aged condition 7XXX alloys suffer a significant reduction in resistance to environmentally assisted cracking,

which has been attributed to hydrogen embrittlement [115,116]. Edge dislocation pileups can possibly shear coherent precipitates or be pinned for peak-aged alloys, while in the overaged alloys where dislocations would have to travel around incoherent precipitates.

2.3.2 Anodic Dissolution

Anodic Dissolution is a corrosion mechanism of alloys in solution which occurs by ionic transport between conductive elements of different corrosion potentials in the submersed alloy [117,118]. Anodic dissolution occurs between conductive materials in a conductive solution. Hence, anodic dissolution can occur between the matrix and the second-phase particles if they are exposed to the solution [117,119]. Anodic dissolution is especially prominent in NaCl solution because the Cl^- ions are believed to weaken or disrupt the native oxide layer of the aluminum and allow for reaction of the matrix with the aggressive ions in solution via the anodic dissolution mechanism [36,37,119–122]. When stress is applied, anodic slip dissolution can occur. In the case of anodic slip dissolution, the stress causes slip, which ruptures the passive film at the crack tip and further facilitates access of corrosive ions to the bare metal surfaces [123,124].

For corrosion-fatigue in 7XXX aluminum alloys, the change in mechanism has been suggested to go from hydrogen embrittlement dominance, to a mixed mode for overaged, to anodic dissolution for highly overaged [65]. The change in precipitate size and chemistry, as well as the reduced crack tip sharpness in overaged alloys can cause the anodic dissolution mechanism to dominate the corrosion and cracking properties of the alloys when highly overaged [65].

2.3.3 Effects of Pits on Fatigue in Aluminum

7XXX alloys are susceptible to damage by corrosion pitting which can reduce the fatigue life of the materials [58,70,72]. Most studies of corrosion pits' effect on crack growth in Al 7075 have used two dimensional methods, such as optical measurement [70], confocal microscopy, and scanning electron microscopy to study damage post-mortem [71,90,92]. Efforts to measure pit structure effects on fatigue, such as post-mortem scanning electron microscopy (SEM) of the fracture surface [71,90–92] and confocal microscopy analysis of the corrosion damage [93,125], have suggested that the shape of the corrosion damage affects the fatigue crack initiation life more than the depth of the corrosion damage alone. Specifically, cross-sectional pit analysis and fractography of the corrosion-fatigue initiation of corroded aluminum alloys have suggested that sharp protrusions in localized regions of the pit can lead to regions with sufficient stress to create localized plasticity at the pit tip and thereby initiate cracks within fewer cycles [75,92,125]. These local protrusions can be associated with the corrosion product shape. Additionally, multiple fatigue crack initiation sites have been observed from fractography of corrosion pitted aluminum alloys, meaning the existence of multiple pits may lead to synergistic activity between pits in crack initiation and growth since [70,77,126,127].

Corrosion damage is a frequent initiation site for fatigue crack initiation [2,4,75,128]. This is due to the stress concentration caused by the morphology of the corrosion damage.

2.4 Motivation: 3D *In Situ* Studies of Environmentally Damage

Recently, X-ray tomography has emerged as an excellent technique to understand microstructural damage mechanisms in three dimensions (3D). *In situ* synchrotron X-ray tomography has been used to view many damage phenomena in aluminum alloys. *In situ* fatigue tests have shown that 3D tomography provides reliable measurements of local crack growth rates and quantified the effects of second phase particles on local crack growth rates [8,129,130]. *In situ* corrosion-fatigue testing has demonstrated the value of tomography by showing relationships between hydrogen bubbles and corrosion on the fracture surfaces [17,131–134]. *In Situ* observations of stress corrosion cracks of sensitized 7075 in moist air have shown that the embrittling environments can lead to jagged cracks which would not be measured accurately using traditional 2D techniques such as optical microscopy [18]. Both *In situ* and e*x situ* studies of crack growth from pitting corrosion in steels using X-ray tomography have directly shown that pits had distinctly different geometries such as bullet-shaped and hemispherical shapes which determined whether the stress corrosion crack initiated at the tip of the deepest intrusion of the pit or the opening of the pit [135–137].

Based on the wealth of evidence suggesting the utility of *in situ* tomography for the observation of corrosion and cracking analysis, useful information can be gained by examining the corrosion-fatigue cracking of pitted aluminum alloys using tomography. Most observations of aluminum alloys have examined corrosion pitting and cracking using 2D techniques. One limitation of 2D techniques is the pits are filled with the corrosion products [37,40] which can serve to obscure the optical measurements. Hence,

important mechanistic insights could be missed, such as the difference in 3D shape between pits which reach the fracture surface and those which do not fracture. An aggressive acidic wash has been suggested [138] to clean the corrosion product before corrosion damage analysis, but this may undesirably change the corrosion morphology in a way that effects subsequent fatigue properties, or cause increased embrittlement of the remaining matrix material. Using post-mortem fractography, only the pits which reach the fracture surface are observable, but the pits which do not reach the fracture surface may also be of interest for failure modelling purposes.

Moreover, when aluminum alloys are fatigue tested in corrosive fluid, information obtained *via* fractography can be limited due to corrosion of the crack faces during crack growth [56,139]. This is an especially significant problem for samples tested in 3.5 wt% NaCl solution, where the corrosion damage can proceed to cover most of the fracture surface and reduce the accuracy post-mortem analyses such as striation spacing measurements. Furthermore, the corrosion pit shape may be more important than the number of pits, and therefore highly accurate three dimensional assessments of pit shape are required to understand fatigue crack initiation life in these corroded 7075 alloys [90,92] since existing studies can only gain 3D assessments of pit shape for pits which reach the fracture surface. Confirmation of insights regarding corrosion cracking in aluminum via 3D nondestructive techniques such as X-ray tomography serves to improve the accuracy of future 2D nondestructive testing analysis for modelling the effects of corrosion damage on fatigue life.

Pit initiation and growth has been observed using X-ray tomography [19,20,140], but fatigue crack initiation from corrosion pits has not yet been analyzed using *in situ* X-ray tomography. A 3D technique such as X-ray tomography is required to analyze the pit depth and shape comprehensively in a sample region nondestructively to determine the fatigue crack growth initiation properties [19,20]. In fact, recent 3D examinations and modelling of 3D pit morphology in steels has shown that pits have different shapes yielding different stress concentrations [135,137,141].

For fatigue tests of aluminum alloys in corrosive fluid, information obtained via fractography can be limited due to corrosion of the crack faces during crack growth. This is an especially significant problem for samples tested in 3.5 wt% NaCl solution, where the corrosion damage, or "mud-cracking" can proceed to cover the fracture surface and prevent post-mortem analysis. Moreover, for pre-corroded samples, sample characterization before testing is even more difficult since the thick corrosion product layer is significantly rougher than the polished surface, and its insulating properties lead to poor quality images in the SEM due to sample charging. Furthermore, the corrosion pits are filled with the corrosion products [37,40], which can serve to complicate pit depth analysis.

To complicate matters even more, round test specimens, which are very convenient to machine, can pose significant difficulties for crack growth rate measurements, since the crack depth must be inferred from the half-arc length using finite-element calculations, direct current potential drop measurements, or post-mortem

fracture surface striation measurements. The work herein demonstrates a fast method for a more complete understanding of the crack geometry of relatively small cylindrical samples using 3D X-ray tomography.

High resolution synchrotron X-Ray tomography can be used *in situ* to perform 3D nondestructive studies of corrosion fatigue crack growth in aluminum alloys. High resolution synchrotron X-Ray tomography can be used *in situ* to perform 3D non-destructive studies of corrosion fatigue crack growth in aluminum alloys. *In situ* synchrotron tomography has been used to view the damage evolution of tensile loading [8,129,142–144], corrosion [19,20], fatigue [10,130,145,146], corrosion fatigue [16,17,131,134], and stress corrosion cracks [15,17,18,147] in aluminum alloys. These experiments have provided useful insights regarding aluminum alloy damage evolution [10,148], such as showing how cracks propagate through the matrix and impurity inclusion particles, how corrosion pits form, and how crack growth in solution leads to chemical reactions [8,18–20,129–131,134]. Therefore, the primary techniques used in this study relied on nondestructive 3D X-ray tomographic methods to study the corrosion and corrosion-fatigue properties of

3 3D TIME-RESOLVED OBSERVATIONS OF CORROSION DURING FATIGUE CRACK INITIATION AND GROWTH FROM A CORROSION PIT IN PEAK-AGED AL7075 USING SYNCHROTRON X-RAY TOMOGRAPHY

3.1 Introduction

This work presents, for the first time, a thorough analysis of crack initiation at corrosion pits, followed by corrosion-fatigue crack propagation in 7075 aluminum (in 3.5 wt. % NaCl solution) using *in situ* X-ray tomography. The real-time experiments allowed us to understand the effects of corrosion pit formation, followed by the effect of surrounding inclusions and microstructure on dissolution, hydrogen bubble formation, and its effects on subsequent fatigue crack growth. These experiments were combined with scanning electron microscope focused ion beam (FIB-SEM) cross-sectioning and EDS analysis to obtain a complete picture of microstructural effects on corrosion-fatigue damage.

3.2 Materials and Methods

Blocks were cut from commercially available Al 7075-T651 (5.63 Zn, 2.45 Mg, 1.55Cu, 0.045 Si, 0.18 Fe, 0.008 Mn, 0.19Cr, 0.004 Ni, 0.049 Ti, and rest Al) about 7.6 cm in thickness (Alcoa, New York, NY). The blocks were solution treated at 510^{o}C for 2 hours, water quenched, and then rapidly placed into a furnace at 120 ^{o}C for 24 hours to obtain the peak-aged condition (Vickers hardness of ~170 HV). The sample geometry for *in situ* fatigue testing, shown in Figure 1, was cut from heat-treated blocks using electrodischarge machining (EDM), while the gauge section was milled using low stress grinding.

The sample gauge section was carefully polished to a 1 μm diamond finish, sonicated for 30 seconds in acetone, then rinsed in deionized water, and dried. Masking tape was applied to the center 1 mm of the gauge section, and the sample was coated with epoxy spray paint. After 24 hours of curing the masking tape was removed, and the gauge section of the sample was gently wiped with an ethanol coated cotton swab to remove any trace residue left by the tape. The sample was suspended in a 110 mL bath of 3.5 wt% NaCl solution mixed with deionized (DI) water and allowed to corrode for 15 days. Every 24 hours, 5 – 15 mL deionized water was added to the uncovered bath to account for water lost due to evaporation. After corrosion, the sample was briefly rinsed in DI water, dried, and transported to the Argonne National Laboratory for *in situ* fatigue testing at the synchrotron facility.

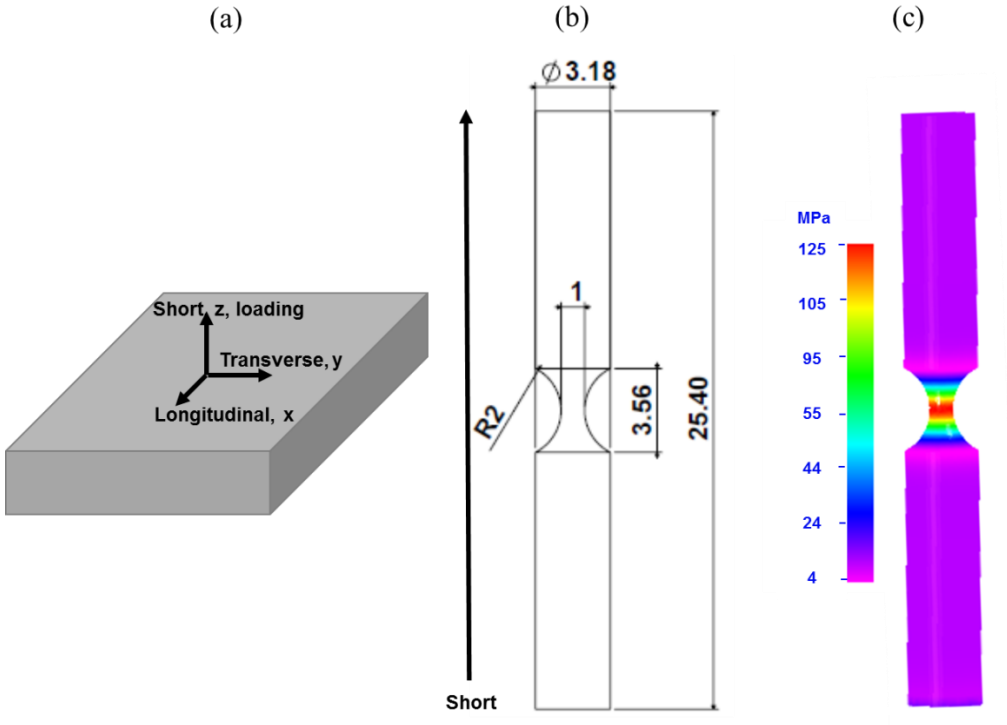

Figure 1: (a) Schematic of 7.6 cm 7075-T6 plate demonstrating short, transverse, and longitudinal directions with respect to the rolling of the plate. (b) schematic of sample indicating machining orientation and dimensions in millimeters. (c) Finite element model displaying the Von Mises Stress contours in the sample, showing uniform stress distribution in the x-ray tomography region of interest.

The *in situ* corrosion-fatigue experiments were performed at the Advanced Photon Source (APS) at Argonne National Laboratory. X-ray synchrotron tomography was performed at the 2-BM beamline of the APS. Details of the APS 2-BM beamline have been described elsewhere [149]. A double-bounced single crystal Si monochromator was used to tune the x-ray energy to 27.4 keV. The 27.4 keV energy was chosen because it provided high contrast between the inclusion particles and the aluminum matrix, based on the

attenuation coefficients of the different phases. The sample was scanned 60 mm away from a 10 μm thick LuAg:Ce scintillator screen at a rotation rate of 0.75°/s across a 180° angle while 1500 projections images were taken, each with a 0.1 millisecond exposure time. A 2560 x 2160 pixel PCO AG (Kelheim, Germany) Edge scientific complementary metal oxide semiconductor (sCMOS) camera recorded the projections with a 0.65 μm pixel size.

A specially designed loading frame, detailed in [132], was used for fatigue testing the samples *in situ* at 2-BM. A specialized bath was mounted to the samples and filled with 3.5 wt% NaCl solution during the experiment. Figure 2 shows a schematic of the sample in the bath. All the samples were fatigue tested under load controlled conditions using a maximum stress (σ_{max}) of 120 MPa and a stress ratio ($\sigma_{min}/\sigma_{max}$) of R=0.1 with the load applied orthogonal to the rolling direction of the sample. The stress was calculated using the minimum cross-sectional area of the sample based on a measurement of virtual tomography slices of the L-T orientation of the sample. The samples were held at $\sigma = 0.5\sigma_{max}$ during the tomography scans to allow sufficient crack opening to view bubbles within the crack while reducing the possibility of sample movement due to stress corrosion cracking during scanning near sample failure. The projections were reconstructed into 3D stacks using Fourier grid reconstruction algorithm in the Tomopy software framework, which is an open-source Python reconstruction program [150]. The data was analyzed using ImageJ [151] and segmentation was performed using the seeded region grow technique in Avizo Fire (Bethesda, MD) [152].

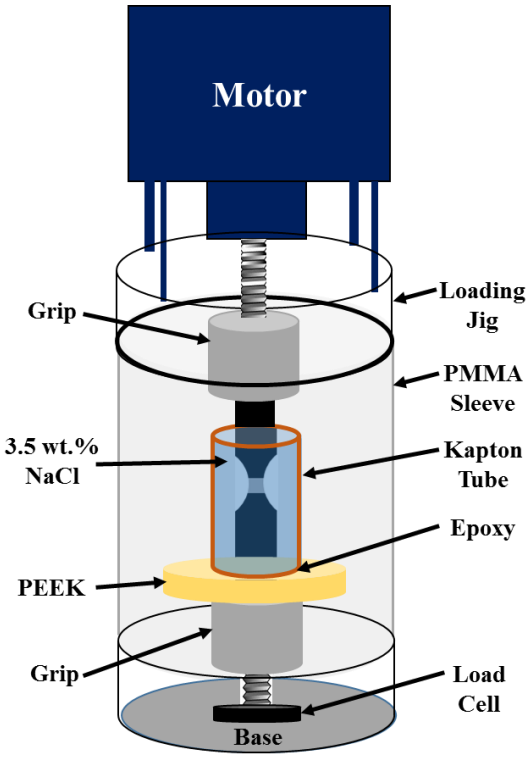

Figure 2: Schematic of the loading jig used for *in situ* fatigue testing of the 7075 samples.

After failure, the fractured pieces were quickly removed, rinsed with deionized water, and dried. The tomography data from time points during and after the test were carefully matched with the SEM images of the fracture surface to select points for FIB-SEM (Auriga, Carl Zeiss Microscopy, Jena, Germany) and EDS (AZtecEnergy, Oxford Instruments, Oxfordshire, United Kingdom) analyses at various points during fatigue crack growth.

3.3 Results

The peak-aged 7075 alloy studied herein is strengthened by semicoherent η' precipitates ($Mg(Cu_{0.15}Zn_{0.85})_2$) [31]. These precipitates are anodic compared to the matrix, which can increase the alloys susceptibility to corrosion and hydrogen embrittlement [31]. This aging condition is known to be susceptible to corrosion pitting in saline solutions due to electrochemical potential differences between the Fe- and Mg-bearing inclusions [54,55,70,153]. The Mg-bearing inclusions are anodic with respect to the matrix while the Mg dissolves, then cathodic after only the corroded Si-O byproduct remains [53,56]. The Fe-bearing inclusions are cathodic with respect to the matrix, leading to preferential dissolution of the matrix surrounding Fe-bearing inclusions [54,55]. The Fe-rich and Mg-rich impurity particles can be seen clearly in the tomography data. The Fe-rich inclusions are brighter than the matrix, and the Mg-rich inclusions are darker than the matrix. The inclusion compositions have been verified via a previous study which compared inclusions viewed using tomography under similar conditions to SEM-EDS spot analysis of the same inclusions in a 7075 alloy [12]. Additionally, since this sample came from a rolled plate, the grains and inclusions were elongated along the rolling direction. The elongated inclusions can be seen in **Figure 3**, which shows an example of corrosion pits found in the specimen via a virtual slice of the material in the L-T orientation.

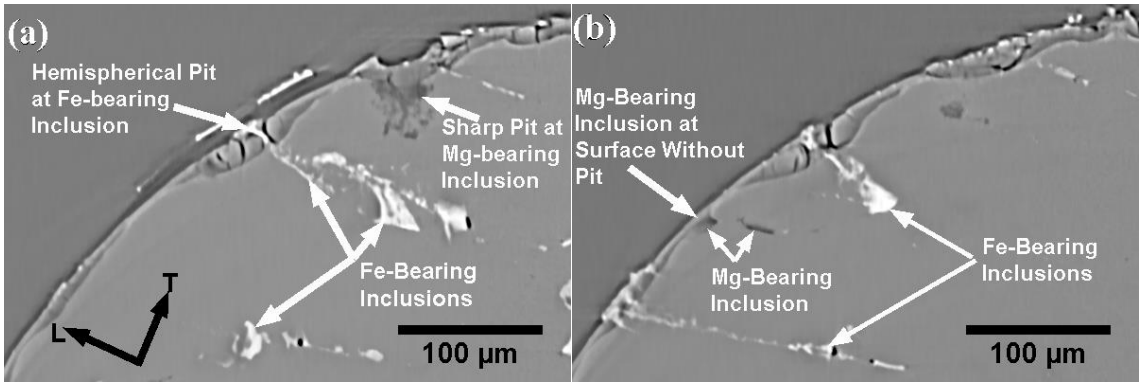

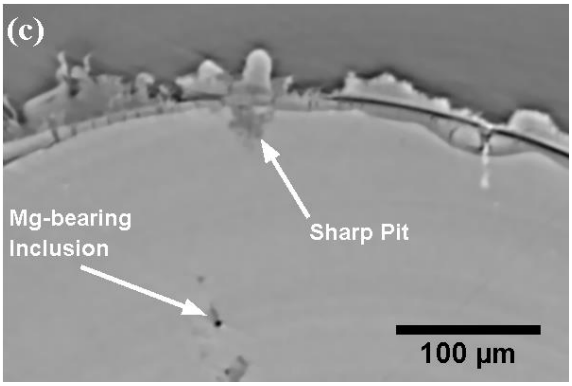

Figure 3: Virtual Slices of corrosion pits in 7075 aluminum alloy. (a) The pit on the left is a typical hemispherical-shaped pit formed by preferential dissolution of the matrix around the noble Fe-rich inclusion, while the pit on the right has a less common morphology with a sharper corrosion feature extending into the matrix past the initial pit. (b) The Mg-rich inclusion on the left side is not corroded, which may have been due to a lack of large oxide-breaking precipitates at the inclusion/matrix/surface interface. (c) Example of a sharp pit feature which may have occurred due to an Mg-bearing inclusion on the sample surface with some critical defects promoting corrosion.

Figure 4 shows a 3D representation of the pits in Figure 3, while **Figure 4** shows a 3D rendering of the pits in **Figure 3** for greater clarity. Note the cracks within the pits. These cracks may have formed along with the corrosion product during corrosion and volume increase during formation of the corrosion product. Besides the pits, the sample exhibited a thin, relatively uniform (0-10 µm) layer of corrosion product covering most of the surface. Cracks in the corrosion product and occasional corrosion pits located stochastically at Mg-rich and Fe-rich inclusion particles were observed on the surface.

Most of the corrosion pits were smooth and hemispherical. The left pit in **Figure 3** represents a typical hemispherical pit geometry which formed due to preferential dissolution of the aluminum matrix surrounding a cathodic Fe-bearing particle. The deeper, sharper pit on the right may have formed due to an Mg-rich particle being present sufficiently near an Fe-rich particle to cause accelerated corrosion *via* galvanic coupling between the two particles of significantly different corrosion potential. Note that not all the inclusions interacting with the surface lead to corrosion, with an example in the far left of Figure 3 showing an Mg-bearing inclusion at the surface but not leading to a pit.

Figure 5 shows a 3D representation of the crevice corrosion pit where a corrosion-fatigue crack initiated. Analysis of the pits in the sample showed that this was the largest pit in the sample with dimensions of 100 µm deep × 305 µm wide × 127 µm high. Using the 3D pit depth and half arc length, we were able to calculate the stress intensity factor for the pit per the Raju-Newman equation [154]. The stress was obtained from the actual area in the plane of the pit. Using these inputs, a K_{max} of about 1.1 MPa·$m^{0.5}$ was obtained in the thinnest section of the sample, while a K_{max} of 1.0 MPa·$m^{0.5}$ was calculated for the deepest pit in the center section.

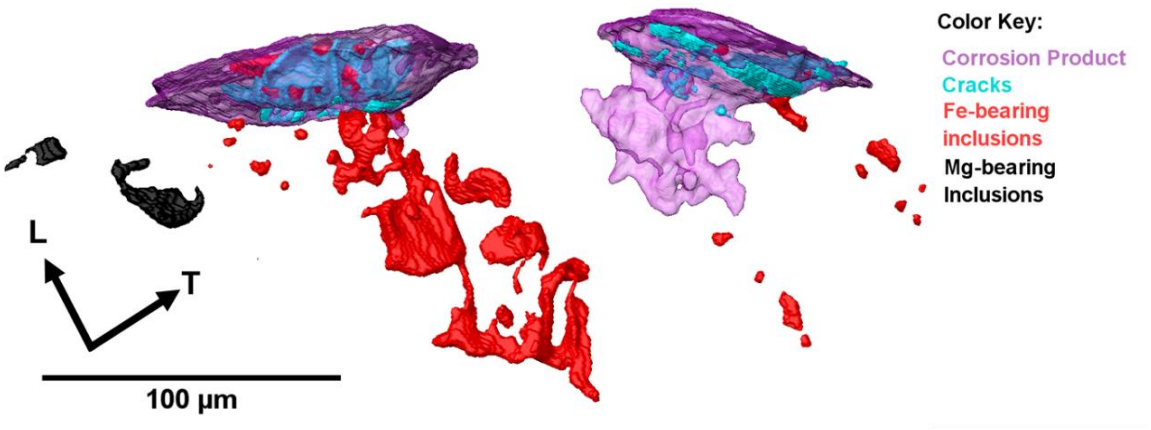

Figure 4: 3D segmented view of corrosion pits in peak-aged 7075 from Figure 3. The pit on the left is a typical pit formed around Fe-rich inclusion. The pit on the right has an exceptionally deep and sharp feature which may have been due to dissolution of an Mg-rich particle very close to an Fe-rich particle on the surface.

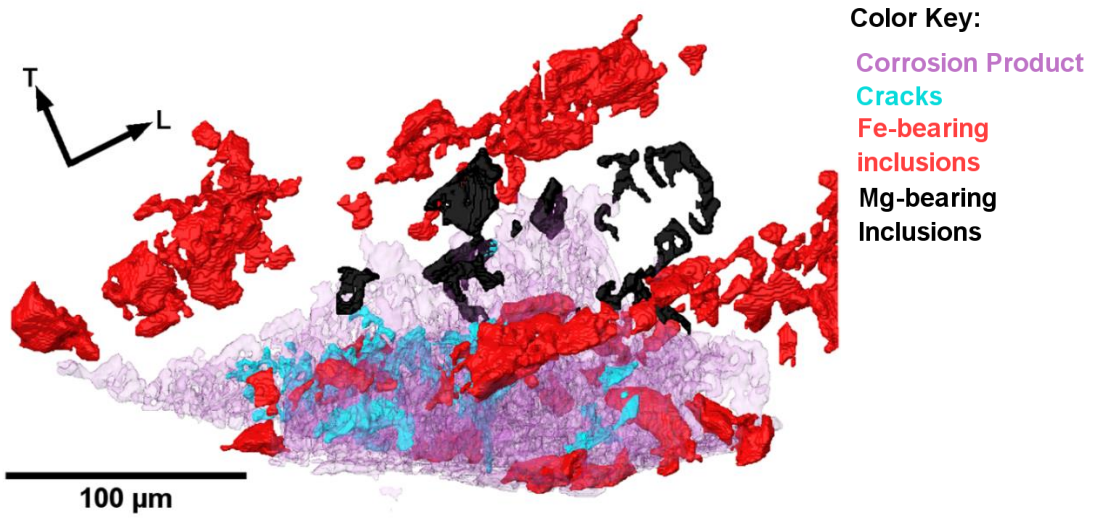

Figure 5: L-T view of the crack-initiating crevice corrosion pit. The pit has a sharp geometry which serves as a stress concentration for fatigue crack initiation and growth.

Crack initiation from the corrosion pit was resolved after 8,500 cycles. The crack was jagged with significant branching and a sharp crack tip, as shown in **Figure 6**. The sharp crack tip serves as evidence of brittle failure [103,114,155]. Peak-aged 7075 alloys are known to be susceptible to hydrogen embrittlement when exposed to aqueous environments, which may be due to corrosion of the anodic precipitates leading to hydrogen evolution, in addition to the AIDE mechanism causing increased dislocation emission at the crack tip during cyclic loading and the HELP mechanism reducing the pileup spacing at the precipitates in the plastic zone, causing shear of the precipitates at lower stress [31,156–158]. Additionally, the crack appeared to interact preferentially with inclusions. This may be due to the brittle inclusions serving as sources of hydrostatic stress, which could promote further embrittlement near the crack tip [24,159]. After 14,300 cycles, the maximum crack opening displacement was 6.6 μm and the minimum resolvable crack tip opening was 1 μm or less, indicating that this crack was very sharp. These bubbles, which are easily observed via in situ synchrotron tomography, are evidence of corrosion during the fatigue process. The bubbles are most likely H_2 gas formed by recombination of evolved H^+ produced by dissolution reactions, described earlier, between the metal surfaces and the solution. Figure 7 shows a highly magnified virtual tomography slice of the crack from the L-T plane of the sample at 14,300 cycles, which clearly depicts bubbles within the crack.

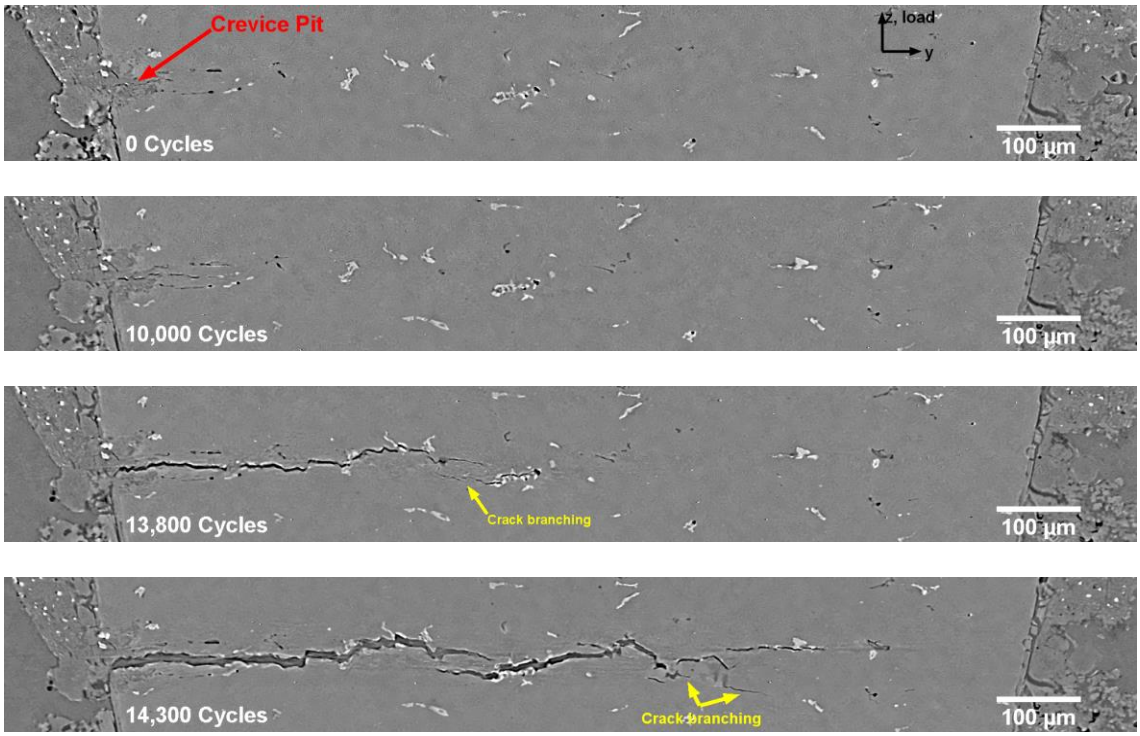

Figure 6: Center YZ plane showing the progression of corrosion-fatigue crack growth from a corrosion pit in peak-aged 7075 tested in 3.5 wt% NaCl solution using σ_{max}=120 MPa, R = 0.1, f = 1 Hz.

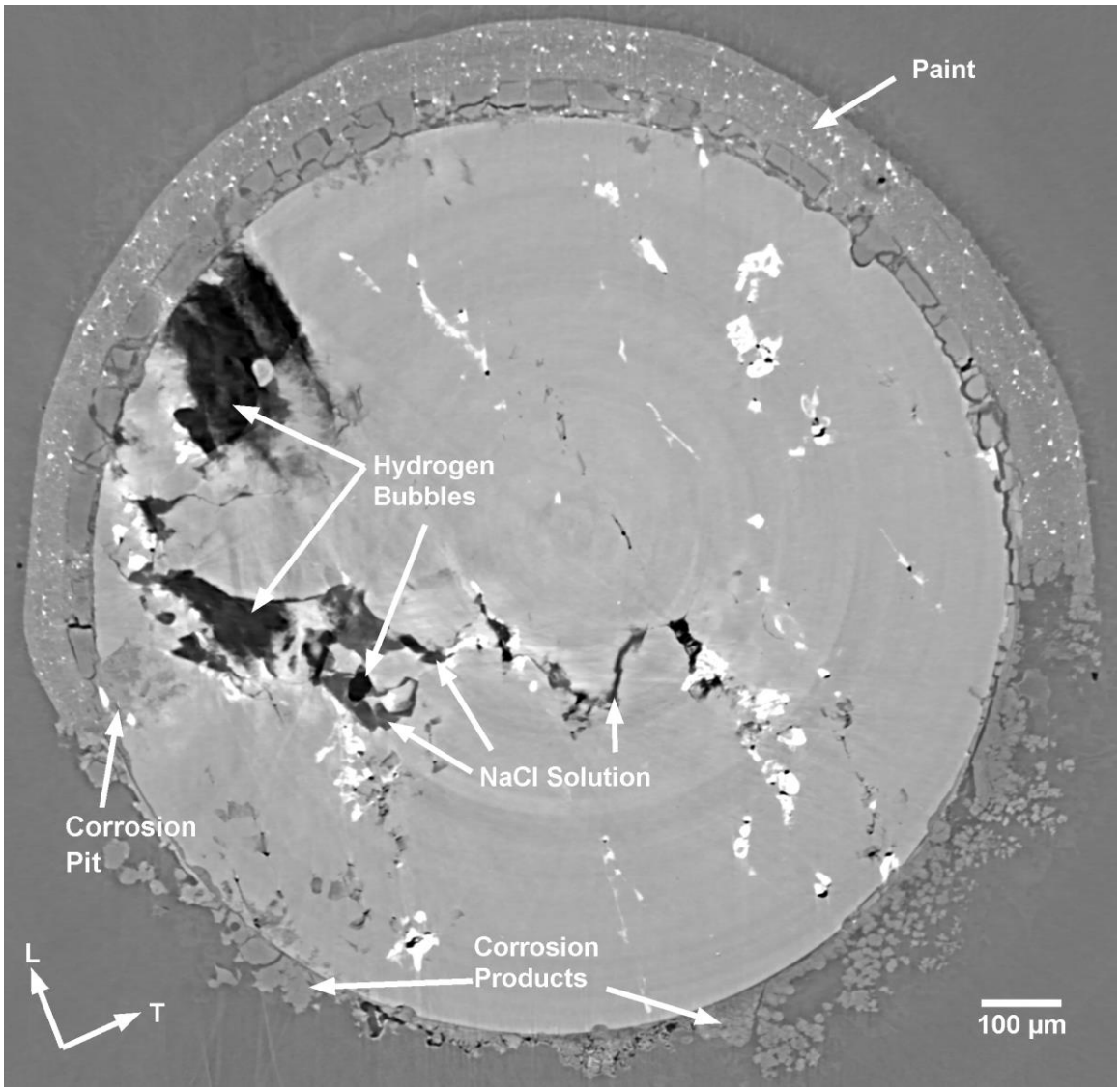

Figure 7: XY Section of the crack at 14,300 cycles depicting a clear instance of bubbles within the 3.5 wt.% NaCl solution-filled crack.

Figure 8 shows a 3D segmented representation of the crack in light blue, the bubbles in dark blue, with inclusion particles touching the crack face before failure overlaid in red and black. Note that the crack is quite tortuous in nature, presumably from the inclusions in the path of the crack. It is interesting to note that the bubbles are always one step behind the crack tip. To examine this effect, the bubble volume and crack surface area were quantified with increasing crack growth. A linear relationship between the exposed crack face surface area and the bubble volume was found, as shown in Figure 9. This relationship is suggestive of the direct link between exposure of the fresh surfaces to NaCl solution and hydrogen evolution observed during crack growth.

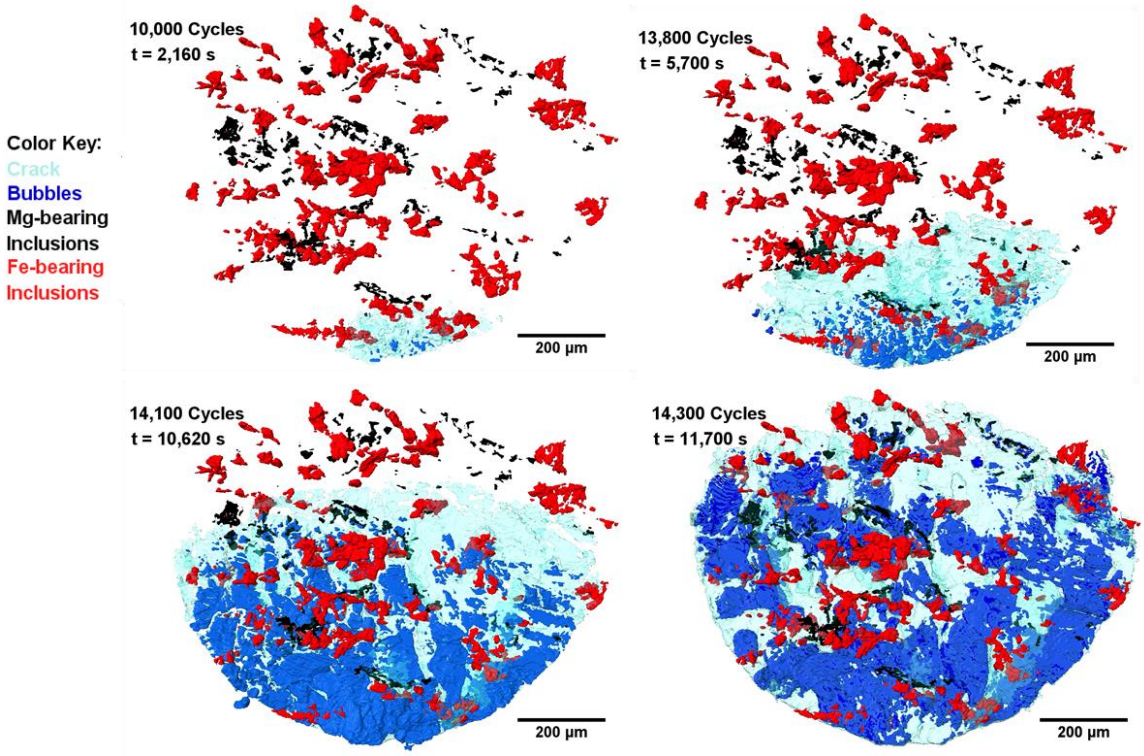

Figure 8: Top-down renderings of the fatigue crack in the peak-aged sample showing the crack progressing approximately along the L-T plane in light blue, gas bubbles in dark blue, Fe-bearing in red, and Mg-bearing inclusions in black. The inclusions which touched the crack before failure were traced back to the corroded sample and overlaid on the crack in the rendering to visualize their interaction with the crack and bubbles.

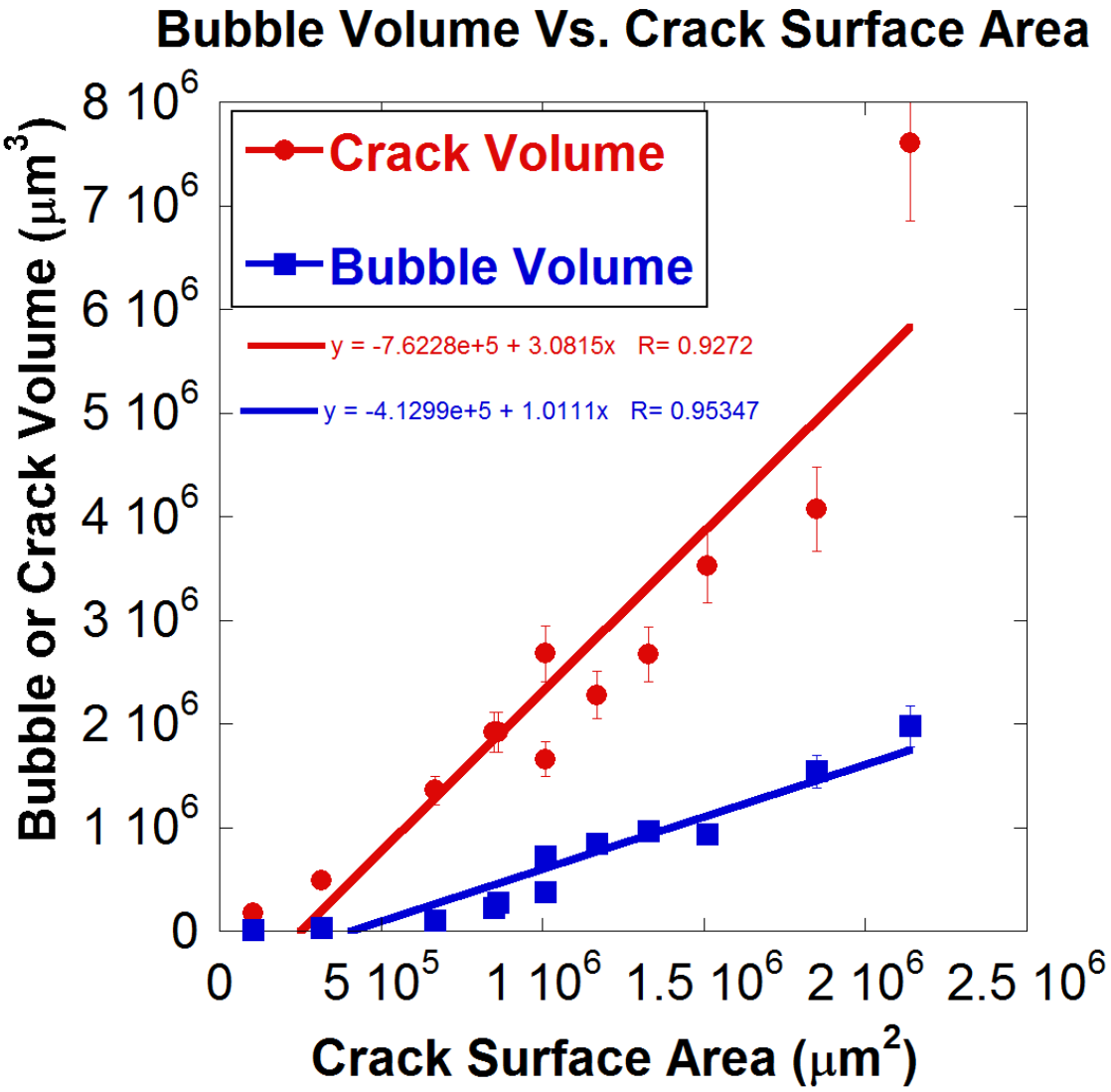

Figure 9: Crack volume and bubble volume as a function of crack surface area for the peak-aged sample. 10% error bars are included to account for errors in measurement incurred during the segmentation process.

To pinpoint the origin of the reactions causing hydrogen evolution, a closer study of the time-dependent evolution of individual phases during crack growth was conducted.

Figure 10 shows a selected region of the sample near the pit at high magnification, where H_2 bubbles appear within the crack touching Mg-bearing inclusions. Figure 11 shows a magnified 3D rendering of the same region more clearly showing the corrosion reactions. Here one can observe that, during crack growth, the crack goes around the Fe-rich inclusions, but that the Mg-rich inclusions appear to dissolve during the corrosion-fatigue process. Since Mg is more anodic than the aluminum matrix, Mg-bearing inclusions corrode before the matrix by dissolution of the Mg from the Mg_2Si inclusion [53–55]. However, the resolution of the x-ray microtomography was not high enough to determine whether there was complete dissolution or partial dissolution of the Mg_2Si inclusions.

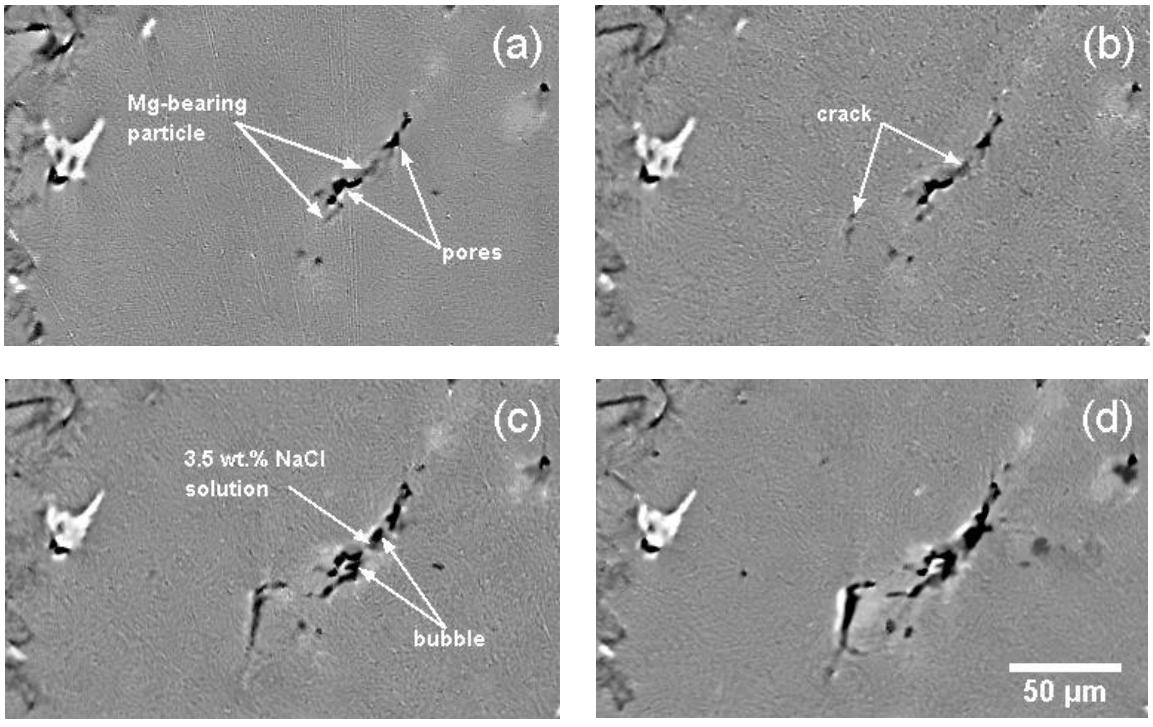

Figure 10: Highly magnified tomography slices of a section of the peak-aged 7075 sample near the corrosion pit (left side of images) showing the crack growing through an Mg-bearing inclusion and pores. After continued growth, the crack becomes darker in

some regions due to H_2 bubble evolution near the Mg_2Si, suggesting that a primary cause of the bubble formation is the dissolution of Mg from the Mg-bearing inclusion particles. (a) 10,000 cycles (2,160 s exposure time) (b) 12,000 cycles (~4,320 s exposure time), (c) 13,000 cycles (~5,700 s exposure time), (d) 13,100 cycles (~6,420 s exposure time).

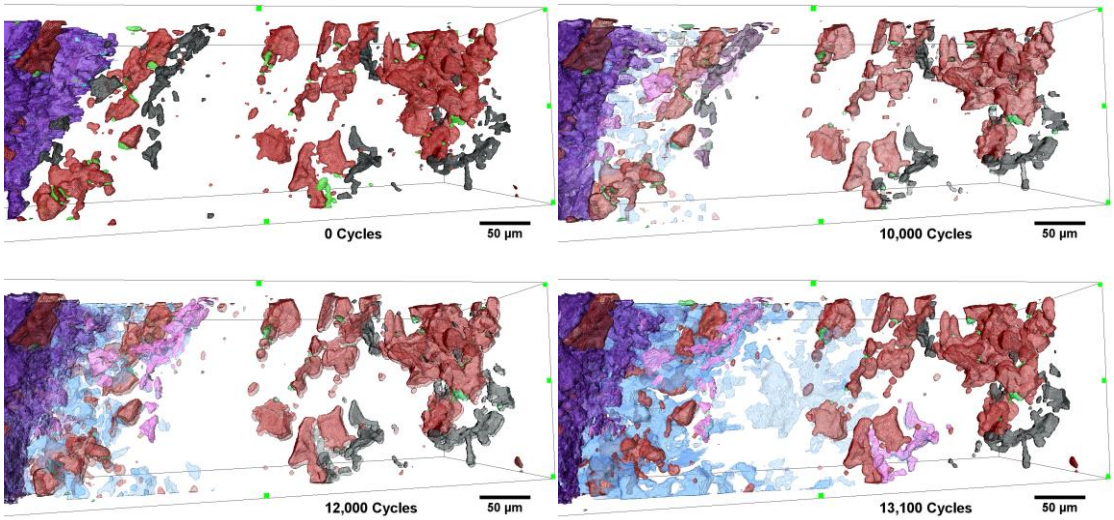

Figure 11: 3D rendering of a section of the peak-aged 7075 sample near the corrosion pit showing the hydrogen bubble formation at the Mg-bearing inclusions exposed during cracking, suggesting that a primary cause of the bubble formation is the dissolution of Mg from the Mg-bearing inclusion particles. Pit: purple, voids: green, Fe-bearing inclusions: maroon, Mg-bearing inclusions: black, Exposed/corroding Mg-bearing inclusions: pink, Hydrogen bubbles: blue.

To determine the extent of dissolution of the Mg_2Si inclusions, two Mg_2Si inclusions on the crack face were selected for FIB-SEM cross-sectioning and EDS analysis by careful comparison of the SEM fracture surface images with the *in situ* tomography data before, during, and after fatigue testing. The selected FIB trench regions are outlined in red in

Figure 12. An inclusion exposed after approximately 10,000 cycles, and another inclusion exposed after approximately 14,100 cycles was selected. EDS spot analysis was performed at the center of the inclusion and Table 1 shows that the inclusion was predominately SiO_2, and was mostly corroded by preferential dissolution of Mg and then passivation of the remaining Si. This indicates that there is preferential dissolution of the Mg_2Si inclusion itself, with the Mg leaching out preferentially and leaving behind Si. The FIB cross-section analysis also showed, in

Figure 13, a subsurface portion of the inclusion intersecting a secondary crack which was exposed by FIB milling. This secondary crack was likely a consequence of hydrogen evolution from dissolution of the Mg_2Si inclusion during the initial crack growth.

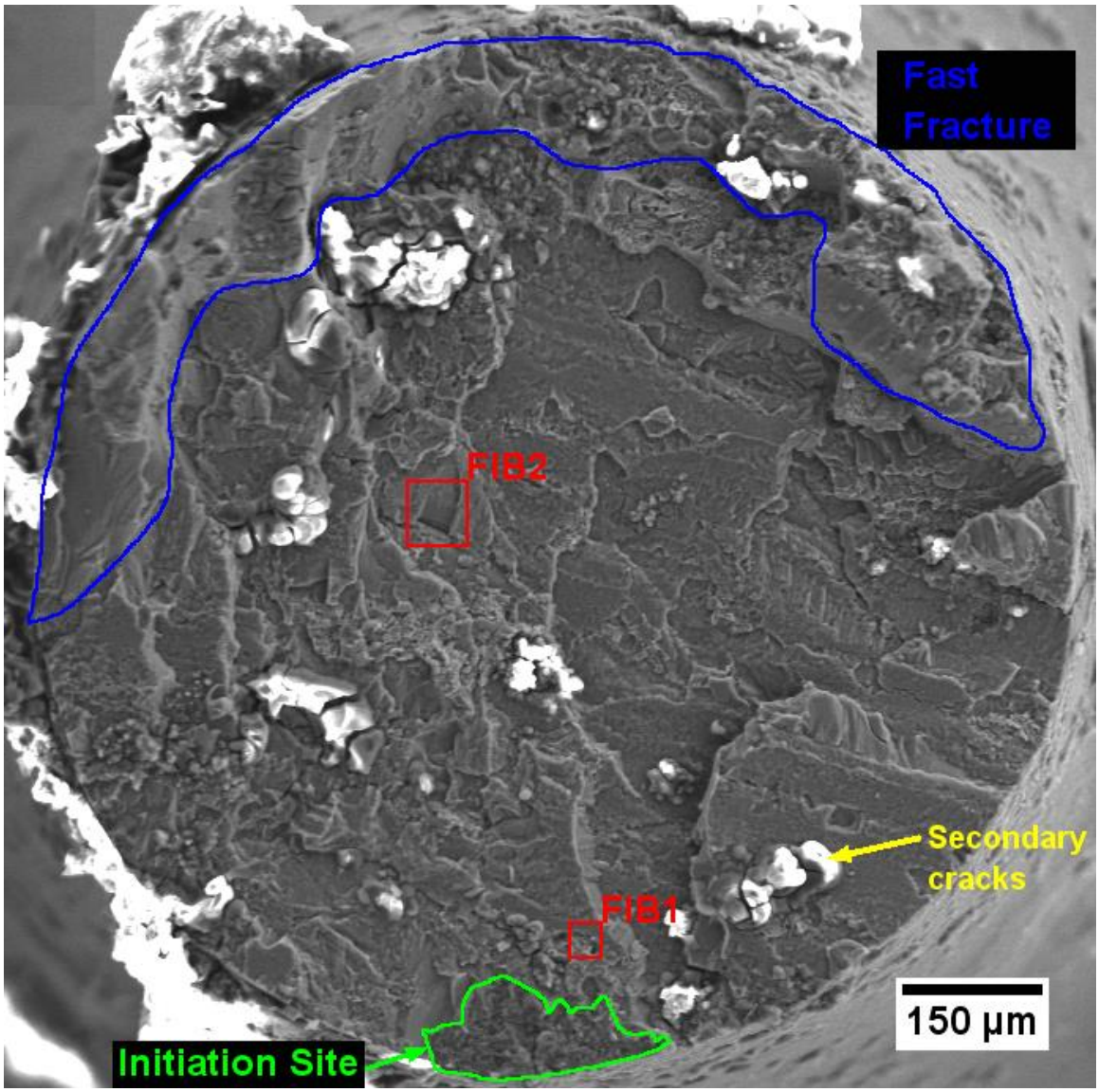

Figure 12: SEM secondary electron image of the top fracture surface of the peak-aged 7075 alloy with notable regions annotated. FIB1 represents the first FIB sectioning of an Mg_2Si inclusion exposed after 10,000 cycles. FIB2 represents the second FIB sectioning of an Mg_2Si inclusion exposed after 14,100 cycles.

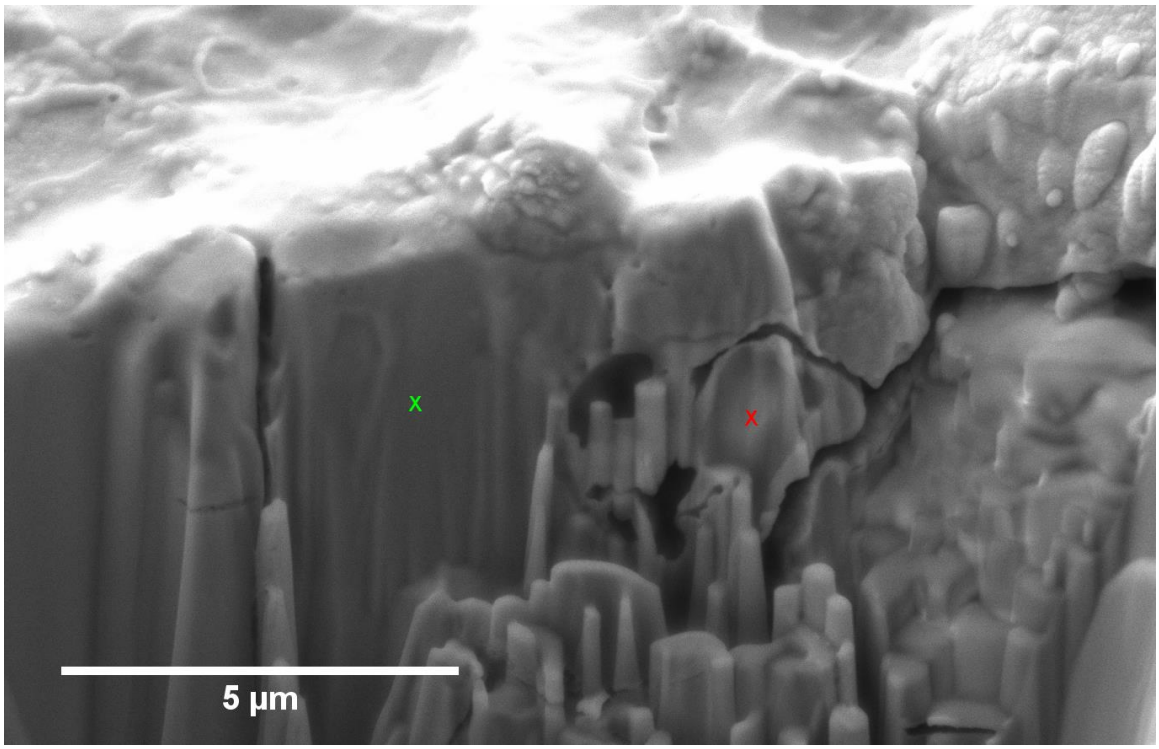

Figure 13: Cross-section view of a portion of the FIB1 Mg_2Si inclusion shown in Figure 12 with EDS spot analyses on the matrix (green "x") and the inclusion (red "x"). Also note the secondary crack touching the side of the inclusion.

Table 1: EDS spot analysis of the matrix and inclusion from Figure 13 showing the inclusion is completely depleted of Mg even within the depth of the matrix.

Element	**O**	**Si**	**Mg**	**Al**	**Zn**
Green	1	-	2.1	92.3	4.6
Std. Dev. (wt%)	0.3	-	0.4	0.9	0.8
Red	49.5	48.1	-	2.4	-
Std. Dev. (wt%)	0.8	0.8	-	0.5	-

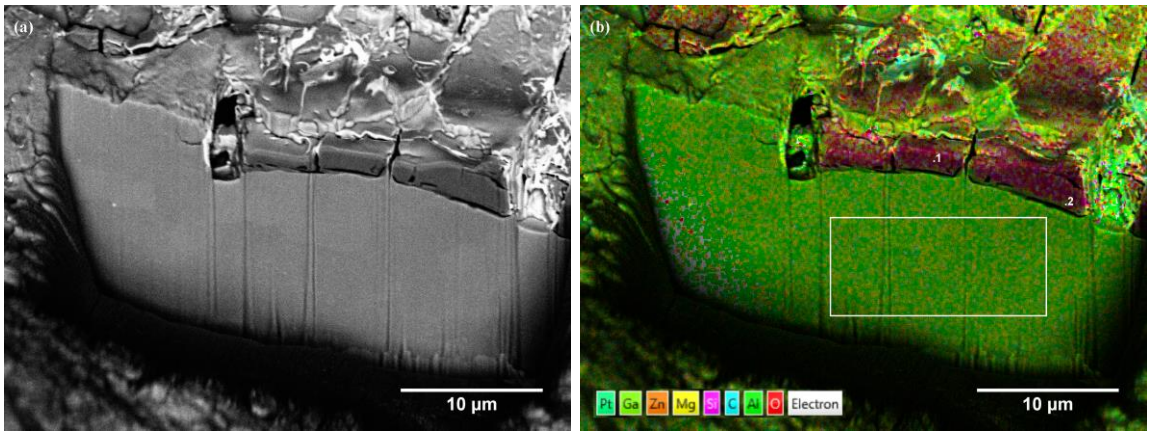

Figure 14: (a) Cross-section secondary electron SEM image of an Mg_2Si exposed after 14,100 cycles of corrosion-fatigue. (b) EDS dot map of the cross-section showing the inclusion was also depleted of Mg during the corrosion-fatigue.

Table 2: EDS composition table of selected regions from the EDS dot map in **Figure 14**.

Element	**O**	**Si**	**Al**	**Mg**	**Zn**	**Cl**	**Ga**
Point 1 (wt.%)	56	39	4.4	-	-	-	-
Std. Dev. (wt.%)	0.3	0.3	0.2	-	-	-	-
Point 2 (wt.%)	34	28	35	-	-	1.6	1.3
Std. Dev. (wt.%)	0.4	0.4	0.4	-	-	0.4	0.3
Boxed Region (wt.%)	1	-	91	2.2	5.4	-	-
Std. Dev. (wt.%)	0.2	-	0.7	0.3	0.6	-	-

To estimate the corrosion rate of the Mg_2Si within the crack, an inclusion which was not exposed until after approximately 14,100 fatigue cycles was also analyzed using FIB-SEM and EDS. Pt was deposited before the milling to ensure a smoother FIB section. **Figure 14** (a) and (b) show the secondary electron image of the FIB trench and an EDS dot map of the inclusion. Selected portions of the inclusions and the aluminum matrix were chosen for compositional analysis and the results were displayed in Table 2. From

these results it is quite clear that the corrosion of the Mg_2Si happens rapidly within the crack in 7075 as this inclusion was exposed to saline solution for less than 35 minutes.

3.4 Discussion

The 4D study of both pitting and subsequent corrosion-fatigue provided a rich amount of microstructural mechanistic information. For example, the pit shapes suggested that in peak-aged 7075 alloys, Fe-bearing inclusions lead to hemispherically-shaped pits while Mg-bearing inclusions can lead to sharp pits. It is well-known that pits form by trenching surrounding Fe-bearing inclusions since the inclusions are noble and cathodic with respect to the matrix [43,160–164]. The Mg-bearing inclusions form pits by initial rapid dissolution of the Mg from the Mg_2Si, followed by subsequent corrosion of both the cathodic Si-rich skeleton which is left behind, and the Al matrix surrounding it [53]. Thus, the Mg-pits were observed to have much sharper morphology than the Fe-rich pits. Some surface inclusions may cause pits while others do not. One possible explanation for this is that inclusions interacting with grain boundaries or triple points would be located at higher energy sites which could also lead to nucleation of larger precipitates with a higher copper concentration, leading to greater electrochemical potential differences at the inclusion/matrix interface and faster corrosion progression [165]. Recent work using focused ion beam tomography, in fact, has shown that the precipitate density at the inclusion/matrix interface and subgrain boundaries are larger than precipitates within the bulk grain due to heterogeneous nucleation at inclusion surfaces [61]. If an inclusion, and thus a subsequent pit resides at a grain boundary, it

may be more prone to grow a crack as it is a likely location for a crack initiation site for stress corrosion cracking and stage I fatigue crack growth in aluminum alloys. An examination of the pit's sharpness in **Figure 5** further suggest that the sharpness of the pit and chemical damage near the pit tip are playing significant roles in increasing effective stress concentration and reducing the resistance of the material to crack initiation. The microcracks from volume change may also be contributing to the incubation of a fatigue crack during subsequent corrosion-fatigue.

Bubble evolution during cracking was observed, and expected because of exposure of bare, unpassivated aluminum and inclusion surfaces during corrosion cracking to NaCl solution, which is known to lead to hydrolysis reactions with the solution and subsequent hydrogen bubble evolution [37,59]. The linear relationship observed in **Figure 9** provides significant evidence that these bubbles are a consequence of the exposure of the bare metal and inclusion surfaces to the solution. Consequently, the pH at the crack tip has been shown to become more acidic during the corrosion cracking process [84]. A proportion of the evolved H^+ may enter the matrix *via* adsorption and subsequent diffusion at the crack tip to embrittle the material, while the rest can dissolve into the solution to raise its acidity, or recombine to form H_2 bubbles [82,84,95]. The exact proportions of hydrogen which diffuse into the sample, solution, or bubbles are difficult to measure because of the high mobility and small atomic number of hydrogen [95,166]. Therefore, the evolved bubbles can provide some quantitative understanding of the embrittling environment at the crack tip, especially as understanding of local corrosion cracking phenomena improves. With high resolution *in situ* synchrotron tomography, the

bubbles within the crack were clearly observed both here and elsewhere [15]. These bubbles serve as evidence of accelerated corrosion and enhanced localized embrittlement. In this work, we have shown hydrogen bubble evolution within a small corrosion-fatigue crack for the first time. Quantification of these bubbles as they initiate and grow within the crack can provide improved understanding of exactly how much hydrogen goes into the matrix for embrittlement, into solution for increased acidity, or recombines to form gas bubbles. Additionally, using the *in situ* nondestructive technique we can pinpoint the locations of each respective bubble to understand how each microstructural feature contributes to the hydrogen evolution, which may potentially lead to improved alloy design.

To pinpoint the exact sources of corrosion bubble evolution, the tomography data was carefully observed as in **Figure 10**. Many of the bubbles were near Mg-bearing inclusions. In acidic to nearly neutral conditions as in this case, the Mg in the Mg_2Si inclusion particles is anodic with respect to the matrix and the iron-bearing inclusions and dissolves preferentially from the Mg_2Si to leave passivated Si [15,49,53,56,84,167]. Based on the FIB-SEM-EDS analysis results, all the Mg-rich inclusions touching the crack had reduced concentrations of magnesium. Figure 11 shows a high magnification 3D rendering of the sample near the pit during the fatigue cracking process. As the crack proceeded through the inclusions, their corrosion began and bubbles formed within the crack touching the Mg_2Si inclusions due to the dissolution of Mg from Mg_2Si.

This suggests that Mg dissolution contributed a significant proportion of the H_2 bubble formation in this sample. Additionally, the bubbles are also at a much higher

pressure than the ambient atmosphere due to their small size and higher surface tension leading to increased internal pressure, in addition to the tortuous nature of the crack preventing the bubbles' escape. For instance, basic physical laws of surface tension show that the pressure difference between a bubble and ambient atmosphere is inversely proportional to the bubble radius. Based on this, the maximum pressure at the resolvable crack tip of 1 μm could be approximately 75% higher than atmospheric pressure, and if the true crack tip is below the resolution limit on the order of 1 nm, then the pressure could be ~10x higher than atmospheric pressure. There is a possibility that some of the bubbles escaped during fatigue cycling between scans. Hence, future work should use *in situ* synchrotron tomography to investigate corrosion-fatigue in real time during cycling such that every bubble which emanates from the crack is captured with perfect certainty and corrosion within the crack is accurately related to the expected corrosion rates for a free surface. With increases in throughput due to advances in synchrotron tomography and computational systems, real time capture and quantitative analysis of corrosion-fatigue may soon be a possibility.

3.5 Summary

A peak-aged 7075 aluminum alloy sample was prepared by corrosion in 3.5 wt% NaCl solution for 15 days, then fatigue tested in solution *in situ* using synchrotron X-ray tomography. The pit geometry and fatigue crack growth progress were examined in 3D. This study yielded valuable insights regarding the depth and nature of corrosion pits within the Al7075 matrix. Using *in situ* testing, the effect of corrosion pits on the

corrosion-fatigue crack initiation process was investigated. Furthermore, the corrosion within the crack face during fatigue was investigated *via* interrupted tracking of the bubble evolution and FIB-SEM-EDS analysis of the corrosion on selected areas of the crack faces. *In situ* synchrotron tomography showed directly that pre-existing cracks within the corrosion product serve as preferential fatigue crack initiation sites due to their high stress concentration and attachment to the underlying aluminum metal matrix. These cracks may be due to preferential intergranular corrosion attack, but further work is required to determine the exact cause. Comparison between time-resolved 3D data and *post mortem* FIB-SEM-EDS fractography suggested that a significant portion of the evolved bubbles may come from preferential dissolution of Mg from the Mg_2Si particles.

4 3D TIME-RESOLVED OBSERVATIONS OF FATIGUE CRACK INITIATION AND GROWTH FROM CORROSION PITS IN AL7XXX ALLOYS USING SYNCHROTRON X-RAY TOMOGRAPHY

4.1 Introduction

The corrosion and cracking mechanisms have been proven interrelated and dependent on precipitate structure, yet the effect of precipitate structure on pit morphology and subsequent fatigue crack initiation is not well known. Therefore, X-ray tomography was used to view the 3D shape of the corrosion pits in the 7075 and 7475 alloys of peak-aged, overaged, and highly overaged conditions after 15 days' immersion in 3.5 wt.% NaCl solution. *In situ* corrosion fatigue testing was performed on the corroded samples in 3.5 wt.% NaCl solution to observe the corrosion fatigue crack initiation properties as a function of aging condition and impurity concentration. By using the 3D *in situ* tomography, the mesoscale processes of the fatigue crack initiation and growth from corrosion pits can be demonstrated.

4.2 Materials and Methods

Pieces were cut from a 3" Al7075-T651 block and a 2" 7475-W51 block, then heat treated at 510 ^{o}C for 2 hours. The pieces were water quenched, then rapidly placed into a lower temperature furnace for heat treatment to peak-aged, over-aged, and highly overaged conditions. **Table 3** shows the heat treatment procedures used for each aging condition. The peak-aged pieces were placed in a 120 ^{o}C furnace for 24 hours. The over-aged pieces were placed in a 107 ^{o}C furnace for 6.25 hours, then moved to a 163 ^{o}C

furnace for 50 hours. The highly overaged samples were subject to the same heat treatment as the overaged pieces, followed by 200 ºC precipitation aging for 50 hours.

Table 3: Heat treatments applied to the as-received materials for each aging condition tested.

Heat Treatment					
Peak-Aged		**Over-aged**		**Highly Over-aged**	
Time (h)	**Temperature (ºC)**	**Time (h)**	**Temperature (ºC)**	**Time (h)**	**Temperature (ºC)**
2	510	2	510	2	510
24	120	6.25	107	6.25	107
		50	163	50	163
				50	200

The sample geometry and sample preparation technique are described in [168]. The samples were separated by aging condition and alloy type, then suspended in 110 mL baths of 3.5 wt% NaCl solution mixed with deionized water and allowed to corrode for 15 days. Every 24 hours, deionized water was added to the uncovered baths to account for water lost due to evaporation. After corrosion, the samples were briefly rinsed in DI water, dried, and transported to the Argonne National Laboratory for *in situ* testing.

The fatigue experiments were performed at the Advanced Photon Source (APS) at Argonne National Laboratory. X-ray synchrotron tomography was performed at the 2-BM beamline of the APS. Details of the APS 2-BM beamline have been described elsewhere [149]. A double-bounced single crystal Si monochromator was used to tune the X-ray energy to 27.4 keV. The samples were scanned 60 mm away from a 10 μm thick LuAg:Ce scintillator screen at 0.75 º/s rotation rate across a 180º angle while 1500 projections images were taken, each with a 0.1 millisecond exposure time. A 2560 x 2160

pixel PCO edge sCMOS camera recorded the projections with a 0.65 μm pixel edge length.

A specially designed loading frame was used for fatigue testing the samples *in situ* at 2-BM. The details of the loading frame are described elsewhere [132]. A custom bath, described in [168], was used to submerge the sample gauge sections in 3.5 wt.% NaCl solution during testing. All the samples were fatigue tested under load controlled conditions using a max stress of σ_{max}=120 MPa and stress ratio R = 0.1, with the stress calculated using the minimum cross-sectional area of each sample based on measurements from X-ray tomography. The samples were held at $\sigma = 0.5\sigma_{max}$ during the tomography scans to reduce the likelihood of stress corrosion cracking during scanning when the crack was large and the maximum stress intensity was sufficiently high. The projections were reconstructed into 3D stacks using the Tomopy open-source Python reconstruction software framework [150]. The data was analyzed using ImageJ [151] and segmentation was performed using Avizo Fire (Bethesda, MD).

4.3 Results

4.3.1 Effect of Aging on Corrosion Pit Depth

An increase in maximum pit depth was found with increased aging for both the 7075 and 7475 alloys. Figure 15 shows minimum Z projections of selected samples in the 7075 alloy for the peak-aged, over-aged, and highly overaged samples. The maximum pit depth observed in the 7075 peak-aged samples was 50 μm. The 7075 overaged samples had a maximum pit depth of 192 μm. The 7075 highly over-aged sample showed a maximum pit depth of over 500 μm, with the sample gauge section corroding completely

through in one case. Figure 16 shows the minimum Z projections of the corrosion pits in the 7475 alloys of different aging conditions. In the 7475 alloy, the maximum pit depth in the peak-aged samples was 25 µm, 160 µm in the over-aged condition, and 342 µm in the highly over-aged condition.

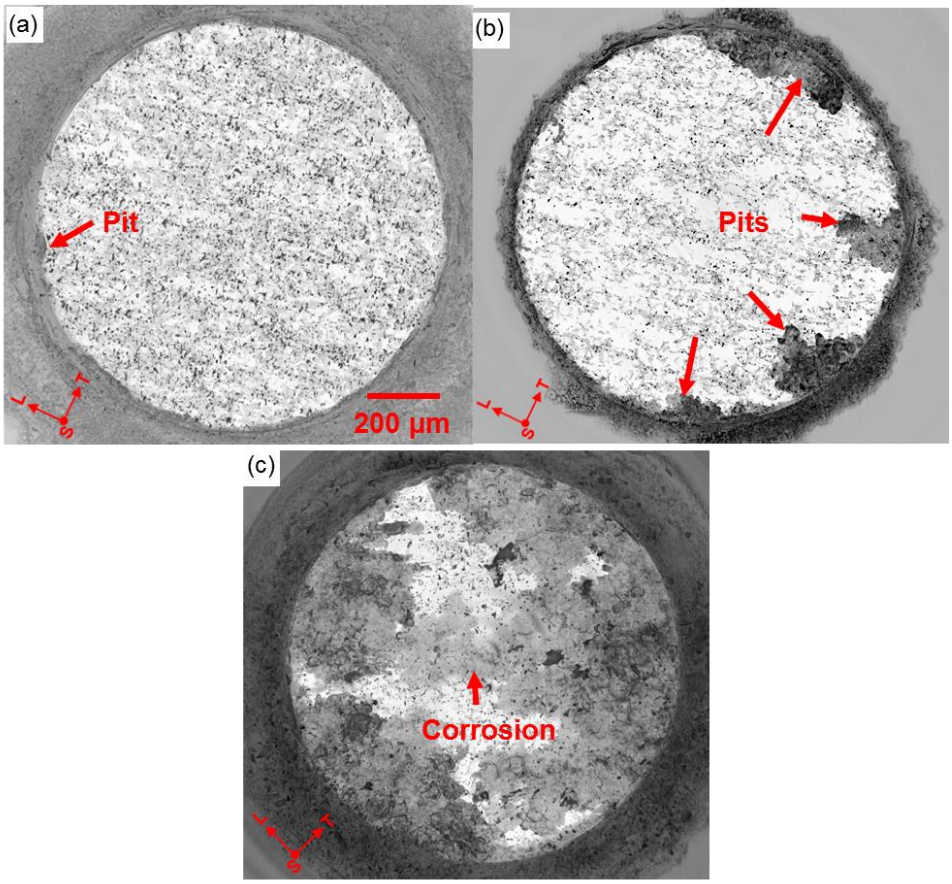

Figure 15: Minimum Z projections of the 7075 (a) peak-aged, (b) over-aged, and (c) highly over-aged samples scanned at 2-BM suggest that there is a relationship between pit depth and precipitate size. The peak-aged samples have very small pits compared to the highly overaged samples.

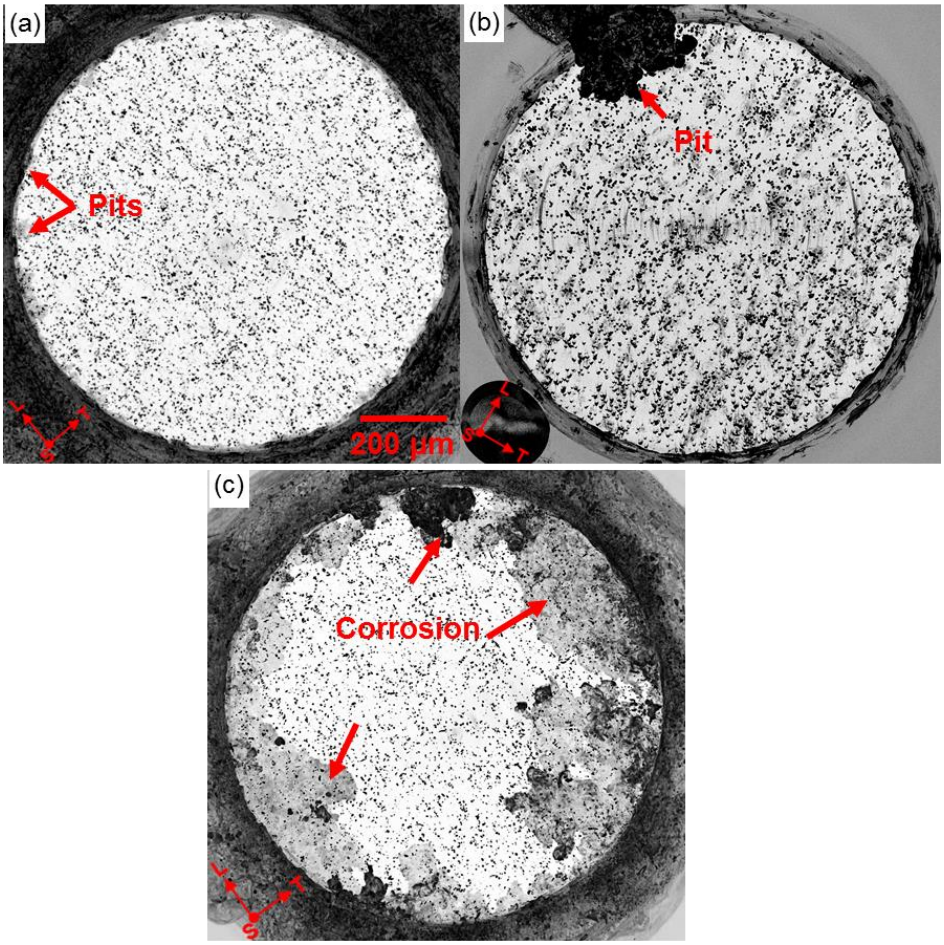

Figure 16: Minimum Z projections of the 7475 (a) peak-aged, (b) over-aged, and (c) highly over-aged samples scanned at 2-BM samples scanned at 2-BM show a similar trend between pit depth and aging duration. The peak-aged samples have smaller pits than the overaged samples.

4.3.2 Effect of Aging on Corrosion Fatigue Crack Growth

Since the cracks and bubbles are much darker than the matrix, the crack growth was measured by taking the minimum of the 3D datasets along the height of the sample to obtain minimum projections along the sample height, which gave a clear representation of the crack's reduction of cross-sectional area in the sample. Hence, crack depth and crack surface half-arc length were measured by tracing over the minimum Z projections in ImageJ as a simple method to quantify the damage. **Figure 17** shows an example of the pit and crack geometry measurement method. Note the extra traces inside to show what is being considered a crack or a pit. When the crack is initiating, the opening displacement is low since it is closer to the resolution limit of the tomography which causes it to appear less dark than subsequent time points. While this method gives useful information about the reductions in cross-sectional area of the sample, certain features such as the flatness of the pit, or if one pit is above another, may also affect the stress intensity factor. Therefore, 3D modelling of the corrosion pits in the overaged sample shown in **Figure 17**(a-d) was also performed and is describe later.

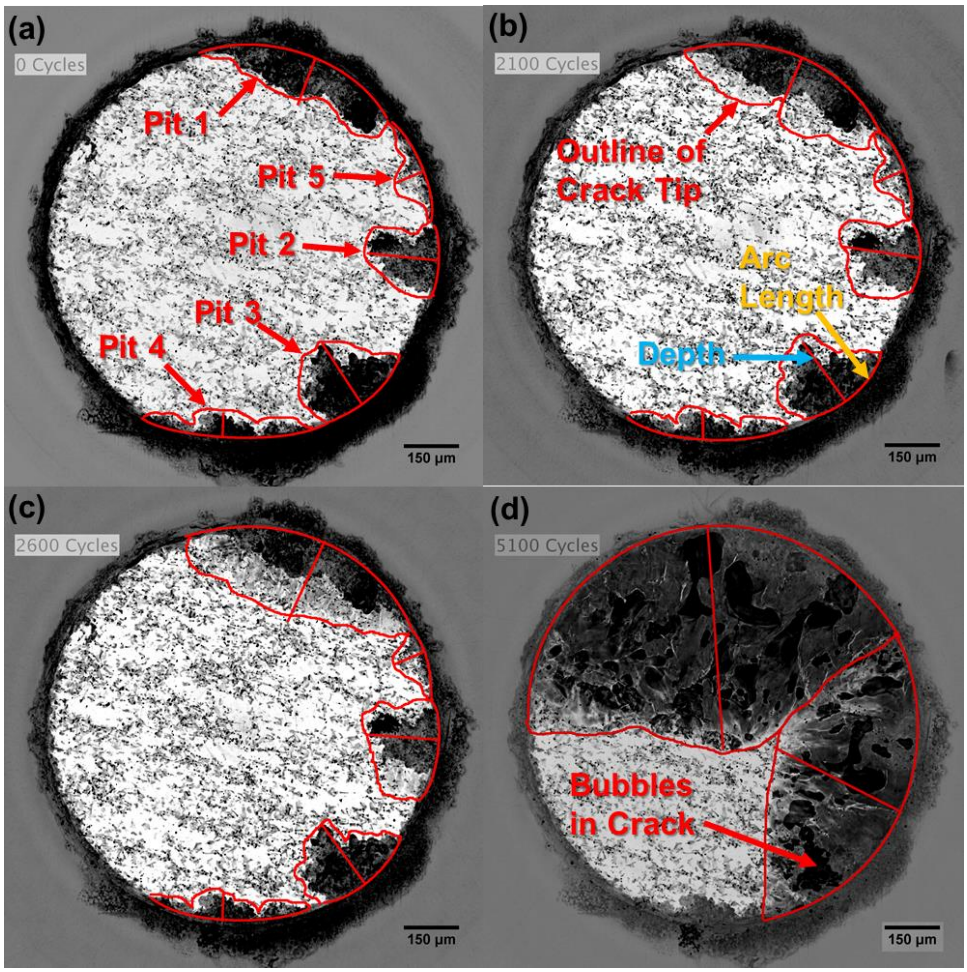

Figure 17: Virtual minimum Z projection of the overaged 7075 showing the pit structure before, and crack growth during fatigue. The overaged sample cracked at the largest pit first, then the deepest pit.

The measurements of the crack depth and arc length taken from the minimum Z projections of the 3D *in situ* fatigue data were also used along with the Raju-Newman relationship to compute the stress intensity factors during crack growth and measure the crack growth rates of the samples [154]. The results were compared to literature data [76,169] on crack growth rates of long fatigue cracks tested under similar conditions. **Figure 18Error! Reference source not found.** shows the fatigue crack growth rates for

each peak-aged sample. **Figure 19** shows the fatigue crack growth rates for the over-aged samples. Note that crack initiation and growth was observed from multiple pits within some of the over-aged samples. **Figure 20** shows the crack growth rate plots for the highly over-aged samples. All the highly over-aged samples showed crack initiation and growth from multiple pits. Additionally, a greater scatter was observed in the highly over-aged data compared to the peak-aged and over-aged samples. This scatter may be due to increased competition between the multiple large pits and cracks contained within each sample. Figure 21 depicts a side view tomography slice near the center of 7075 samples of each aging condition in the last image taken before fatigue failure. From this figure, crack branching and a sharp crack tip can be seen in the peak-aged sample, with the crack growing through many of the inclusions. The over-aged crack had a slightly less sharp crack tip than the peak-aged sample and still cracked through inclusions. The highly over-aged sample showed further ductility, with void formation surrounding the inclusions before failure.

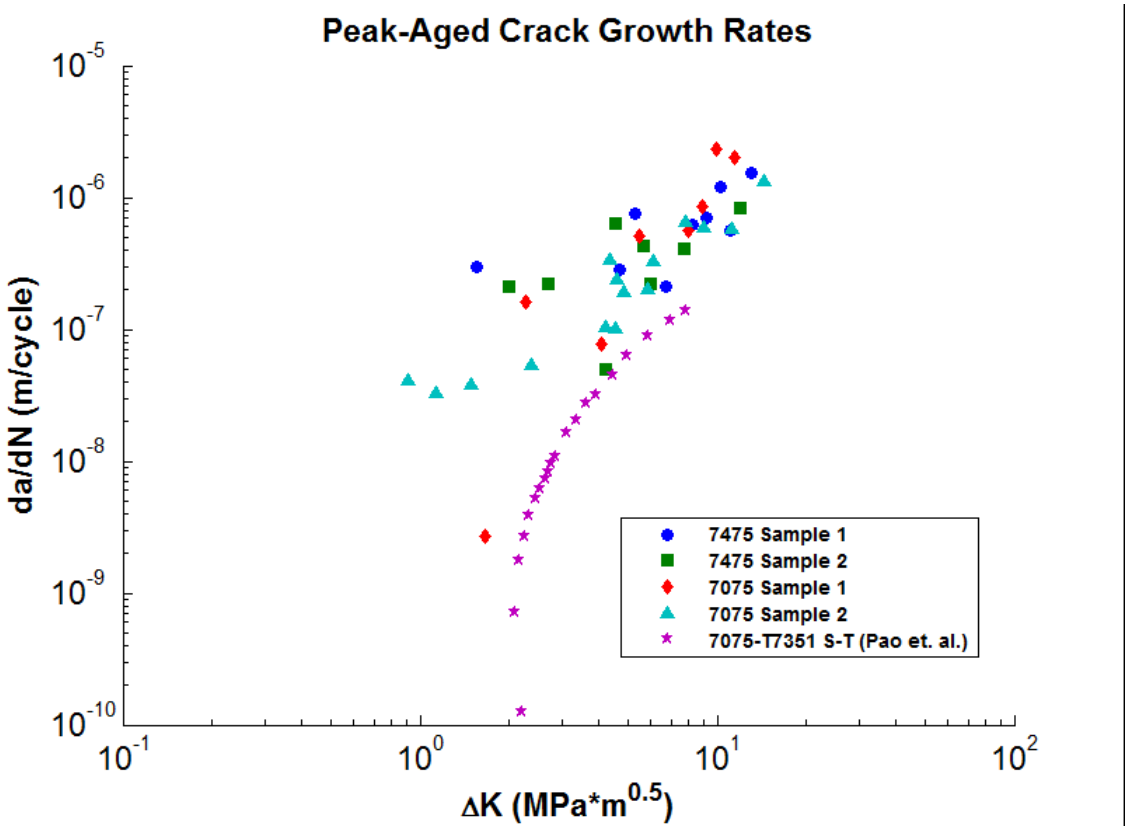

Figure 18*:* Crack growth rate plots of *in situ* tested samples of the peak-aged condition. Crack initiation was observed from a single pit in the peak-aged samples. The reference data was found in [76].

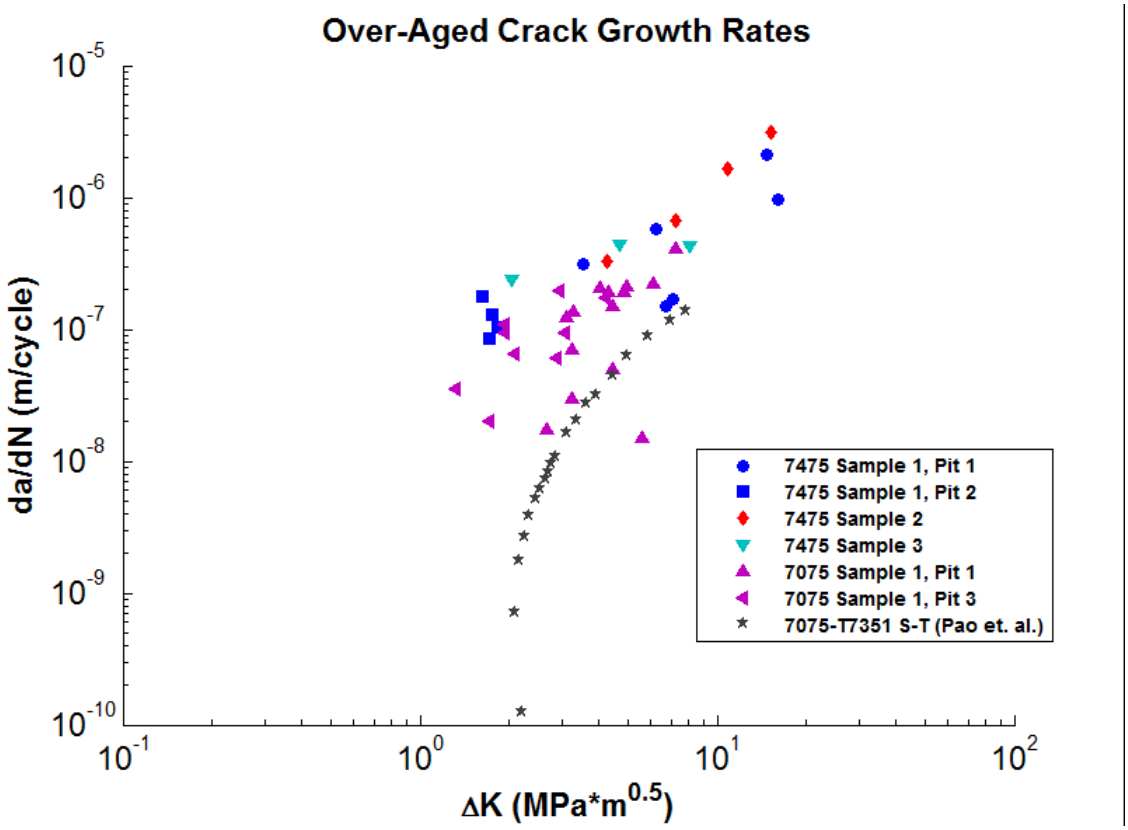

Figure 19*:* Crack growth rate plots of *in situ* tested samples of the over-aged condition. Some of the samples showed crack initiation from multiple pits, while others had crack initiation from a single pit. The reference data was found in [76].

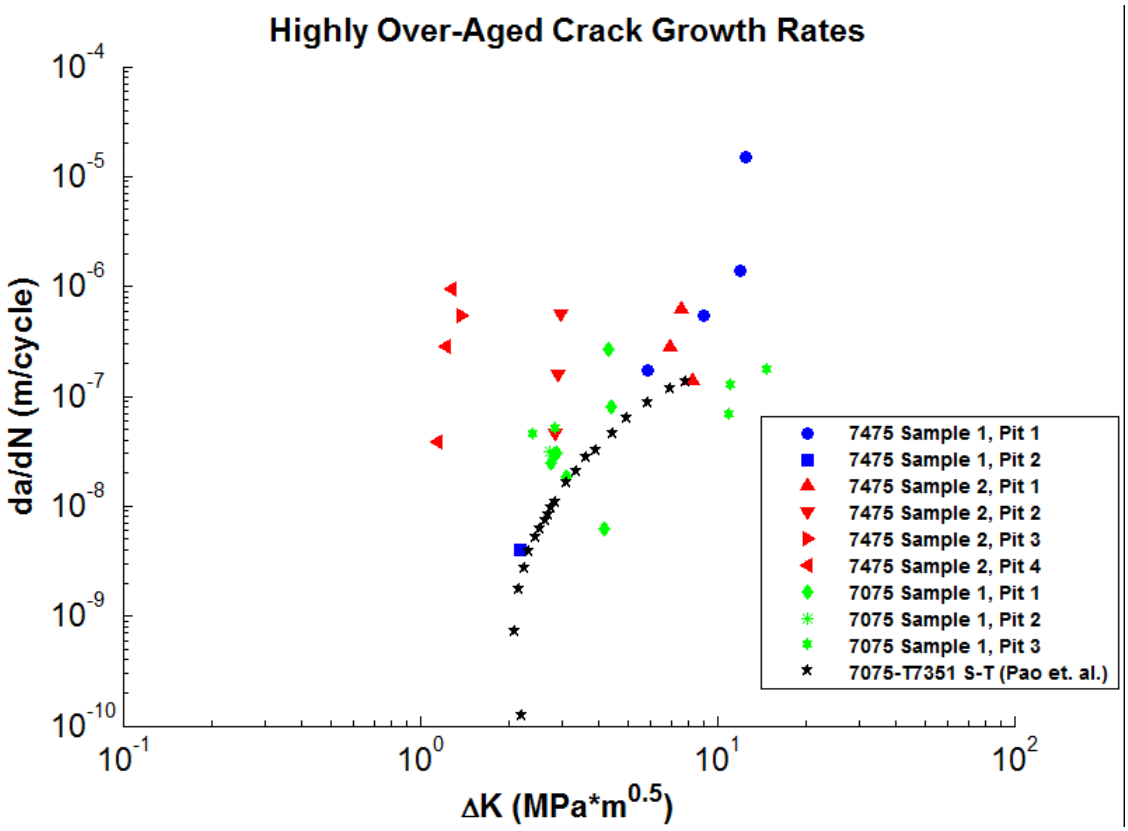

Figure 20*:* Crack growth rate plots of *in situ* tested samples of the highly over-aged condition. The crack growth rates for the highly over-aged samples had more variance than the peak-aged or over-aged samples, which could be explained by competition between multiple large pits within each sample during cracking. The reference data was found in [76].

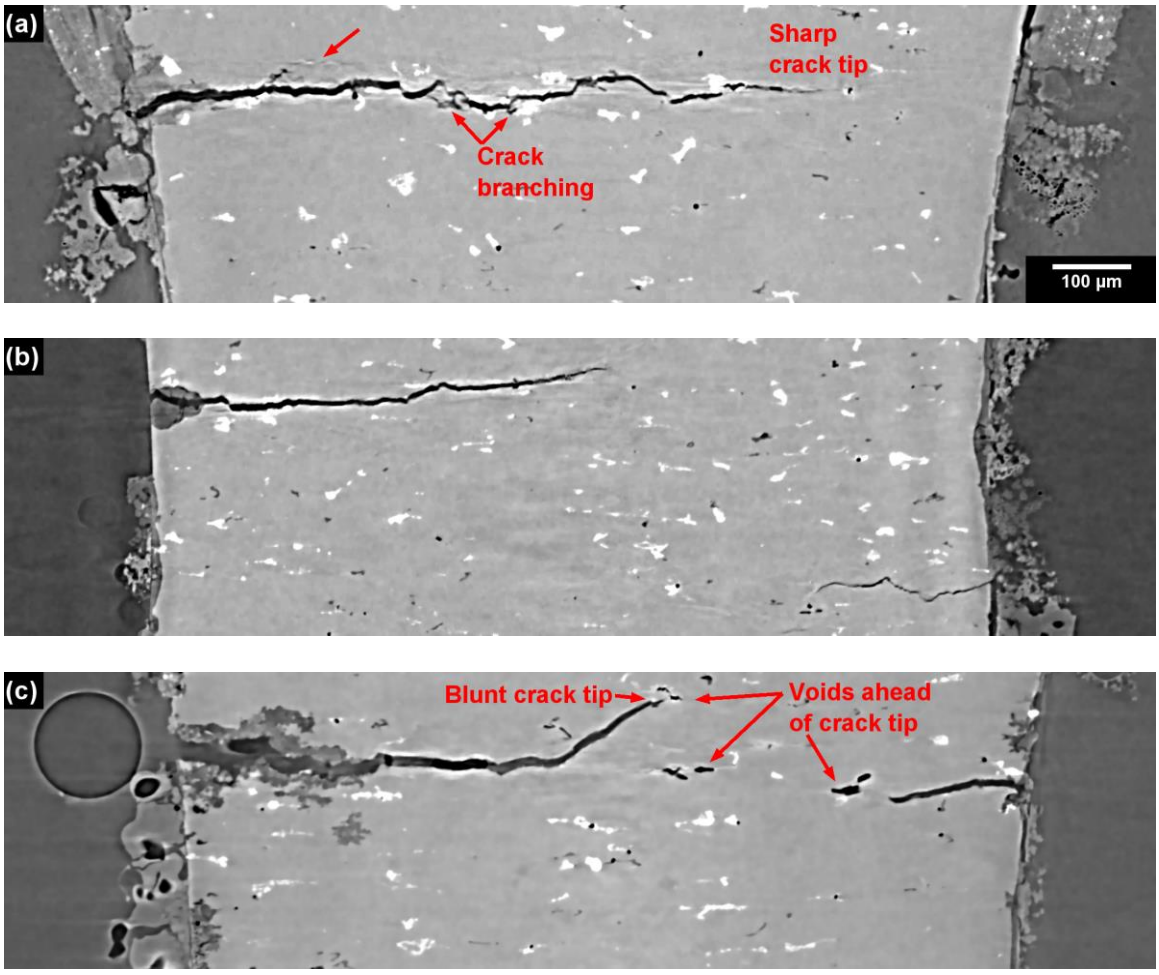

Figure 21: Center XZ plane showing the crack at $0.5\sigma_{max}$ during the last tomography scan before failure. (a) Peak-aged sample showing significant crack branching and a sharp crack tip (ΔK=10.7 MPa•$m^{0.5}$, 46 cycles before failure.) (b) Overaged sample without crack branching and a slightly less sharp crack tip. (for largest crack, ΔK=7.2 MPa•$m^{0.5}$, for smaller crack ΔK=3.8 MPa•$m^{0.5}$, 82 cycles before failure), (c) Highly overaged sample with void formation ahead of the crack tip (for largest crack, ΔK = 8.2 MPa•$m^{0.5}$, for smaller crack, ΔK=2.8 MPa•$m^{0.5}$, 5 cycles before failure).

4.3.3 Overaged Pit Model

The overaged sample depicted in Figure 15(b) and **Figure 17**(a-d) was chosen for 3D finite element modelling due to its numerous pits with different shapes but similar depths. by segmenting the aluminum metal matrix and corrosion pits in Avizo Fire (Waltham, MA, USA), then meshing the segmented data in Altair Hypermesh (Troy, MI, USA) and simulating the sample under the same loading conditions as the experiment in Altair Hyperworks using a 2.6 μm voxel size using a model which took account of plastic deformation. The stress intensity factors of the pits were calculated from the model results using the displacement correlation method listed in [170].

Figure 22 shows the 3D Von Mises stress distribution of the sample surface calculated using 3D tomography data and Hyperworks FEM software. The first pit grew from the exposed region on the sample oriented approximately on the long-transverse face of the sample. This pit was the longest and had the largest reduction of cross-sectional area in the sample, in addition to sharp features near its tip, referred to as micro pits by Burns et. al. [171]. These micro pits along with the large pit depth lead to the highest stress intensity factor in the sample of 2.4 $MPa \cdot m^{0.5}$ and crack initiation was observed from them after 2100 fatigue cycles. Figure 23 shows the region of highest stress in the first pit, along with X-ray tomography slices showing the crack initiation site.

Figure 24 shows the FEM result of the second pit. The second pit had a significantly different geometry, which was more of a “bullet” as described by Turnbull et. al. [137], which may have been partially caused by its position approximately on the short-

transverse face of the sample. This pit had a maximum stress intensity factor of 1.4 $MPa \cdot m^{0.5}$ at the maximum load. Crack initiation was observed in this pit after 2600 cycles. This sample may have shown earlier crack initiation due to its proximity to the first pit, or due to the nearby iron-bearing inclusion, shown in (b), increasing the local stress intensity. The third pit had a stress intensity of $1.5MPa \cdot m^{0.5}$, but crack initiation was not observed until 4000 cycles, at which point the cracks merged from the second pit into the third pit. Figure 25 shows the aluminum matrix after 2,600 cycles and 4,000 cycles of cracking, at which point the crack from the second pit merged into the third pit.

Additionally, the stress intensity factors from the Raju-Newman method before cracking were compared with the simulation. Table 4 provides a comparison of the stress intensity factor in each pit measured from the minimum Z projections and the simulation. A reasonably good agreement was found, with the Raju-Newman method slightly overestimating the stress concentrations. The Raju-Newman estimate may have been higher since it assumes an elliptical geometry that completely encompasses the true pit geometry. To test for an interactive effect from multiple pits within the sample, the sample geometry was modified such that there was only one pit and modeled once for each pit to find the stress intensity factor caused by each pit individually. A slight interactive effect of multiple pits was noted since the FEM results for individual pit models were slightly lower.

Table 4: Comparison of Maximum stress intensity factor of each pit in the corroded sample when loaded to 120 MPa stress in the gauge section.

Pit #	Raju-Newman K	FEM K (MPa·m$^{0.5}$)	FEM K (One pit at a time) (MPa·m$^{0.5}$)
1	2.7	2.4	2.2
2	N/A	1.4	1.3
3	1.9	1.5	1.4

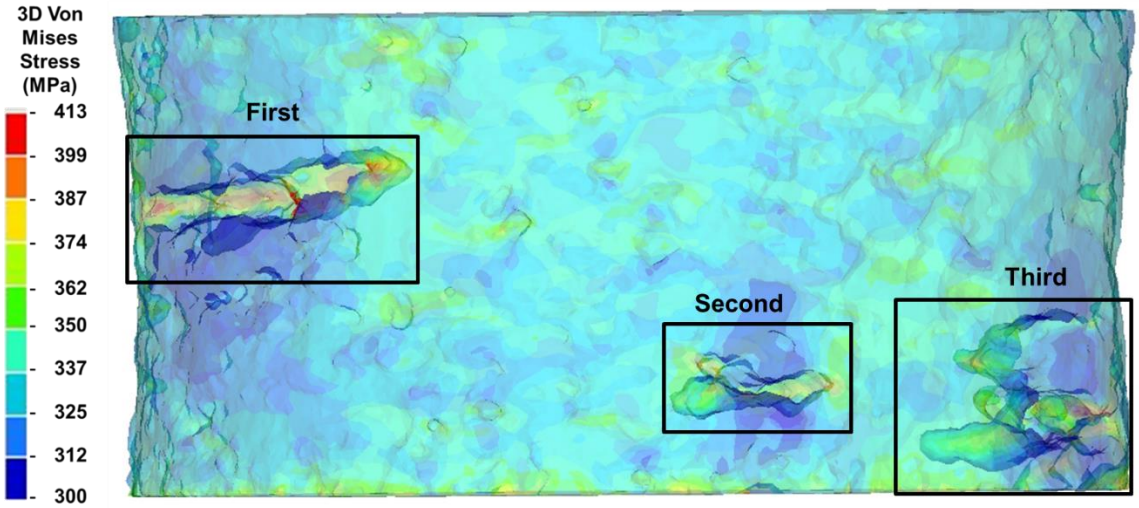

Figure 22: 3D Rendering of Von-Mises stress results for the 3D model of the overaged sample pits. The 3D pit shapes of overaged 7075 alloy can achieve complex geometries due to the influence of microstructural features such as grain boundaries and inclusions on corrosion. Note the annotations corresponding to different pit types.

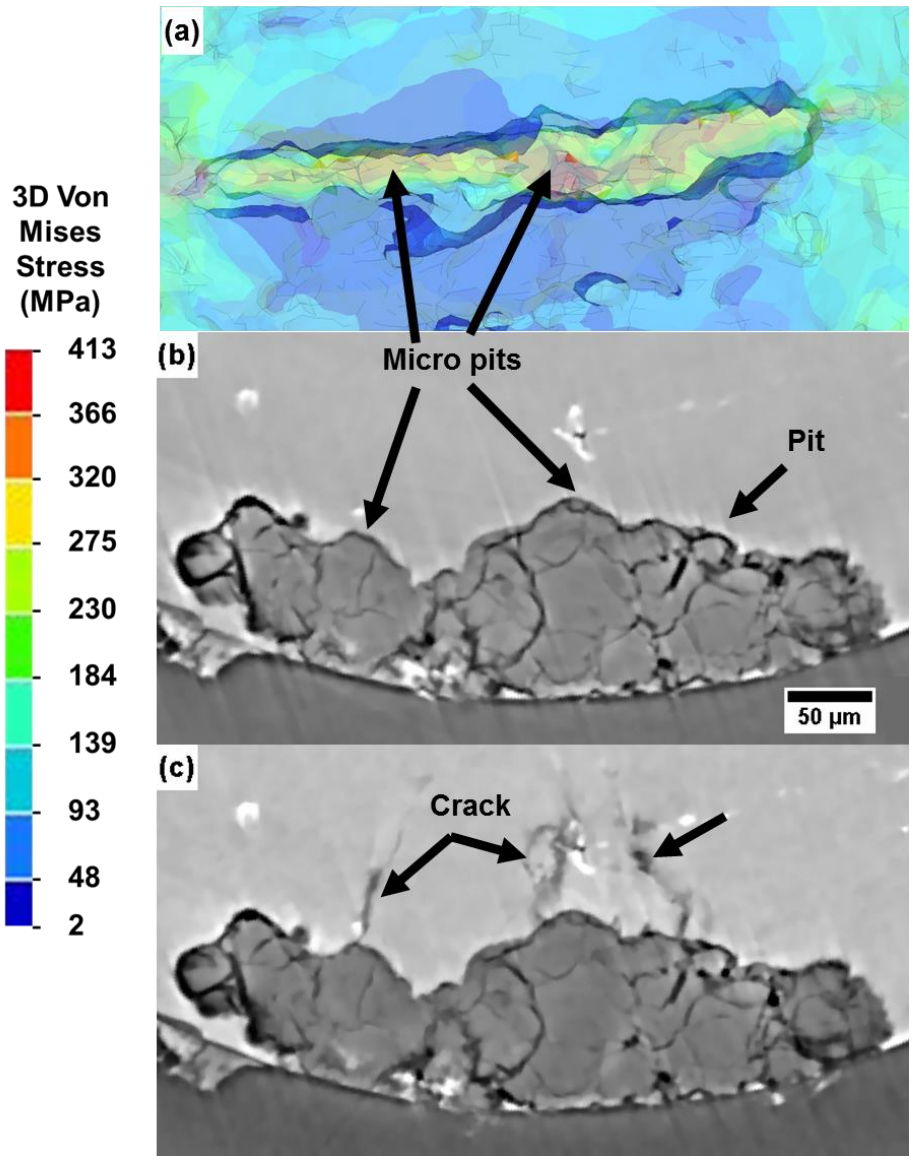

Figure 23: (a) FEM result of first pit with limited stress range displayed showing the pits of maximum stress in the sample used to calculate the maximum stress intensity factor K = 2.5 MPa·$m^{0.5}$. (b) Top-down view tomography slice of the pit in approximately the same position of the maximum stress. (c) Tomography slice of the same region after crack initiation was observed at 2600 cycles of fatigue.

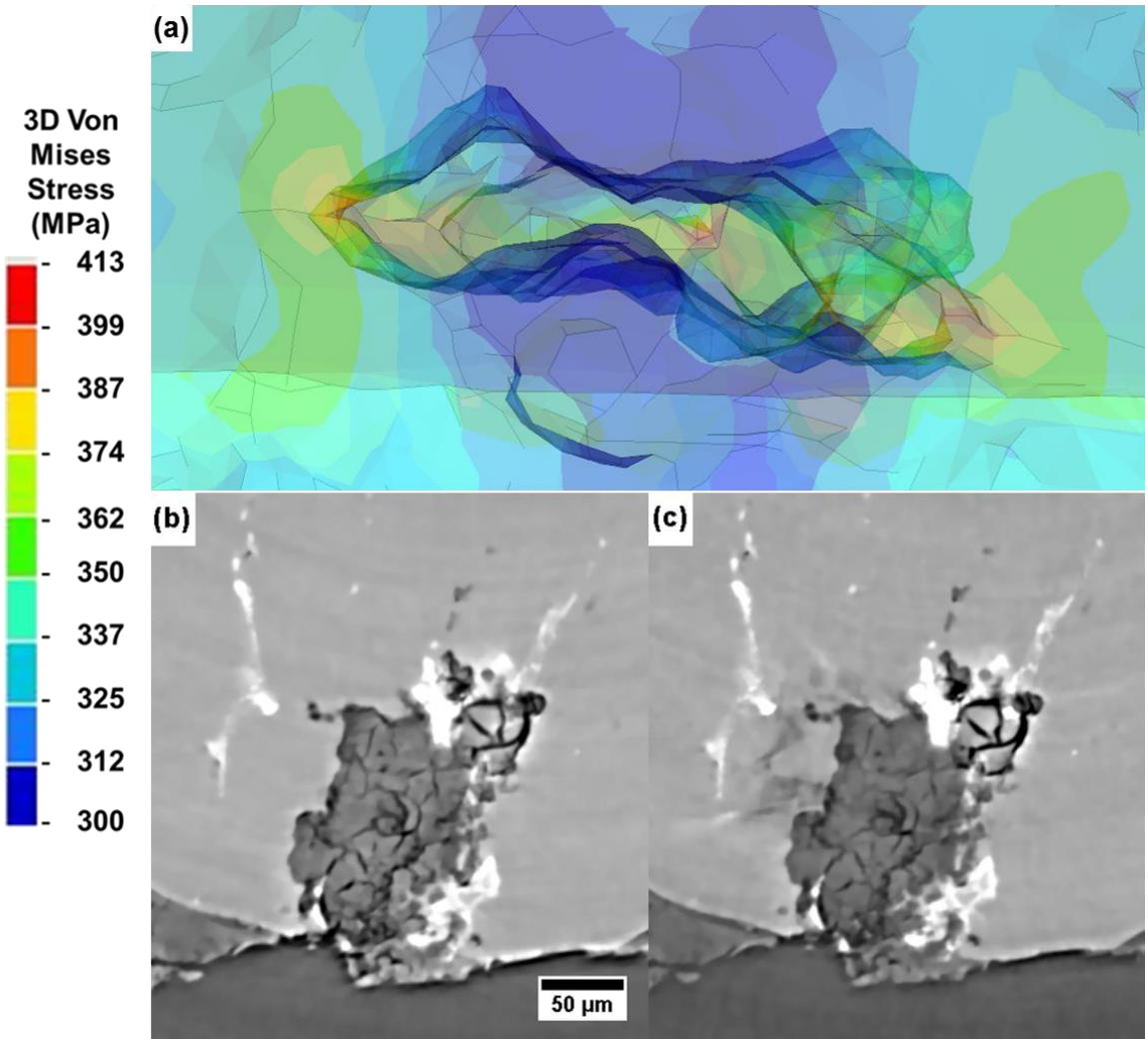

Figure 24: (a) FEM result of the second pit with limited stress range displayed showing the region of maximum stress in the sample used to calculate K = 1.4 MPa·m$^{0.5}$. (b) Top-down view tomography slice of the pit in approximately the same position of the highest stress. (c) Tomography slice of the same region after crack initiation was observed at 2600 cycles of fatigue.

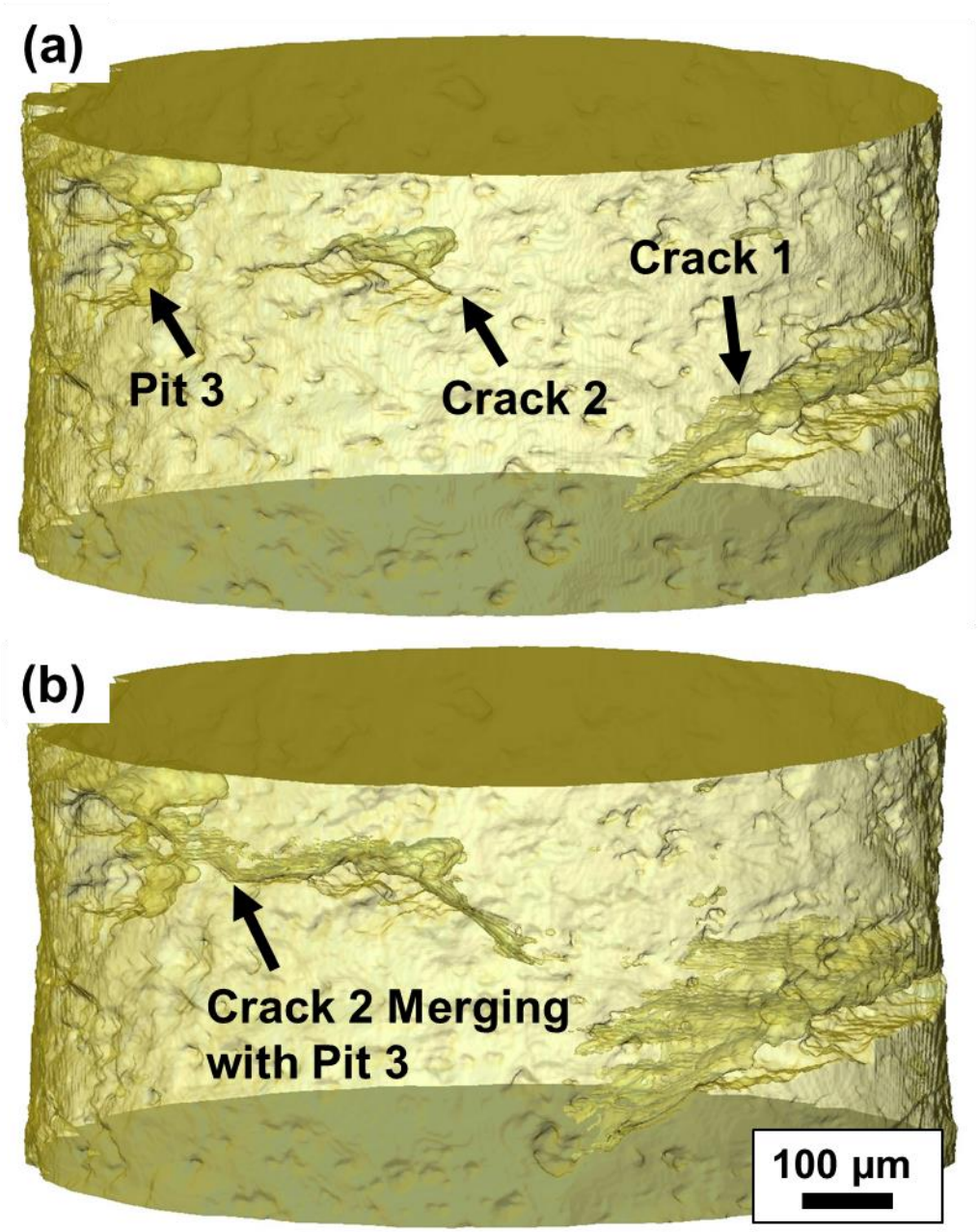

Figure 25: 3D rendering of the aluminum matrix after (a) 2,600 cycles, and (b) 4,000 cycles. Note how the crack from the second pit merges with the third pit after 4000 cycles.

4.4 Discussion

It is well known that aluminum and its alloys are susceptible to corrosion pitting which leads to undesired premature failures [2,3,37]. Changes in aging condition have been known to change pitting and stress corrosion cracking mechanisms [70,76]. For instance, surface studies of pitting have suggested a difference in the maximum pit area for peak-aged versus overaged conditions [70]. Furthermore, recent research has found differences in the frequency of electrochemical pitting events between different aging conditions of aluminum alloys [35]. For some aluminum alloys, the film breaking mechanism has been proposed as the mechanism for corrosion [35,37,48] which involves corrosion via localized breakdown of the passive layer on the aluminum surface caused by adsorption of Cl^- anions from the electrolyte solution on the passive film surface. A change in the dominant corrosion mechanism from film breaking mechanism to an exposed micro-galvanic corrosion mechanism has been suggested with increased aging of aluminum alloys beyond the peak-aged condition as cause for significant differences in corrosion behavior [48].

From the corrosion pit growth results, a significant impact of the aging condition on corrosion pit depths in the 7XXX aluminum alloys was observed, while the inclusion concentration had a less significant effect on the maximum corrosion pit depth. The precipitates may become sufficiently large to form continuous networks along grain boundaries which would allow corrosion pit depths to extend until a discontinuity is reached where precipitates along a line are too far away from each other for corrosion to proceed.

The precipitation sequence in Al-Zn-Mg-Cu alloys is known to proceed from coherent GP zones with ~1.6:1 Mg:Zn ratio to semi-coherent (peak-aged condition) η' with diameter ~1 – 5 nm, to incoherent η (over-aged condition) with diameter ~4 – 11 nm and Zn:Mg ratio closer to 2:1, depending on the exact temperature and alloy composition [30,63,172–176]. When the Al-Zn-Mg alloys are aged above ~190 ^{o}C an incoherent T-phase precipitate of a different crystal structure is formed, while for overaging below 190 ^{o}C larger η plates are formed [173,177]. Based on high resolution TEM research of similar alloys the average radius of the η' precipitates typically observed in peak-aged (T6 condition) Al-Zn-Mg-Cu alloys has been reported to range from ~1 – 5 nm [175,176,178].

Highly over-aged grain boundary precipitates have been shown to form nearly continuous networks along grain boundaries in Al-Zn-Mg alloys [65]. Additionally, the copper concentration in the Al-Zn-Mg-Cu alloy precipitates has been found to increase with increased aging [63]. The increased corrosion susceptibility with increased aging may also be due to depletion of copper from the matrix combined with the enrichment of the precipitates on Zn and Cu leading to increased difference in corrosion potential [55]. Additionally, the incoherent phase change may weaken the passive film which forms at the interface between the precipitates, leading to faster corrosion [173,177]. Hence, corrosion via proceed via a multitude of micro-galvanic cells between precipitates and the precipitate free zone combined with the enrichment of the precipitates and Cu leading to increased differences in corrosion potential for the highly overaged alloy relative to the peak-aged and overaged alloys [55]. Therefore, corrosion most likely proceeds via a

multitude of micro-galvanic cells between networks of precipitates and the matrix in the highly overaged alloys, whereas the peak-aged alloy would have coherent precipitates which allow the passive layer to remain relatively strong and resistant to corrosion, and dissolve preferentially and discretely at the grain boundaries. In the overaged condition, there may also be a chance for continuous precipitates at grain boundaries, but the probability is much lower due to the smaller precipitate size on average.

These changes in precipitate morphology also affected the fatigue properties of the aluminum alloy. The fatigue crack growth rates showed that near crack initiation, the crack growth in the miniaturized samples was much faster than the long crack data. Since the samples had 1 mm diameter with grain dimensions on the order of 300 μm – 770 μm depending on direction and ~ 5 μm subgrains, as measured by etching, the cracks studied herein could be considered both microstructurally small (as long as only the primary grains and not the sub-grains are considered), as well as physically small [179,180]. Therefore, this faster crack growth may have been caused by the short crack length on the order of hundreds of micrometers [13,137,179,181,182]. As the crack growth proceeded, the cracks grew longer and their growth rates grew closer to that of the data reported in literature. It can also be noted that the scatter of the data increased with increased aging time, which may be ascribed to the fact that the pit depth was considerably more stochastic in the overaged samples compared to the peak-aged samples, which showed a relatively uniform pit depth, or possibly due to interaction effects caused by cracks from different pits interacting with each other during the crack growth. Higher observed stress intensity factors in the finite element simulation than the Raju-Newman estimates from

measurements of the Z-projections suggests that the complex pit shapes and interactions between the pits do play roles in reducing the crack initiation life. Significant differences in crack shape were also observed, as shown in **Figure 21**. The crack tips of the peak-aged samples were much sharper than those of the over-aged and highly overaged samples. Vasudevan and Suresh have observed this difference in crack tip sharpness in stress corrosion cracking data, and attributed it to a change in slip mode from planar slip for peak-aged alloys to wavy slip for over-aged alloys [183]. Additionally, the peak-aged alloy is more susceptible to hydrogen embrittlement [184] which may lead to a decreased dependence upon microstructural features such as grain boundaries and inclusions, and increased dependence on dislocation-precipitate interactions during fatigue crack growth [185,186]. The highly over-aged sample had a very blunt crack tip with high CTOD and void formation ahead of the crack tip near failure. This tendency toward void formation was a clear sign of a change in fracture mechanism from brittle to ductile, with decohesion of the matrix from the inclusions near failure. The transition from brittle cracking mechanisms to ductile behavior depicted in **Figure 21** was due to a change in dominant dislocation-precipitate interaction mechanisms, since in the bulk of the highly overaged alloy fewer particles with larger radius exist, leading to decreased strengthening from Orowan looping as the aging continues beyond peak-aged.

4.5 Summary

7075 samples of different aging conditions were prepared by corrosion in 3.5 wt% NaCl solution for 15 days, then fatigue tested *in situ* using X-ray synchrotron

tomography. The pit geometry and fatigue crack growth progress were examined in 3D. This study yielded valuable insights regarding the shape of corrosion pits within the rolled Al7XXX plates, and their effect on fatigue crack initiation. Since samples of different aging condition were also examined, the effect of precipitates on the corrosion pitting was also analyzed. Moreover, using the *in situ* testing, the effect of corrosion pits on the corrosion fatigue crack growth process was also investigated.

1. Highly overaged 7075 has much larger pits than peak-aged and overaged 7075 when corroded in uncovered 3.5 wt% NaCl solution. This is most likely due to changes in precipitate chemistry with respect to the matrix causing increased nobility of the precipitates compared to the matrix, leading to rapid anodic dissolution of the precipitate free zones to greater depths within the sample via an intergranular corrosion mechanism.
2. A correspondence between rolling orientation and pit shape was observed. This lead to different stress concentrations at the center for pits on the longitudinal face, and stress concentrations at the side of the pits for the transverse face.
3. A change in fatigue crack failure mechanism from brittle failure with a sharp crack tip to microvoid formation ahead of a blunt crack tip was observed with increased aging of the samples.
4. The fatigue crack growth rates showed increasing scatter with increased aging, which may have been due to a reduction in hydrogen embrittlement effects coupled with an increased dependence of the fatigue crack growth rate on microstructural features such as the larger pits. 3D finite element models of the

sample with all the pits compared to models with one pit each provided further evidence for the interactive effects of multiple pits within the sample.

5 3D OBSERVATIONS OF CORROSION FATIGUE CRACK GROWTH OF 7475-T6 WITHIN A FATIGUE CYCLES

5.1 Introduction

Corrosion pits are known to affect fatigue crack initiation and growth properties in aluminum alloys [90–92,125,171,187,188], leading to premature failure in aircraft [2–5]. Additionally, in corrosion-fatigue the local chemistry can be affected by the cracks path. For instance, inclusions, aluminum crack faces and grain boundary precipitates can interact with the solution within the crack to reduce the local pH and produce hydrogen gas bubbles [16,17,82,134]. Furthermore, the crack opening and the tortuous nature of the crack morphology may also affect the local fluid flow within the crack tip and serve to change local crack tip chemistry and crack growth rates. Therefore, the corrosion-fatigue crack initiation and growth were examined in a 7475-T6 sample using in situ three dimensional (3D) X-ray tomography. Scans were taken within the fatigue cycles to examine the corrosion bubble movement during fatigue and gain understanding of the corrosion within the fatigue crack.

5.2 Materials and Methods

This sample was tested and heat treated in the same fashion as described in Chapters 1 and 2. For this test, the sample was tested at σ_{max}=120 MPa, R=0.1, and the testing was paused at ~0.1 σ_{max}, then scanned, then at 0.55 σ_{max}, then scanned at $\sigma_{max,}$ and again at 0.55 σ_{max} and 0.1 σ_{max} on the unloading portion of the fatigue cycle. This allowed for observation of bubble movement and crack growth within a fatigue cycle.

5.3 Results

The high-quality data obtained within the fatigue cycle and before fatigue testing allowed clear observation of the interactions between cracks, pits, and inclusions.

Figure 26 (a) shows a virtual slice through the cross-sectional area of the sample in which inclusions, bubbles, cracks, and pits can be clearly seen. Note that the crack appears discontinuous from this perspective in 3D but is continuous in 3D, indicating the need for this type of 3D study to observe crack growth.

Figure 26(b) shows a minimum projection along the height of the sample. From this, the bubbles can be seen much more clearly and the crack front appears relatively straight since the sample was near failure.

Figure 27 shows a slice parallel to the height of the sample in which the cracks, bubbles, inclusions, pores, and pits can be clearly seen. Note that secondary cracking was observed in this sample. Since this sample was pre-corroded, there were many stress concentrators present in the sample due to the formation of corrosion pits. Figure 28(a) shows a 3D greyscale volume rendering of the corroded sample surface before corrosion-fatigue. Figure 28(b) shows the same volume rendering with regions which were clearly identified as corrosion pits highlighted in green, and the crack after 5,150 cycles in blue. From this, it appears that the crack may have preferentially grown along the corrosion pits.

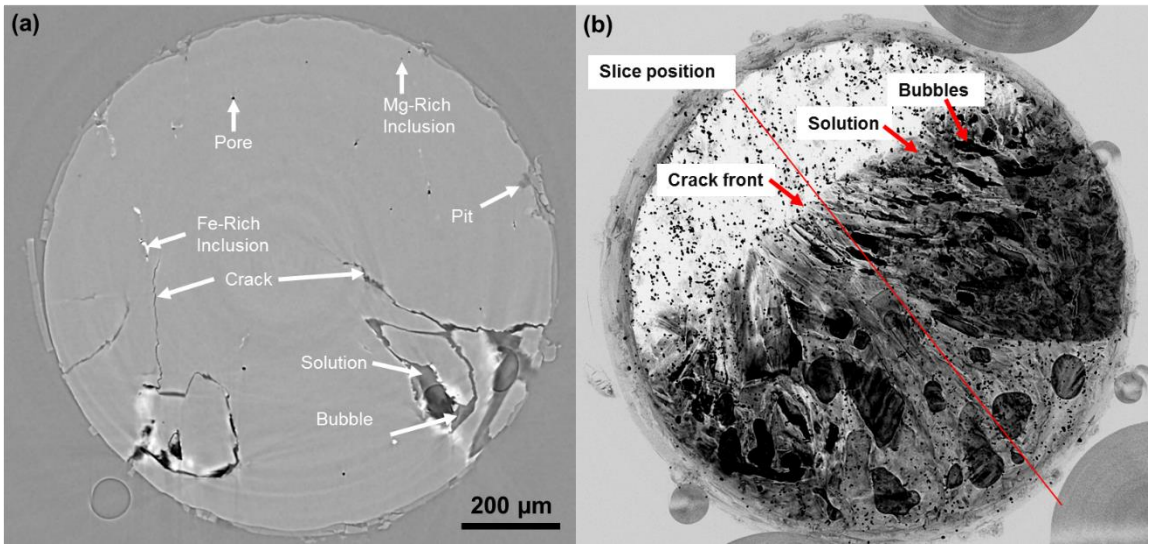

Figure 26: 3D X-ray synchrotron scan data of Al7475-T6 sample taken shortly before failure after 5,398 fatigue cycles at 70 MPa stress. (a) Virtual slice through the thickness of the sample clearly shows microstructural features including the crack, bubbles pores inclusions, and pits. Note that the crack appears discontinuous in 2D because of its tortuous path through the sample, but is connected in 3D. (b) Projection of the data minimum values along the height of the dataset shows the bubble shape much more clearly, and the crack front is relatively straight in 3D near failure.

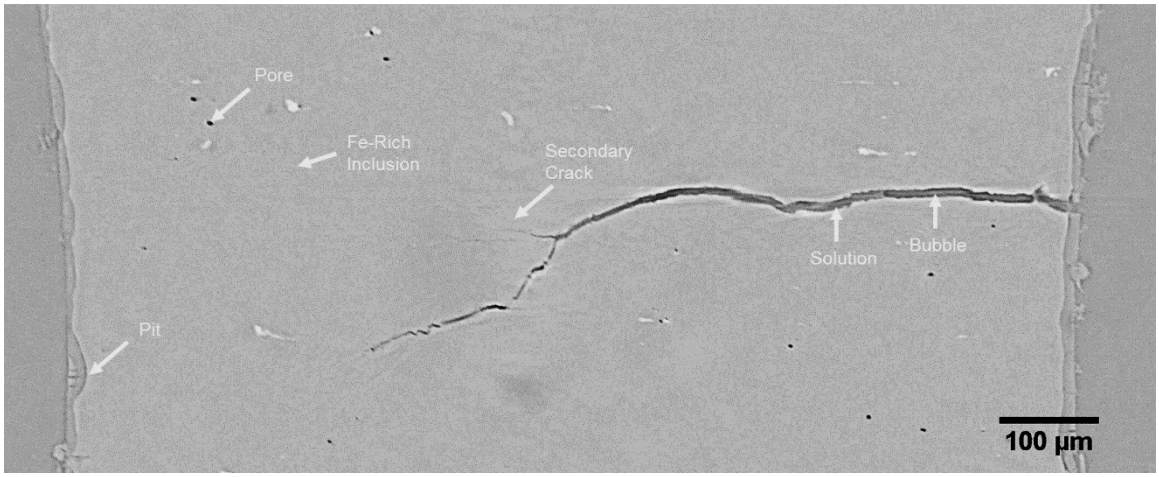

Figure 27: Virtual slice parallel to the height of the sample closest to failure after 5,398 cycles of fatigue at a stress of 70 MPa. Note the relevant microstructural features in the sample including inclusions, pores, cracks, pits, and bubbles.

Figure 29(a) shows a higher magnification view of the sample volume rendering overlaid with segmented data of the crack after 4,000 cycles (the first 3D scan taken after crack initiation). From Figure 29 the corrosion-fatigue crack initiated at a pre-existing crack within the corrosion pit. Overlaying the segmented pit data in Figure 29(b), it appears that the crack grew and branched near initiation because two pits were close to each other and at different heights along the sample. Figure 30(a) shows a secondary electron image of the top crack face. Comparison of the crack surface with the peak-aged sample in Chapter 2 suggests this sample's crack path was much more dependent on crystallographic features than the peak-aged sample due to the significantly reduced concentration and size of the inclusions in the peak-aged 7475 alloy. Figure 30(b) shows a high magnification image of the crack's point of initiation. In Figure 30(b) the initiation can be clearly seen to occur at a sharp "jut-in" at the tip of the corrosion pit. The fact that the jut-in and the crack in the corrosion product overlap may mean that the cracks within the corrosion product lead to local crevices which create faster corrosion and sharper pits due to decreases in pH caused by accumulation of dissolved metal ions within the crevice.

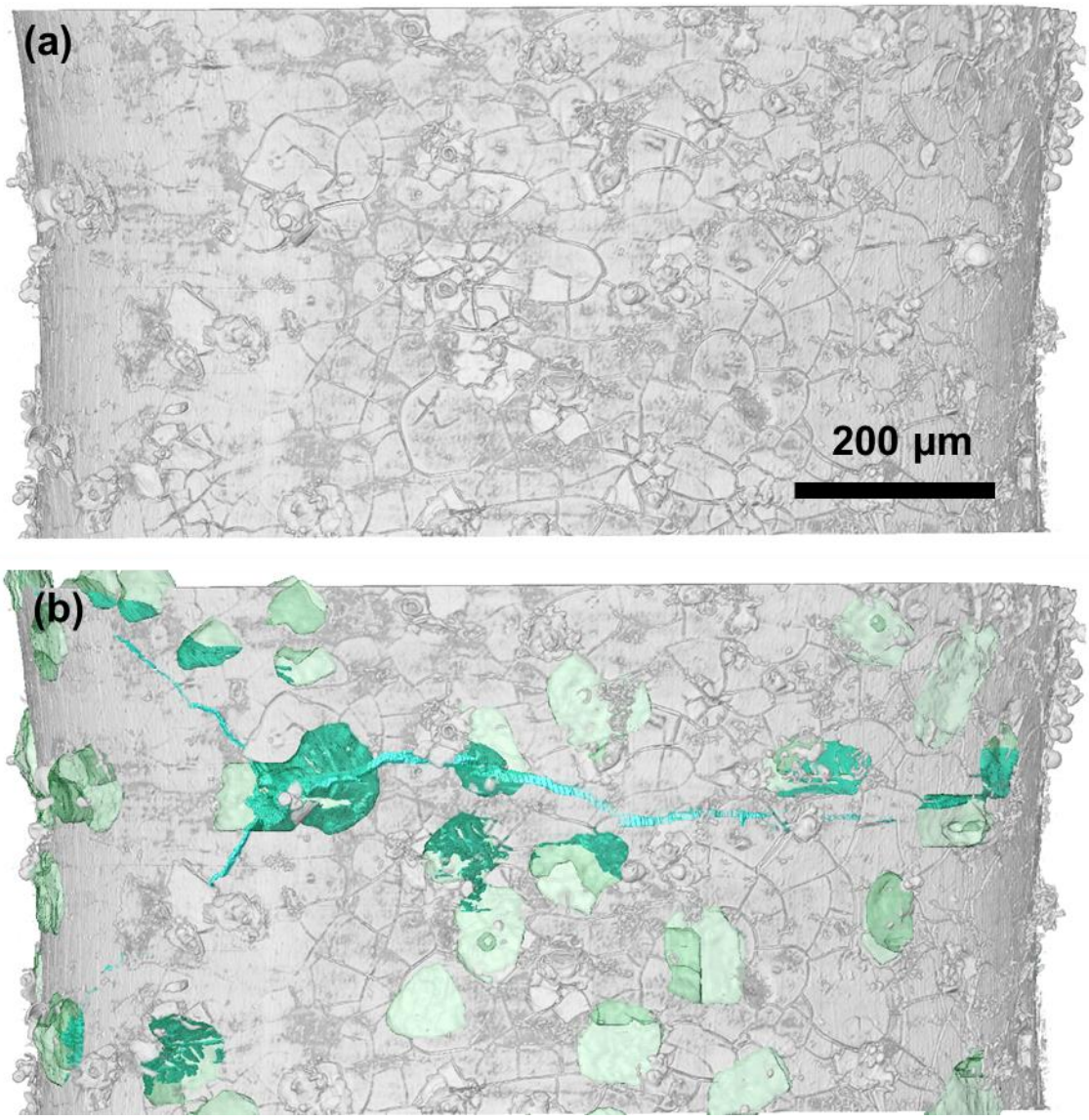

Figure 28: (a) Grey scale 3D volume rendering of one face of the sample before fatigue testing. (b) the same 3D rending with the pits and a rendering of the crack overlaid after 5,5150 cycles of fatigue. The crack appears to follow the pits.

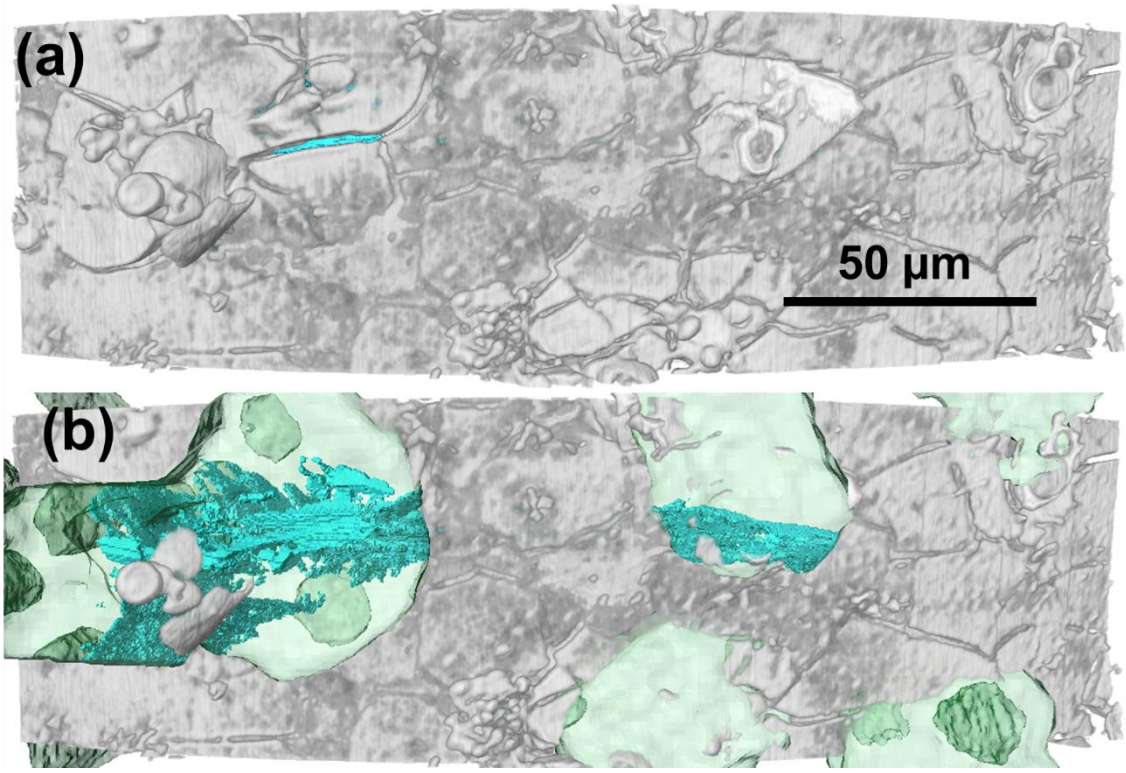

Figure 29: High magnification 3D renderings of the sample face where the crack initiated. (a) the corroded sample had a “mud-crack” within the corrosion pit before fatigue testing. The blue is a rendering of the first resolved fatigue crack at 4,000 cycles, clearly showing that the crack initiated at this pre-existing crack within the corrosion pit. (b) A clear overlay of the corrosion pits on the sample face provides a view through to the crack, which clearly shows that the crack initiated and branched from one combined pit, then grew into another pit nearby.

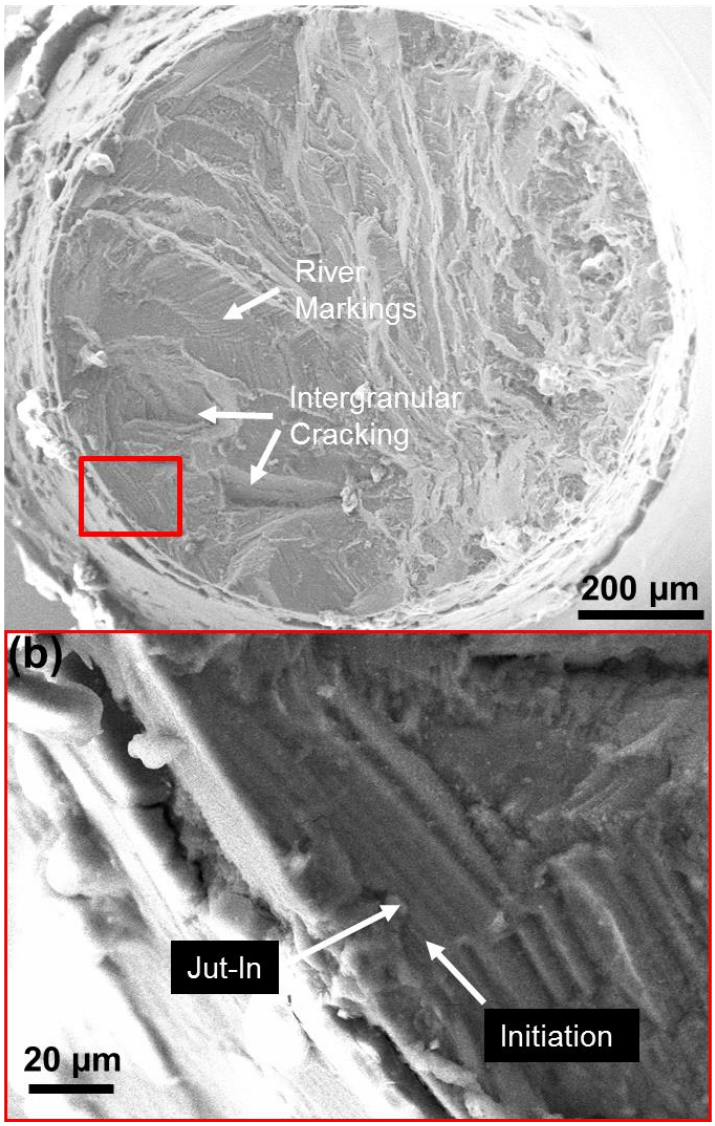

Figure 30: (a) Low-magnification 25 kV secondary electron image of the fracture top surface with initiation region outlined in red. Note features which suggest highly crystallographically dependent fracture such as river markings and possible grain pullout sites. (b) higher magnification image of the initiation site showing the pit initiated from a micro pit within the corrosion pit.

Since scans were taken within fatigue cycles and bubbles could be clearly observed within the crack, a preliminary 3D analysis was performed on the cracks and bubbles via segmentation and 3D renderings. Figure 31 shows 3D renderings of the sample at 5 points within the 4,600th fatigue cycle, just 600 cycles after crack initiation was first observed within this sample. Bubbles were visible within the crack. Some bubble movement and shape changes were detected, with the bubbles going from small localized regions at low load to more rounded shapes at higher loads. Figure 32 shows 3D renderings of the sample during the 5,150th cycle. In Figure 32, the changes in bubble position can be seen more clearly. The elongated bubble shapes suggest that they conform to the rough surfaces of the crack. At lower loads, the bubbles remained closer to the crack initiation site. At the maximum load, the bubbles expanded into the branches of the crack. This suggests that the localized corrosion and fluid flow within the crack may be dependent on many factors such as crack face roughness caused by microstructural features. Figure 33 compares the bubble volumes as a function of stress within the load for the 4,600th and 5,150th cycle. In Figure 33(a) a loose correlation between bubble volume and load can be seen. Figure 33(b) shows a much closer relationship between load and bubble volume, with the bubble volume increasing slightly between the loading and unloading of the cycles.

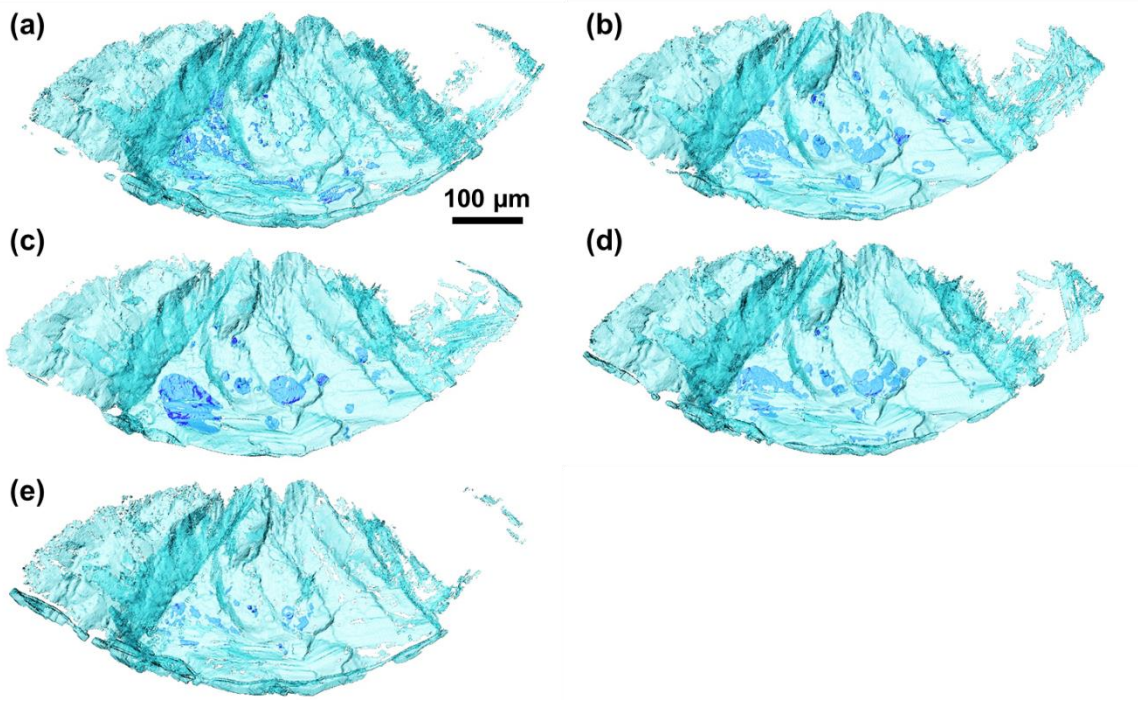

Figure 31: Top-down view 3D renderings of the 4,600th cycle of the crack (light blue) and bubbles (dark blue) during loading at (a) 11 MPa, (b) 70 MPa, (c) 120 MPa, and during unloading at (d) 70 MPa, (e) 11 MPa. Note the bubbles move slightly during loading, going from very small localized shapes at low load to larger, more spherical shapes at higher load.

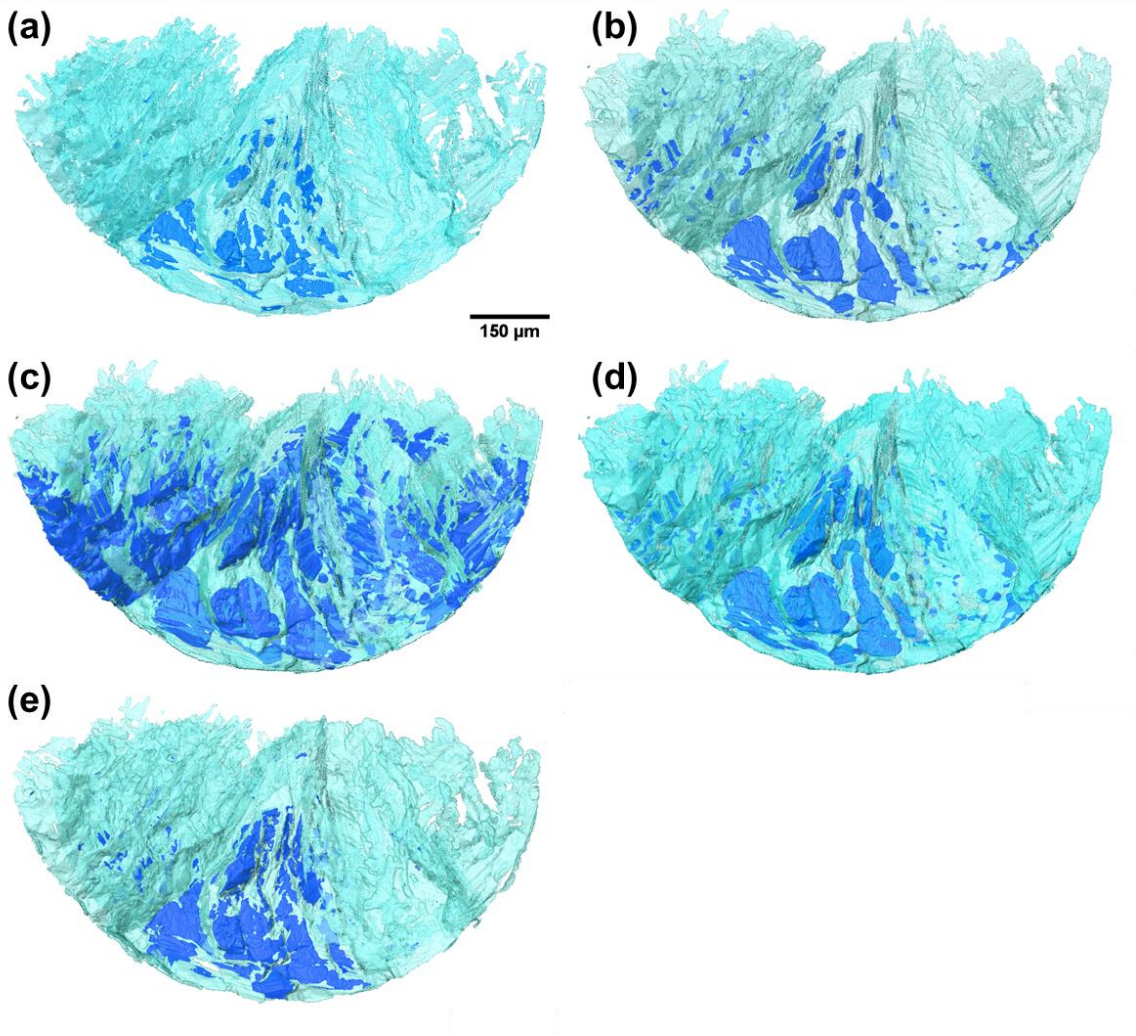

Figure 32: Top-down view 3D renderings of the 5,150th cycle of the crack (light blue) and bubbles (dark blue) during loading at (a) 11 MPa, (b) 70 MPa, (c) 120 MPa, and during unloading at (d) 70 MPa, (e) 11 MPa. Not the significant bubble movement within the crack, with the bubbles moving to the periphery of the crack at max load, and agglomerating at the center of the crack closer to the initiation feature at the minimum load.

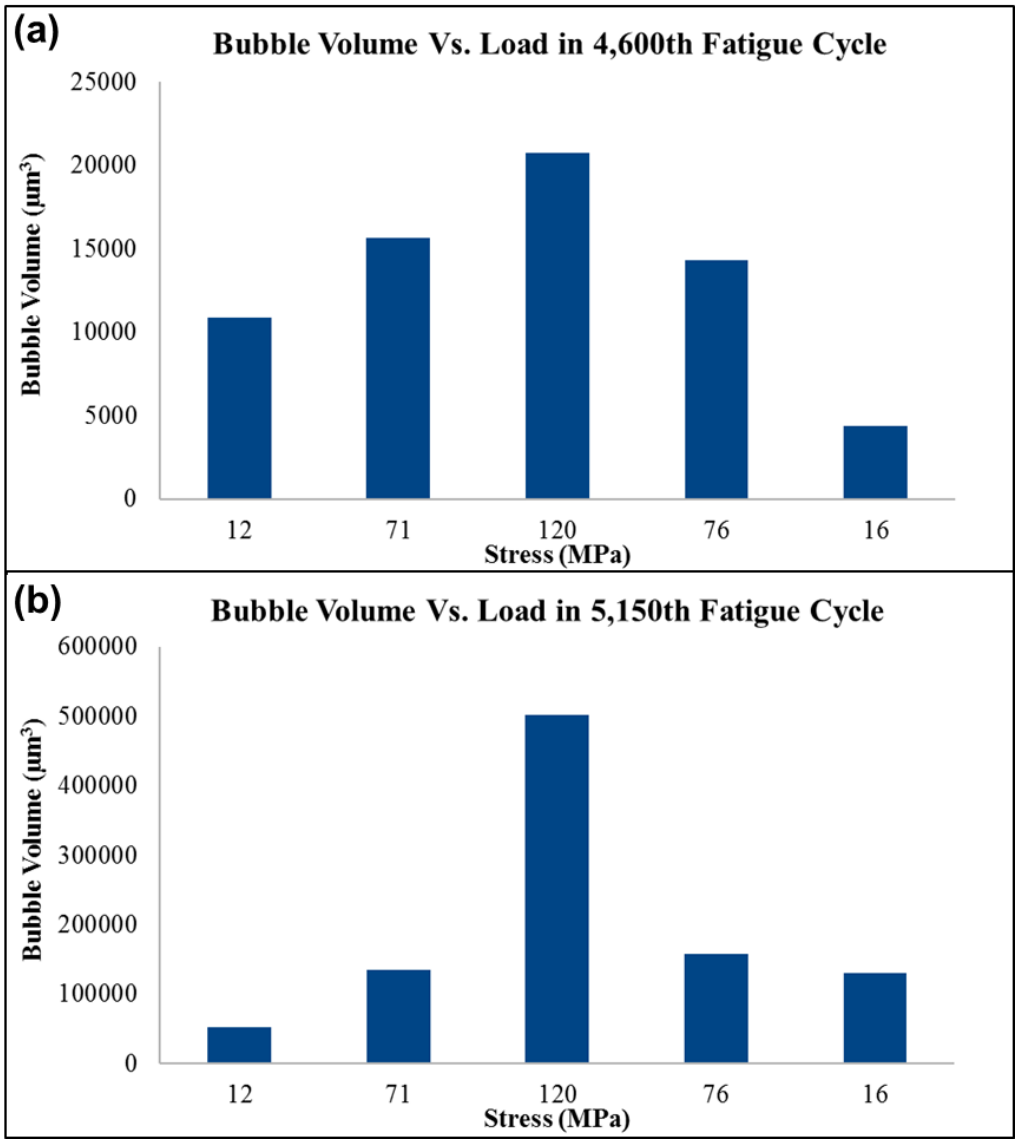

Figure 33: Bubble volume within the fatigue crack as a function of stress after (a) 4,600 cycles and (b) 5,150 cycles. Note that the change in bubble volume is much more significant for the higher load. This may be due to the higher CTOD at the higher load in addition to greater surface tension effects on the bubbles at lower CTOD limiting their movement.

5.4 Summary

In this experiment the corrosion-fatigue of corrosion pitted 7475-T6 was analyzed within the fatigue cycles. The fatigue crack was determined to initiate from a pre-existing crack within the corrosion product, which also contained a pit underneath. The pit had a sharp tip, or "jut-in," which may have been due to preferential corrosion surrounding the inclusion or due to a local crevice forming at the crack within the corrosion product leading to faster corrosion. Additionally, the crack appeared to follow along the corrosion pits on the sample surface. The crack face also showed significant presence of river markings, indicating that this sample's fracture may have been more dependent upon crystallographic features such as grain shapes and orientations than the 7075 alloy, which had a much flatter crack face with many inclusions and secondary cracks clearly visible on the fracture surface. Analysis of the bubble volume changes within the crack during a fatigue cycle near crack initiation and near failure suggested that the bubble positions and volumes change significantly during a fatigue cycle. This change is most likely a function of the local crack tip opening displacement. Further analysis should quantify the bubble's relationships dependence on crack tip opening displacement, and also use focused-ion beam to measure the corrosion product depth at selected locations along the crack face to examine the relationships between localized crack face corrosion product volumes and bubble volumes. Such an analysis could lead to improved understandings of crack tip chemistry and its effect on local crack growth rates.

6 HIGH RESOLUTION MULTIMODAL OBSERVATIONS OF CORROSION INITIATION IN AL7075-T651

6.1 Introduction

Most of the studies to date have focused on corrosion growth over relatively long periods of time from hours to days, or used electrochemical techniques to observe corrosion initiation. Corrosion initiation has been examined in AA2024-T3 and found valuable results regarding the effects of intermetallic particles using a variety of techniques [160,161,163,189–192]. The shape of corrosion damage after brief durations (less than one hour) can provide valuable insights regarding corrosion initiation which may aid in future alloy designs for reduced corrosion. With the advent of higher resolution techniques for measuring changes in sample height becoming easily accessible, opportunities have been presented for gaining an even greater depth of information regarding the initiation of corrosion pits in aluminum alloys. Therefore, focused ion beam scanning electron microscopy (FIB-SEM), energy dispersive X-ray spectroscopy (EDS), and electron backscatter diffraction (EBSD) data were coupled with vertical scanning light interferometry (VSLI) to study the corrosion initiation progression at the surface of an aluminum alloy. For the first time, the elevation changes due to corrosion have been measured with respect to grain orientation during corrosion initiation in 7075 alloys. This combined technique provided microscopic chemical composition, grain boundary information, and nanoscale corrosion rate information to determine their effects on morphological evolution of corrosion initiation of 7075-T651 exposed to 3.5 wt.% NaCl solution.

6.2 Materials and Methods

A sample was cut from the center of a 3” 7075-T651 plate such that the short and transverse directions were exposed. The aluminum sample was mounted in epoxy beside a sample of chemically-inert polytetrafluoroethylene (PTFE) plastic. The sample was gently wet-sanded using 600 grit sandpaper, then 1200p4000 sandpaper, then 1 µm diamond paste with methanol lubricant, and finally 0.05 µm colloidal silica. Several attempts were made to polish the sample using 0.05 µm diamond paste using various pressures and polishing times, and then perform EBSD scanning, but it was determined that the chemical-mechanical effect of the basic (pH ~8.8) colloidal silica solution was required to obtain a high quality EBSD pattern in the 7075 alloy.

The sample was briefly washed and dried, then all nonconductive surfaces of the sample were covered with copper tape to ensure a conductive circuit for SEM analysis. The sample was analyzed using a Zeiss Auriga FIB-SEM equipped with an Oxford Instruments (Abingdon, Oxfordshire, UK) AzTec EDS system for compositional analysis and an EDAX (Mahwah, NJ, USA) electron backscatter diffraction (EBSD) system for orientation analysis. After SEM analysis, the sample was briefly polished for 30 s using 0.05 µm diamond paste with methanol lubricant, then rinsed and dried, to reduce surface carbon contamination from the electron beam in the SEM as well as any remaining chemical contamination from the colloidal silica solution.

The initial sample heights were imaged using the VSLI to gain baseline elevation measurements, then 3.5 wt.% NaCl was deposited onto the sample at a flow rate of 14.5

mL/min for ten minute increments. The sample was rinsed, dried, and imaged using VSLI with a vertical resolution of 0.2 nm and lateral resolution of 80 nm after each interval. Figure 34 shows the corrosion and sample setup. Note that the sample was loaded into a kinematic mount to preserve the imaging position when moving the sample between corrosion and VSLI time steps. The corrosion at each time point was subtracted from the initial reference to gain average corrosion rate measurements for each point in the region of interest, as shown in Figure 36.

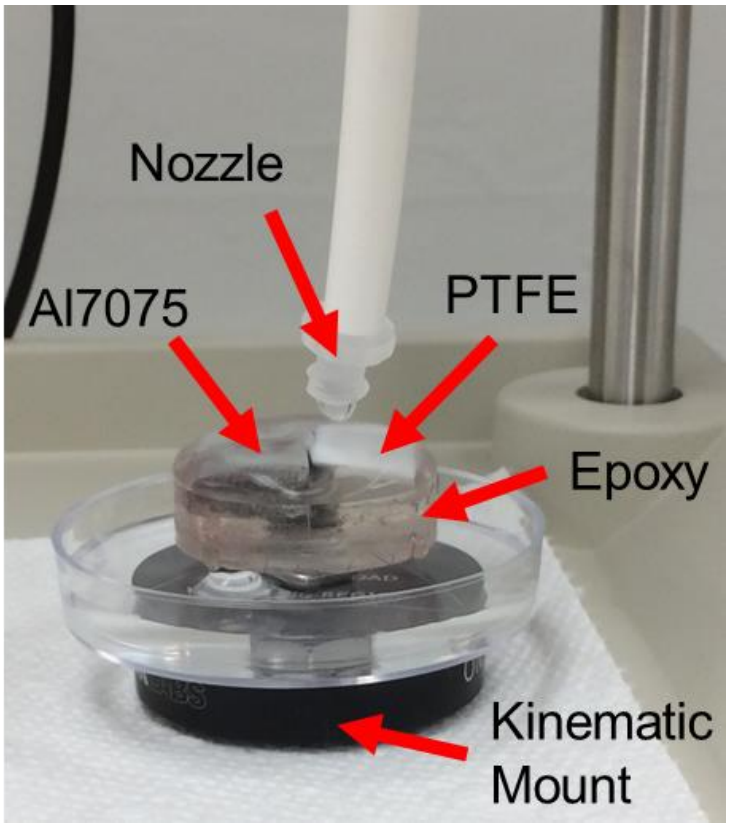

Figure 34: Sample and corrosion setup for the VSLI experiment.

After corrosion, SEM imaging and EDS spot analysis of the inclusions were performed. An Fe-bearing and an Mg-bearing inclusion were each selected for FIB-SEM cross-section analysis. Pt was deposited using low FIB current to protect the fragile corrosion initiation layer during later FIB cross-section milling. FIB cross-section analysis of the inclusion/matrix interface was performed.

6.3 Results

Table 5 shows the composition of the 7075-T651 sample surface tested in this study. Figure 35 (a) shows an InLens material contrast SEM image, in which inclusions and dispersoids can be resolved. Figure 35 (b) shows the pre-corrosion EDS analysis result, indicating the presence of Mg-rich, Fe-rich, and Cu-rich inclusions which all play unique roles during corrosion of aluminum alloys. The Fe and Cu rich inclusions can cause trenching in the surrounding matrix, while the Mg rich inclusions dissolve preferentially. A variety of grain orientations were also examined in the study, as indicated by the EBSD pattern in Figure 35 (c).

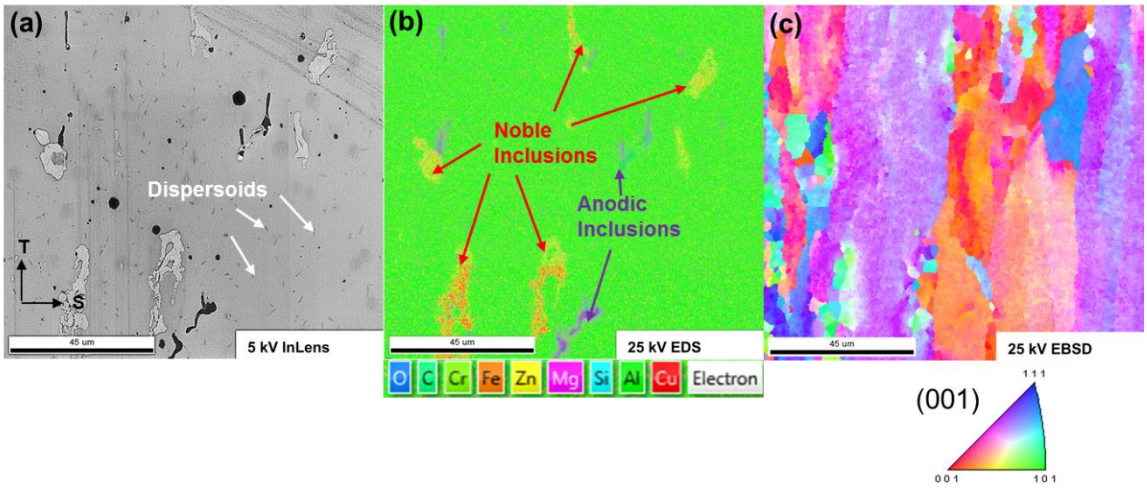

Figure 35: The material region of interest shown using (a) 5 kV InLens (material contrast) SEM (b) 25 kV EDS dot map dot map of region composition and (c), 25 kV EBSD pattern of the same region before corrosion.

Table 5: Composition of 7075-T651 sample measured by energy dispersive X-ray spectroscopy.

Element	**Al**	**Zn**	**Mg**	**Cu**	**Fe**	**O**	**Si**	**Cr**
Concentration (wt. %)	88.4	5.66	2.46	2.03	0.53	0.53	0.21	0.21

Considering that most of the noble inclusions were of similar composition (Fe and Cu rich), the inclusion corrosion rates could depend partially upon the grain orientation in which they reside. Careful examination of the 10 minute rate image in Figure 36 shows that the boundaries between the noble inclusions and the matrix corrode first, which may be a difference in corrosion potential from precipitates accelerating the corrosion rate. Moreover, it is interesting to note that the Mg_2Si inclusions show miniscule height changes with the VSLI technique, but it is known from tomography and EDS that the Mg_2Si inclusions corrode and lose density rapidly. Note from comparison of Figure 35 (c) and Figure 36 that comparison of the EBSD grain orientation map and the corrosion rate show what appears to be a very loose correlation between increased corrosion rates and grain boundaries. Figure 37 shows an increased contrast view of the matrix with the grain boundaries calculated from the EBSD map overlaid. Two grain boundaries were selected for the profile plot in Figure 37 (b), which shows that the grain boundaries clearly had less elevation change than the matrix after 60 minutes of corrosion. Additionally, comparison of Figure 35 (a) with Figure 37 (a) shows that the small particles which are most likely dispersoids also had reduced corrosion-induced elevation changes compared to the matrix.

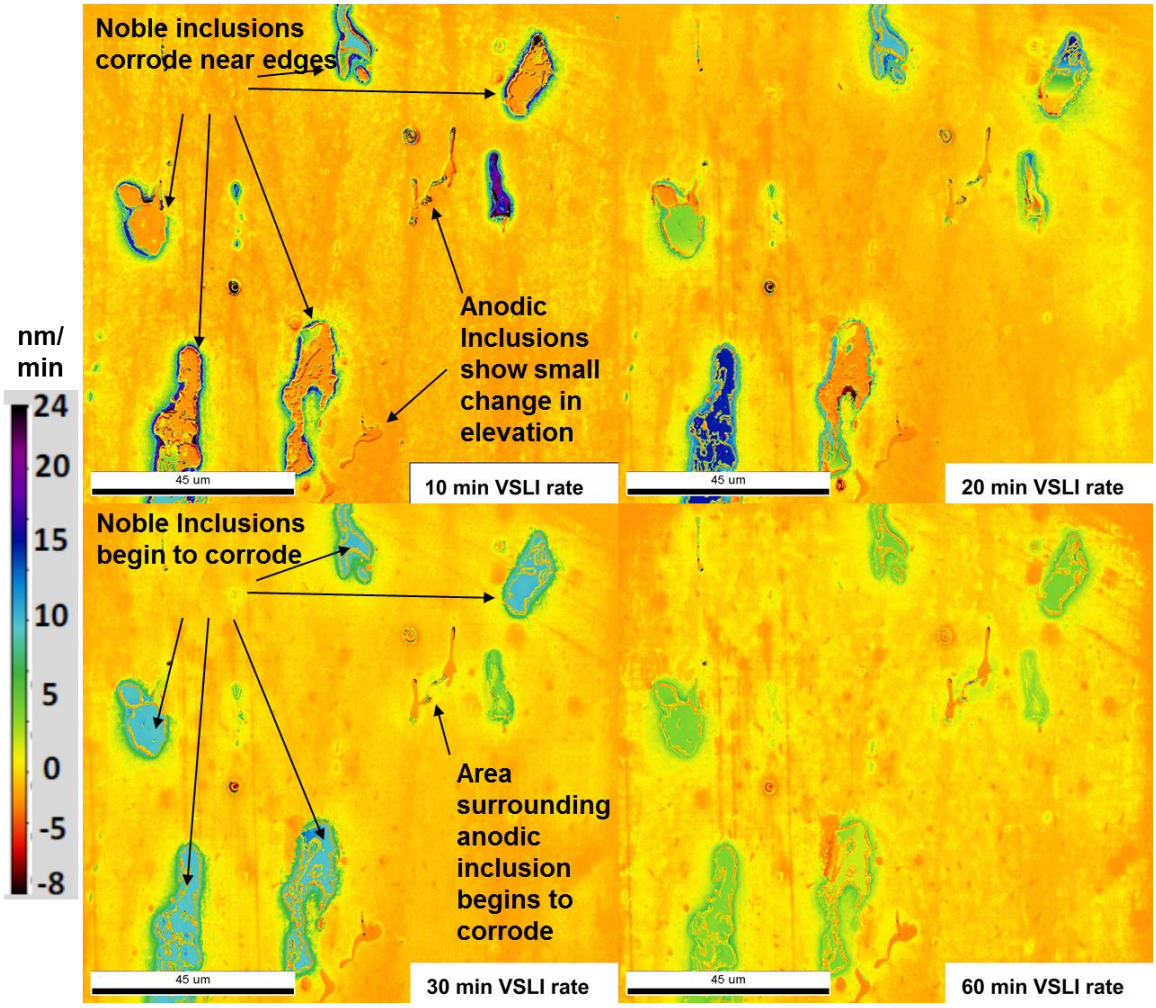

Figure 36: VSLI corrosion rates after 10 min., 20 min, 40 min, and 60 min of drop-wise exposure to 3.5 wt. % NaCl solution.

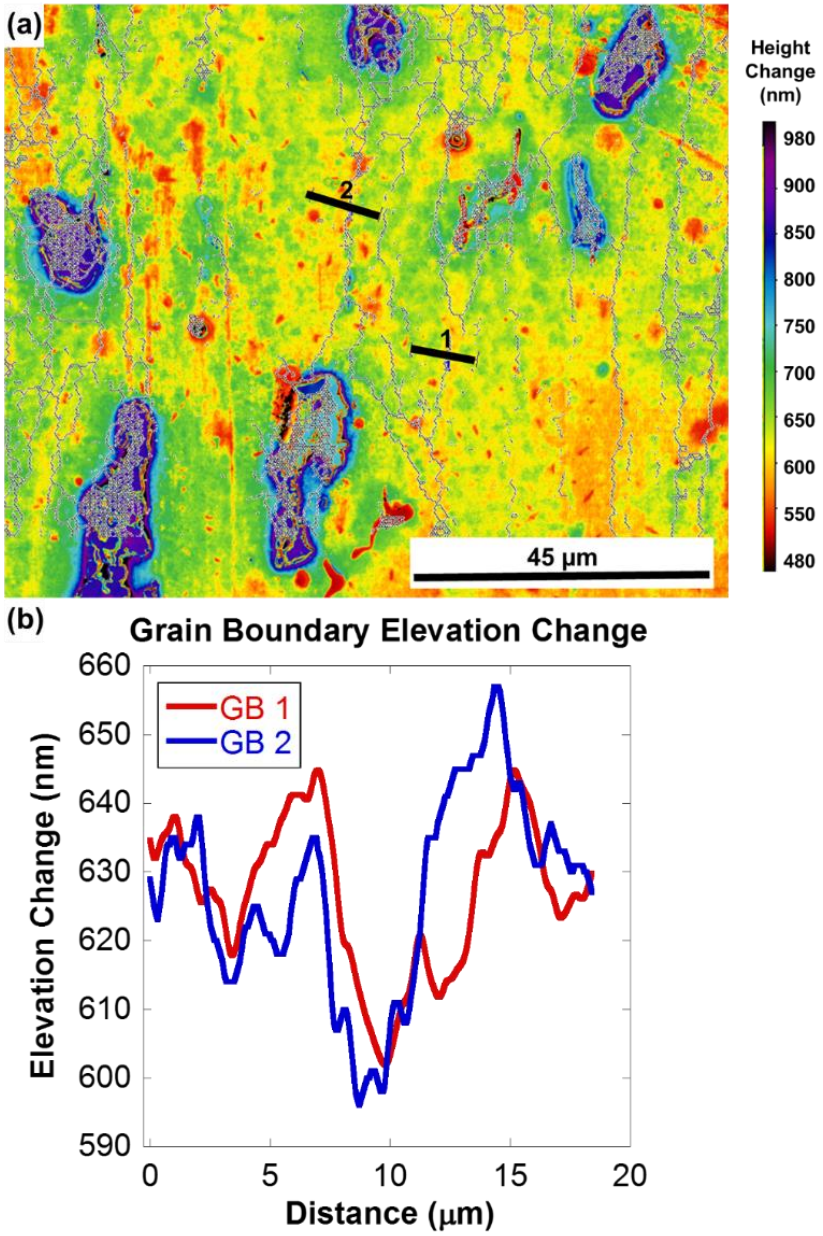

Figure 37: (a) High contrast view of elevation change from 0-60 minutes with grain boundaries from EBSD map overlaid in black shows that some of the grain boundaries have clearly different corrosion properties from the bulk. (b) profile plots of grain boundaries show they had less elevation change than the bulk grain boundaries after 60 min solution exposure.

To understand the corrosion phenomena in greater detail, one noble inclusion and one anodic inclusion each were selected for detailed analysis using the VSLI data and FIB-SEM cross-sectioning. Figure 38 shows SEM images the noble inclusion chosen before and after 60 minutes of corrosion. Note that this inclusion had two discrete compositions, with different levels of nobility in the galvanic series. Additionally, after corrosion an edge region closely surrounding the inclusion had a different appearance than the surrounding matrix. Table 6 shows the compositions of the two phases of interest, indicating that the slightly darker region, labeled "2", had higher concentrations of Cu and Fe than the bright white region.

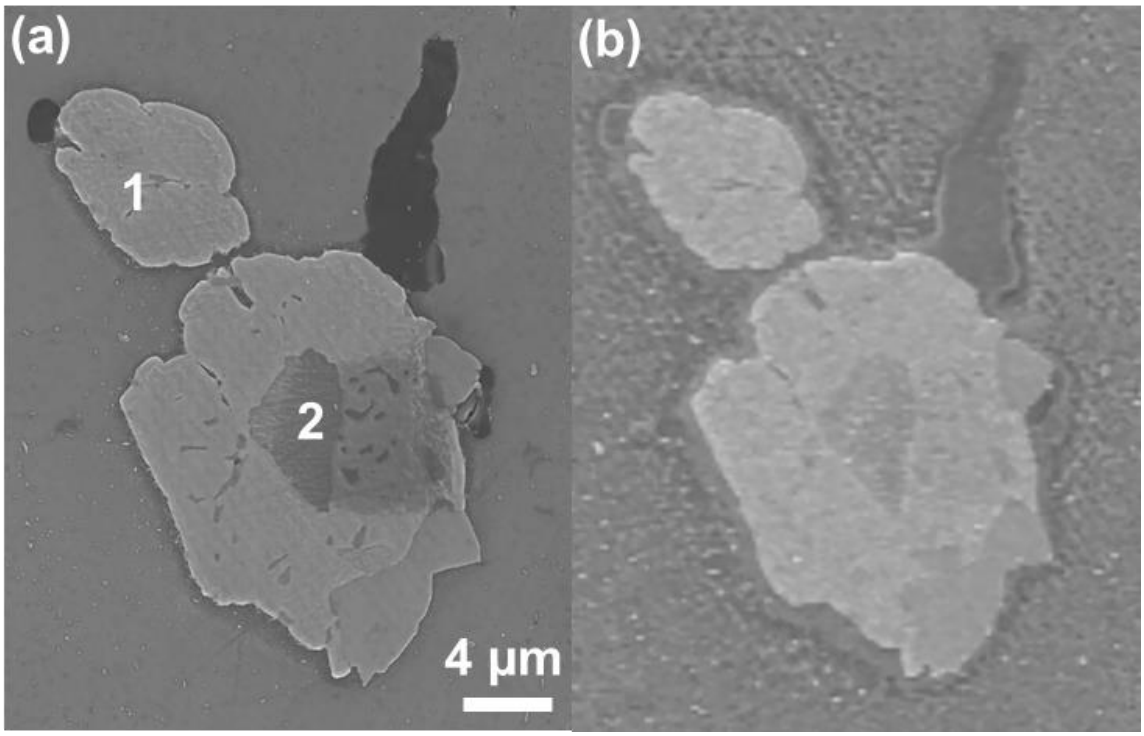

Figure 38: Fe-rich inclusion selected for analysis by FIB-SEM cross-section. Secondary electron SEM images (a) before corrosion and (b) after corrosion.

Table 6: Chemical compositions of the discrete phases within the Fe-bearing composite inclusion particles.

Element	**Al**	**Cu**	**Fe**	**Mg**	**Zn**
Region 1 (Atom %)	75%	16%	7%	1%	1%
Region 2 (Atom %)	69%	19%	11%	--	1%

Figure 39 shows 3D cross-sectional views of the relative height changes near the center of the inclusion (point 2 in Figure 38 (a)). Careful analysis of the views in Figure 39 shows that initially the inclusion is higher than the matrix due to preferential material of the softer matrix material during mechanical polishing, but as the corrosion proceeds past approximately 20 minutes of exposure, two regions within the noble inclusion increase in elevation with respect to their surroundings. These two regions are the matrix surrounding the inclusion at a short distance from the inclusion, and some small regions within the inclusion.

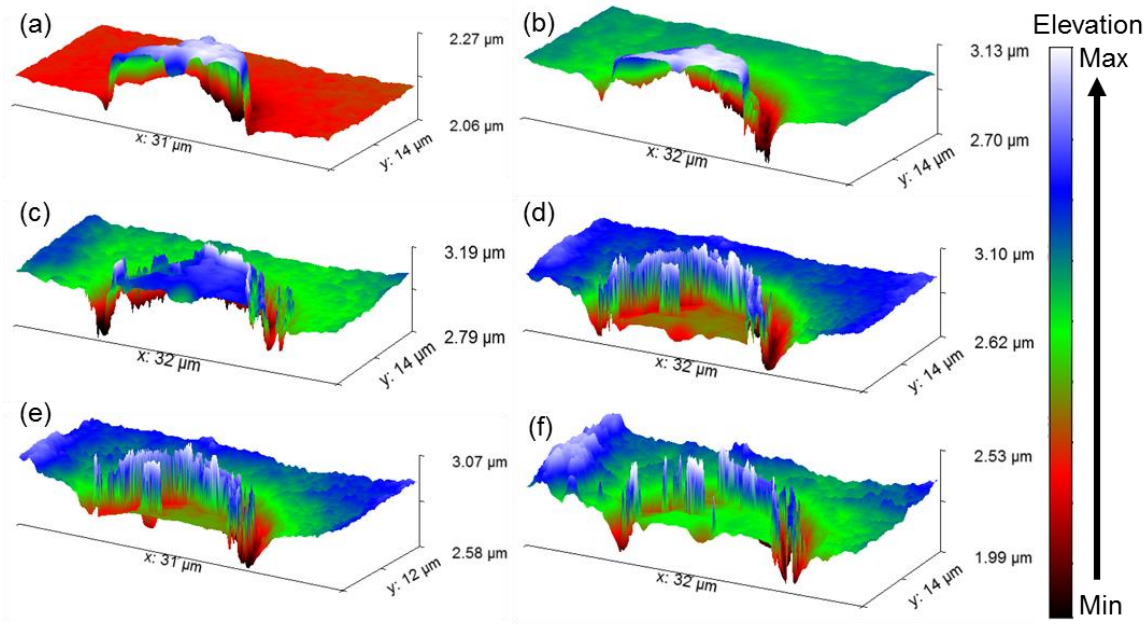

Figure 39: Detailed 3D surface height profile showing the localized height differences of a cross-sectioned Fe-rich inclusion (a) before corrosion, after (b) 10 min, (c) 20 min, (d) 30 min, (e) 40 min, and (f) 60 min dropwise exposure to 3.5 wt.% NaCl solution.

To further probe into the exact corrosion damage mechanisms causing the local changes in surface profile, FIB-SEM cross-sectional imaging was performed near the same region shown in Figure 36. From the cross-section of the noble inclusion in Figure 40, one can see that the areas which showed the greatest increase in elevation had the most corrosion. Furthermore, two regions of relatively low corrosion were observed: the ~250 nm region directly adjacent to the inclusion, and the darker, more noble phase within the Fe-rich inclusion.

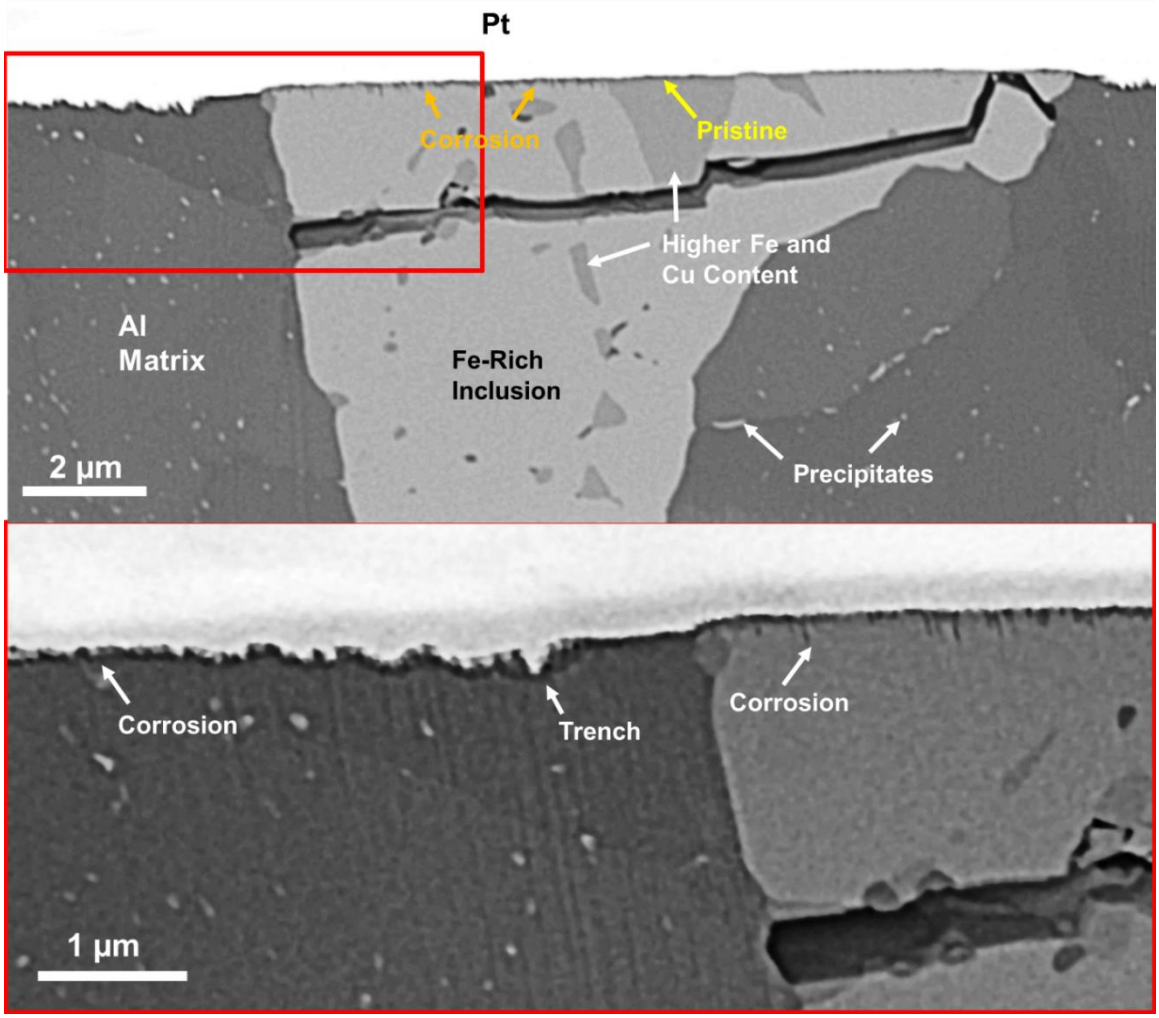

Figure 40: High-resolution BSE SEM images of cross-section from Fe-bearing inclusion after corrosion showing the localized region surrounding the inclusion with minimal corrosion damage, followed by a region with trenching, and then uniform corrosion.

A similar procedure was used to view an anodic Mg-rich inclusion. The inclusion selected is shown in Figure 41. Note this inclusion had cracks and pores in addition to the dark Mg-rich regions. Figure 42 shows the 3D rendering of the anodic inclusion's cross-sectional height during the progression of corrosion. Note that this inclusion was already

at a lower elevation than the surrounding matrix due to preferential material removal of the Mg inclusion during polishing, since the Mg_2Si inclusion is anodic compared to the surrounding matrix. Observation of height changes in the Mg_2Si and surrounding matrix as corrosion proceeded suggested that corrosion surrounding the inclusion was delayed for approximately the first 20 minutes, which may indicate the amount of time required for the Mg within the Mg_2Si inclusion to act as a sacrificial anode to reduce corrosion in the surrounding matrix. Comparison between the corrosion rate images in Figure 36 and the relative corrosion heights in Figure 42 suggests that from 20-60 minutes, the corrosion rates and relative height changes of the matrix immediately surrounding the inclusion became more pronounced than the surrounding matrix at a distance. This indicates that once the

This change in corrosion rate is due to a mechanism change in the corrosion once the Mg_2Si inclusion is sufficiently depleted of Mg. For the first 20 minutes, the Mg in the Mg_2Si was depleted by dissolution, after which point only Si was remaining. The Si was more noble than the surrounding aluminum matrix, therefore the area immediately surrounding the Si inclusion began to corrode at an accelerated rate with respect to the rest of the matrix. Examination of the FIB cross section in Figure 43 suggests that the shape of the Mg_2Si inclusion remained relatively unchanged, but that does not rule out the possibility that the Mg was preferentially dissolved, as recent studies have indicated. More interesting to note is the jagged shape of the corrosion damage in the matrix immediately surrounding the inclusion. Since the VSLI and SEM images before corrosion did not show such jagged features, the possibility of scratches from polishing

can be ruled out. These jagged features could be representative of corrosion damage initiating at defects in the passive layer or precipitates near the surface.

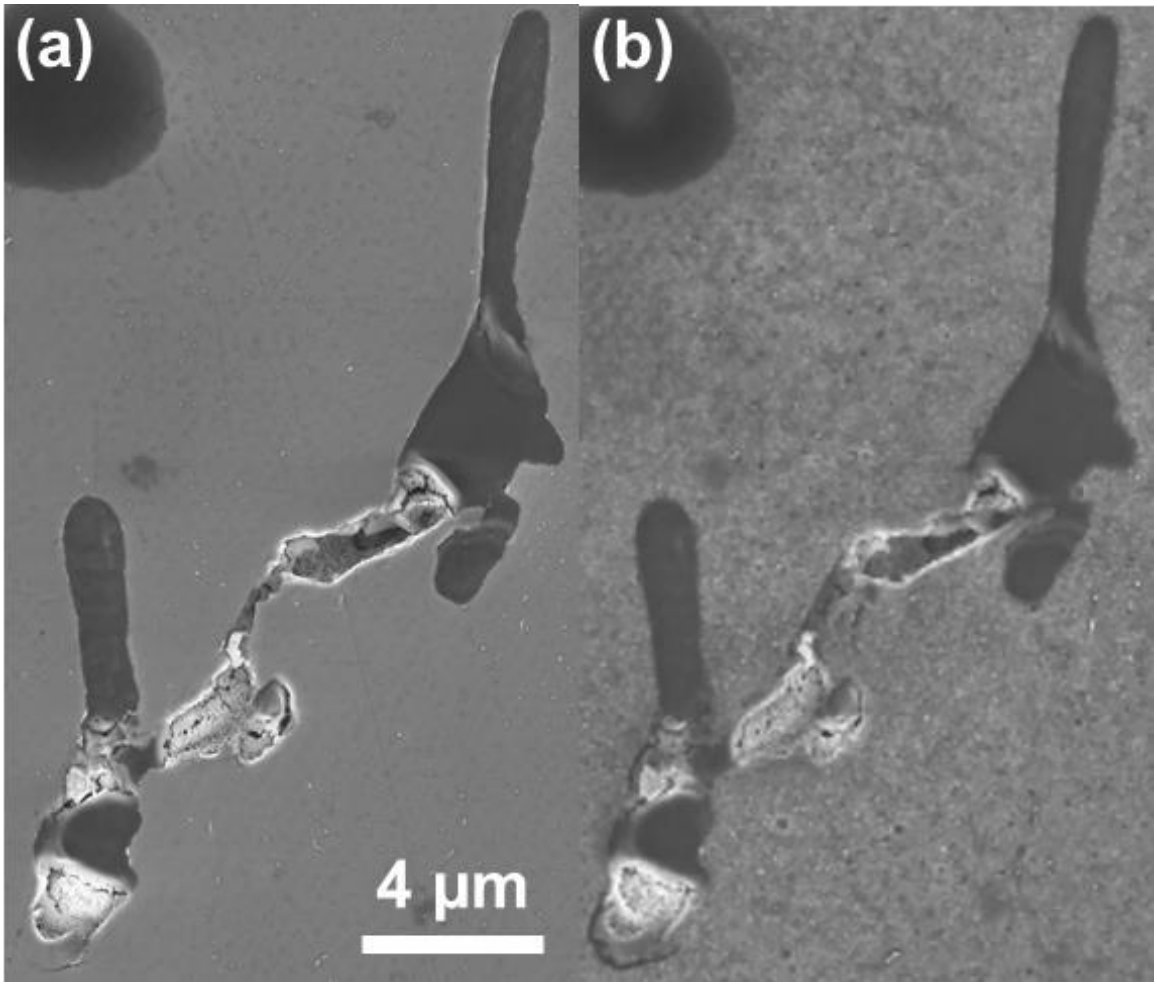

Figure 41: InLens SEM images of Mg-bearing inclusion (a) before and (b) after corrosion.

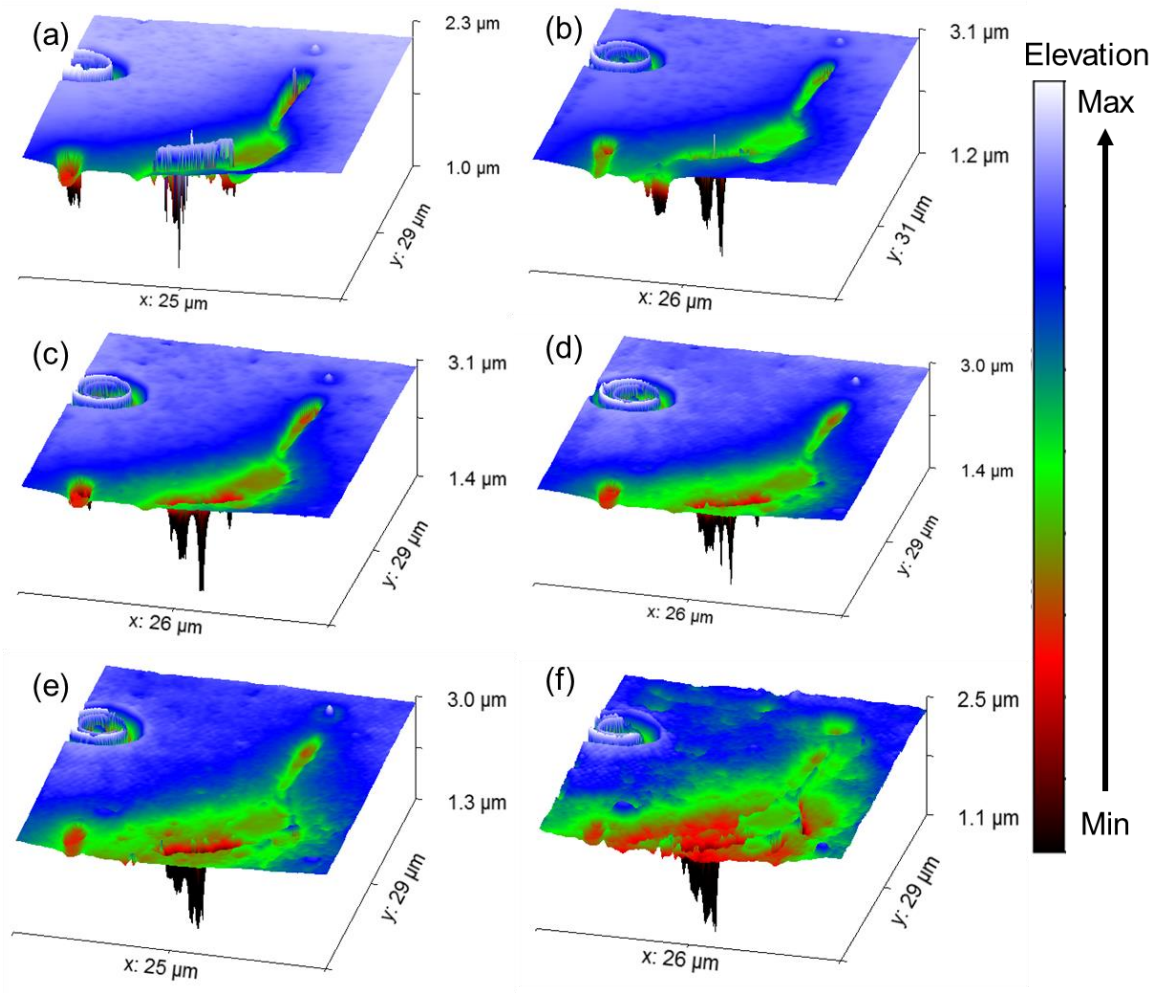

Figure 42: Detailed 3D surface height profile cross-sections of Mg-rich inclusion from (a) before corrosion, after (b) 10 min, (c) 20 min, (d) 30 min, (e) 40 min, and (f) 60 min dropwise exposure to 3.5 wt.% NaCl solution.

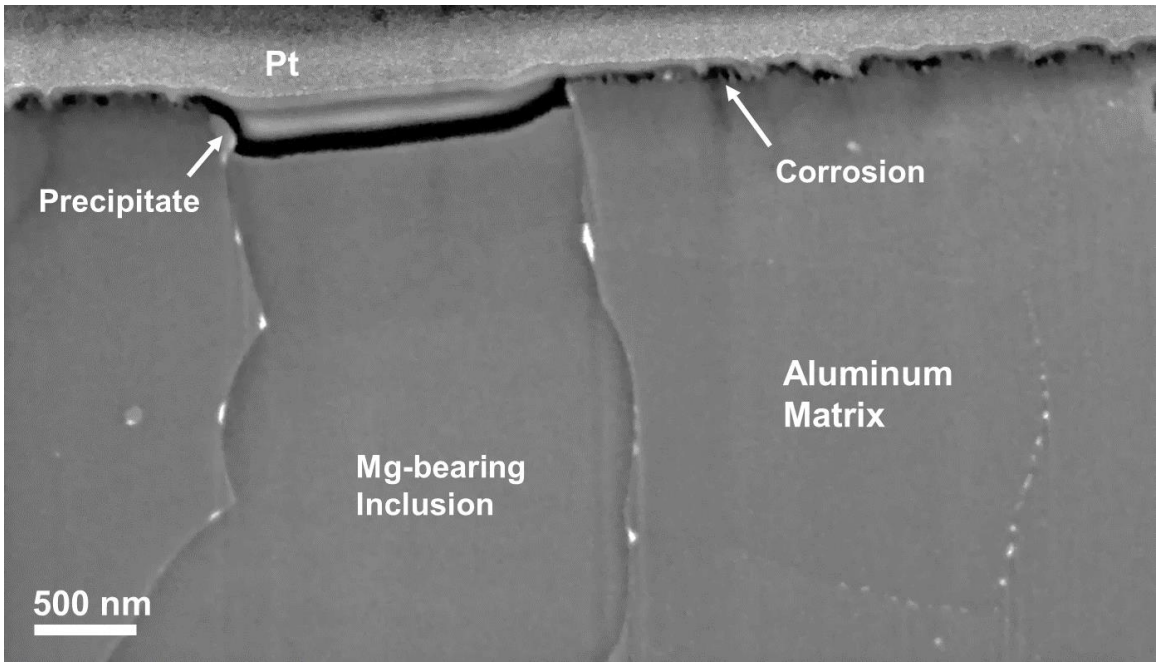

Figure 43: FIB cross-section of Mg-bearing inclusion shows relatively uniform corrosion depth away from the sample, with some localized jagged features which may have been created by precipitate fallout during corrosion.

6.4 Discussion

This study has shown that inclusions, dispersoids, and grain boundaries all play unique roles in the corrosion properties of 7075-T651 alloy. The inclusions are the largest particles in the alloy with significantly different compositions from the matrix. Hence, the inclusions had the largest effect on the corrosion height changes. The Fe-bearing inclusions had discreet phases with varying concentrations of noble elements such as Fe and Cu. These differences in concentration altered the corrosion properties and led the sections of the inclusions with higher Al concentration to corrode rapidly. Additionally, for all the Fe-bearing inclusions, there was a region extending about 200 nm from the inclusion into the matrix which demonstrated slower corrosion than the surrounding

matrix. This region may be more resistant to corrosion due to diffusion of copper from the inclusion during solidification, and causing the high copper region to be noble compared to the matrix. Further studies using EDS in a transmission electron microscopy or electron energy loss spectroscopy would clarify the composition of this near-inclusion region and its effects on the corrosion behavior. From the 200 nm region, the trench surrounding the inclusion grew. Since prolonged corrosion is known to cause Fe-rich inclusions to fall out [37,43,119], the corrosion may propagate by a time-dependent periodic model in which sections of the inclusion corrode, then the matrix corrodes, until correct chemical balance is reached, upon which the Cu-rich region surrounding the inclusion corrodes and the inclusion falls out.

Mg_2Si corrosions are known to corrode by a dissolution mechanism [60,167,193]. Investigations of corrosion in Al-Mg-Si alloys has suggested that initial stages of corrosion for the first 20 minutes are controlled by dissolution of Mg, after which point the Si remnant becomes cathodic with respect to the matrix [53]. Similarly, inspection of Figure 42 suggests that the Mg dissolution was a factor in the corrosion for approximately the first 20 minutes of corrosion when the surrounding matrix began to elevate at an accelerated rate with increasing time due to the change in inclusion electrochemistry from anodic Mg-rich to cathodic Si-rich. Additionally, comparison of the corrosion damage from Figure 40 and Figure 43 suggests that the corrosion surrounding the Mg particle was more discreet and may have relied on dissolution of the precipitate particles judging by its jagged shape, while corrosion surrounding the Fe-

bearing particles appeared to involve dissolution of the matrix due to its smooth trench shape.

An effect of grain boundaries on the corrosion elevation change was also observed for this sample. Comparison of an EBSD grain boundary map and the VSLI map clearly exhibited a reduced change in elevation for the grain boundaries compared to surrounding grain bulk. Considering the grain boundary precipitates in 7075-T651 alloy have been reported to have chemistry $Mg(Cu_xZn_{1-x})_2$ with average contents of Mg, Cu, and Zn of 45.2, 15.1, and 39.7 at.% [31]. Additionally, the grain boundary precipitates in 7075-T651 have been reported as large as 3 μm [194] because the stretching of the alloy before precipitate growth heat treatments leads to larger grain boundary precipitates [26,195]. The reduced height dependence on corrosion of the grain boundaries was not clearly observable until after 60 minutes of exposure. Therefore, the corrosion mechanism of the grain boundaries may also involve initial dissolution of the Mg from the precipitates, followed by protection of the grain boundaries via the remaining Zn and Cu.

In this small sample volume, a dependence of grain orientation on the corrosion rate was not explicitly quantifiable. While there may be some influence of grain orientation on corrosion rates, it is subtle and not easily quantifiable for this small region of interest. Additionally, some authors have attempted to find the dependence of corrosion on orientation Al-Cu alloy single crystals and found that with increasing alloy concentration, a decreasing dependence of grain orientations on pit formation [68].

6.5 Summary

In this study, pre-corrosion SEM imaging, EBSD, and EDS were coupled with interrupted corrosion and VSLI scanning, as well as post-mortem FIB-SEM cross-sectioning to view the height changes due to corrosion of multiple microstructural features. Several useful observations were found:

1. Corrosion initiation was observed to occur at a ~200 nm distance from Fe-bearing inclusions.
2. Corrosion was observed within Fe-bearing inclusions, which may have been due to the presence of discreet phases with different electrochemical potentials.
3. The local corrosion rates surrounding Mg-bearing inclusions were minitially effected, but an increased corrosion rate surrounding the Mg_2Si inclusion was observed after ~20 minutes of corrosion corresponding to Mg depletion from the inclusion.
4. After ~60 minutes of corrosion, reduced elevation changes were observed at the grain boundaries. This may have corresponded to Mg depletion from the $Mg(Cu_xZn_{1-x})_2$ precipitates at the grain boundaries.

7 THREE DIMENSIONAL TIME-RESOLVED QUANTIFICATION OF INCLUSION AND GRAIN BOUNDARY EFFECTS ON CORROSION PIT EVOLUTION IN AN AEROSPACE ALUMINUM ALLOY

7.1 Introduction

The cause of stochastic pit growth may be inhomogeneity of the passive layer caused by defects such as precipitates at grain boundaries and inclusions. For instance, recent studies of corrosion in high purity aluminum and natural-aged aluminum alloy of varying grain sizes has suggested that corrosion rate decreases with decreasing grain size[57,66], which may be due to larger, more heterogeneous particles form at the grain boundaries. Nonetheless, when the alloys are heat-treated, the precipitates can grow and subsequently alter the pit growth-precipitate relationships. Therefore, the peak-aged and over-aged alloys can exhibit different exacerbated corrosion near grain boundaries[35,48,64,65,67]. Until now experimental limitations have prevented thorough, quantitative studies of the grain boundary relationships with corrosion pitting progression in aluminum alloys.

The advent of high resolution laboratory scale X-ray tomography and diffraction contrast tomography techniques have enabled new insights into corrosion pitting mechanisms by combining nondestructive 3D crystallographic and phase information at the microscale. GrainMapper v1, which computes grain centroids and approximate 3D volume nondestructively using laboratory-scale X-ray diffraction patterns, have already enabled significant advancements in multimodal time-lapse three-dimensional materials

research [196–199]. Moreover, synchrotron diffraction-contrast tomography studies with grain boundary reconstruction have shown tremendous advancements in understanding of stress corrosion cracking and fatigue experiments which were designed to fit within the short time constraints of synchrotron X-ray beam time allocations [147,200–203]. Thanks to the advent of grain boundary reconstruction in laboratory X-ray machines, materials damage phenomena of slower, more relevant time scales can now be observed in 3D over time. These advancements in laboratory scale diffraction contrast tomography enabled our 3D study of the effects of phases and grain boundaries on corrosion pitting in aluminum alloys for the first time. This work represents the first commercial application of grain shape reconstruction created using Xnovo GrainMapper v2.0α[204].

7.2 Materials and Methods

7.2.1 Sample Preparation

The sample was EDM machined along the short orientation of a 7475-T6 Plate (Alcoa, USA), then the gauge section was ground to a 1 mm diameter with a 2 mm fillet radius. The sample was then heat treated at 510 ^{o}C for 24 h to grow the grains so that they could be clearly resolved using the labDCT technique, since the minimum grain size is approximately 20 – 40 μm, depending on the probability for diffraction of a given crystal type and the size of the sample causing too many diffraction spots and overlap, which would inhibit the reconstruction algorithm from working accurately. The sample was gently polished using 1200 grit sandpaper and 1 μm diamond paste with methanol lubricant, then briefly rinsed and dried.

7.2.2 Tomography Scanning

The sample was scanned in a Zeiss Xradia Versa 520 using a maximum X-ray energy of 160 kV and a 750 µm X-ray aperture, with 20 mm distance between the sample and source, and 20 mm distance between the sample and the detector. This Laue focusing X-ray geometry maximizes the focusing of the diffraction spots on the detector. The diffraction patterns were reconstructed in 3D using Xnovo Grainmapper v2.0 to achieve a grain boundary positional resolution of approximately 10 µm. Absorption contrast tomography scans were performed using the same geometry to ensure accurate registration with the DCT data. A maximum energy of 50 kV was used for the absorption scans to ensure high contrast between inclusions and the aluminum matrix. The pixel edge length of the absorption tomography data was 1.68 µm. After initial scanning, the sample was placed in a 110 mL bath of 3.5 wt.% (0.6 M) NaCl solution mixed with DI water. The sample was removed, absorption tomography scanned, and replaced to the bath after 14, 60 and 90 days of corrosion. The post-corrosion data sets were registered with the pre-corrosion DCT data using an automated point-matching algorithm in MATLAB to insure accurate comparison during the data analysis. Inclusions were segmented via thresholding using Avizo Fire. The matrix at each time point was segmented by thresholding. Pits were automatically segmented in MATLAB by automatically fitting an ellipse to each slice of the matrix using a convex hull technique, then fitting polygons to the region between the matrix and the ellipse. A MATLAB code was written to identify the boundaries between the grains using the reconstructed DCT data, and perform quantitative analysis.

7.3 Results

7.3.1 Corrosion Pit Growth Relationships

Grain boundaries have been found to play a role in corrosion, but the extent of the significance of grain boundaries in corrosion pit growth versus inclusions is not well known. Therefore, knowledge of both grain boundary and inclusion positions within the alloys is critical to understanding the corrosion mechanisms during the time-lapse study. Figure 44(a) shows a 3D of the inverse pole figure (IPF) color format display of the grains within the sample. Many of the grains still have an oblong shape due to the rolling of the aluminum plate during initial hot rolling from the melt, even though the alloy was heat-treated for grain growth for 24 h at 510 ^{o}C after rolling. Figure 44(b) shows a greyscale 3D rendering of the sample surface after 14 days of corrosion, displayed in the same orientation as Figure 44(a). The bright white regions are inclusions, the dark gray regions are corrosion products, and the light gray regions are relatively uncorroded matrix. Figure 1(c) highlights the corrosion pits from the 14 days of corrosion in red which were identified using an automated algorithm. Figures 1(d-g) show the progression of the corrosion and pit growth for 60 and 90 days. From these images, two distinct pit morphologies can clearly be observed, one is a rounded pit shape, and the other is a line shaped pit which may be due to intergranular corrosion. Additionally, note that not all of the inclusions on the sample surface led to corrosion pits, even though it is well known that inclusions are a significant motivator for corrosion pits [35,37,43,47,48,52–57]. This may be due to the need for other factors to motivate pit growth, such as grain boundaries

and triple points. Indeed, careful examination of Figure 44 suggests that regions of the sample with a higher density of grain boundaries have a higher density of pits. Studies of pitting and intergranular stress corrosion cracking have shown that the short and transverse directions are more susceptible to corrosion and cracking than the rolling direction due to the smaller grain size and higher density of grain boundaries relative to the rolling direction[205,206].

Figure 45 compares the grain orientations of a 2D section through the height of the sample with the phase information before and after corrosion. From these images, one can clearly see the corrosion pit forms at the intersection of three grains and an inclusion. This is due to a combination of the multiple phases within the area including enlarged precipitates, Fe-bearing inclusions, and the aluminum alloy. Since the grain boundary represents a high entropy region full of defects in the crystal lattice, and there are also particles of different corrosion potentials, these areas have the highest probability for corrosion in peak-aged and over-aged alloys[35,48,64,65]. An additional mechanism of corrosion pitting was found in Figure *46*. In this case, the corrosion pit formed within a grain without an inclusion due to the formation of a crack in the corrosion product layer early on, which may have led to the formation of a local crevice followed by subsequent reduction of pH and preferential corrosion in the region.

Using this nondestructive time-lapse 3D LabDCT technique, a large sample of microstructure can be surveyed and features from different imaging techniques can be overlayed to elucidate corrosion mechanisms more clearly. Figure 47 shows an inside-out perspective 3D rendering of the near-surface inclusions and grain boundaries overlaid

with the corrosion product and corrosion pits across all three timepoints of corrosion. Note that in Figure 47, many of the corrosion pits interact with grain boundaries, triple points and inclusions. Additionally, the number of corrosion pits and size of pits increased with increasing immersion time. Furthermore, comparison of selected pits and the grain boundaries suggests that the corrosion occurred as a mixture of pit formation and intergranular corrosion as the corrosion time proceeded from 60 to 90 days.

Using this data, excellent statistical representations can be found to provide more certainty of the alloy damage mechanisms. Table 7 shows the fraction of inclusions which covered the corroded surface areas after 14, 60, and 90 days corrosion. Comparison with the fractions of pits touching inclusions and grain boundaries or triple points shows that even though inclusions and grain boundaries represent relatively small fractions of the sample surface, they have a disproportionally large effect on motivating the growth of corrosion pits.

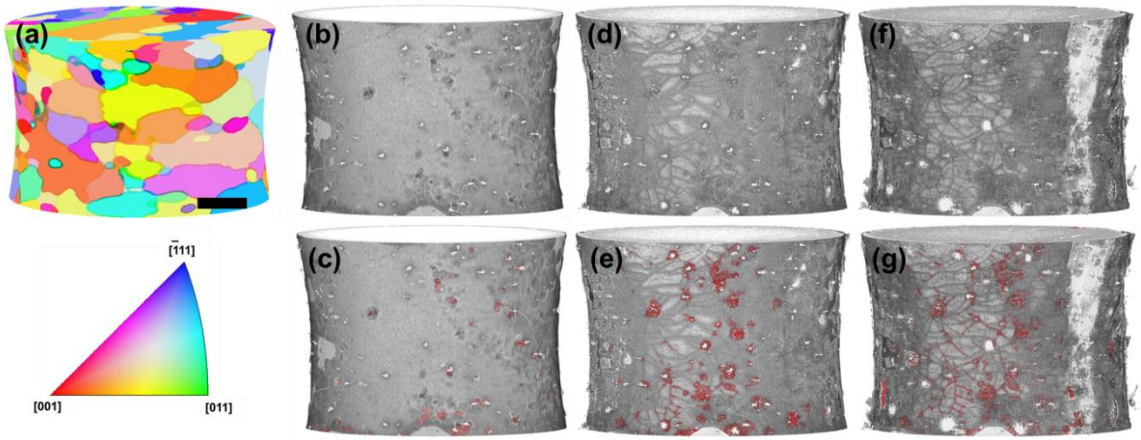

Figure 44: (a) 3D rendering of the grains within the sample with the colors displayed in inverse pole figure format, along with the corresponding inverse pole figure triangle. (b) 3D rendering of the sample after 14 days of corrosion (c) 14 days corrosion with pits overlaid in red. (c) 3D rendering of the sample after 60 days of corrosion and (c) 60 days corrosion with pits overlaid in red. (b) 3D rendering of the sample after 90 days of corrosion (c) 90 days corrosion with pits overlaid in red. Note that deep "mud-cracking," led to preferential corrosion of the matrix. The scale bar width is 200 μm.

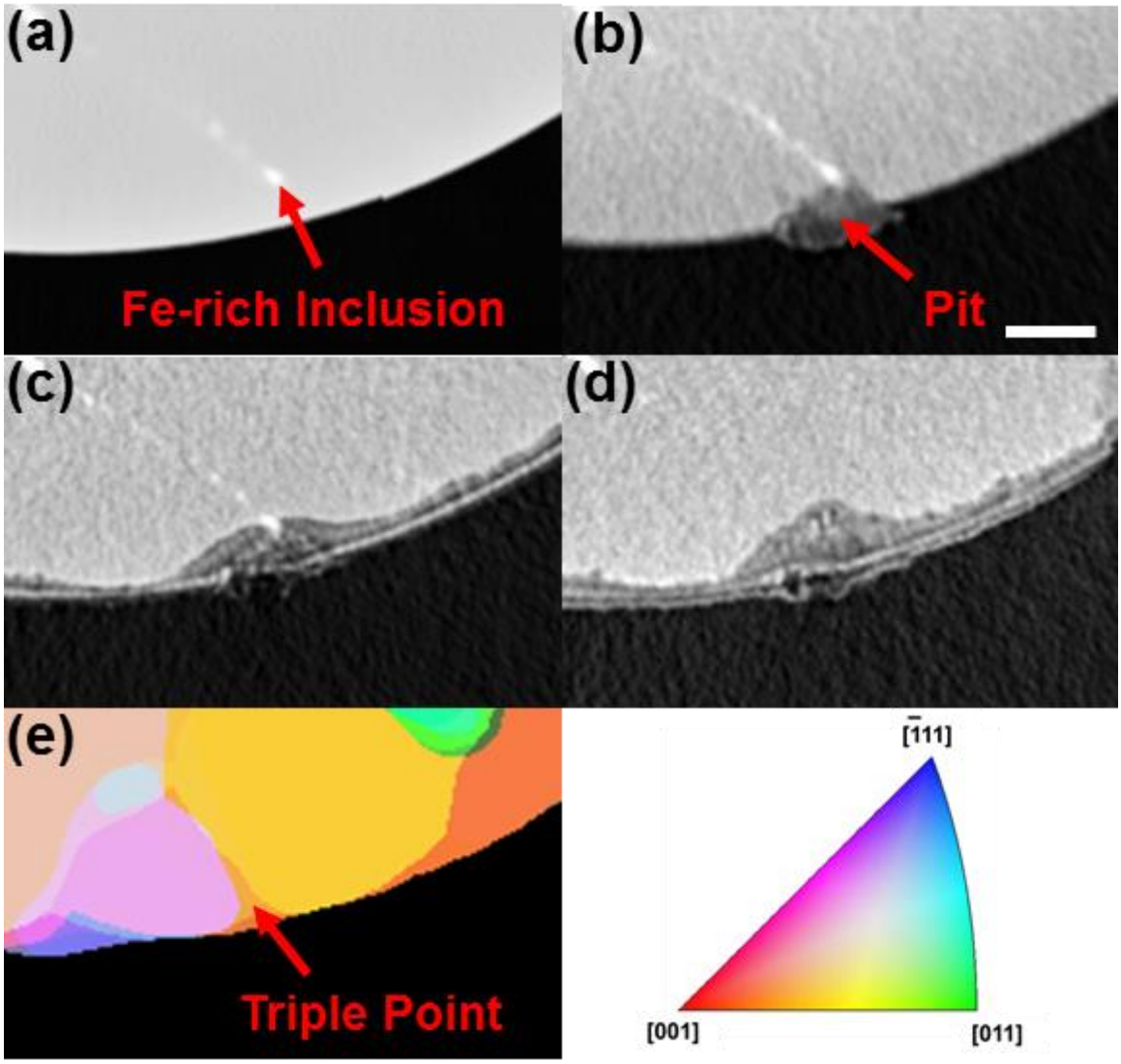

Figure 45: (a) 2D slice of absorption contrast data before corrosion showing inclusion near surface. (b) After 14 days of corrosion, a pit could be seen surrounding the inclusion. (c) After 60 days, the pit depth and width increased. (d) After 90 days, the pit depth continued to increase. (d) DCT slice showing this pit occurred at a grain boundary triple point. The scale bar width is 50 μm.

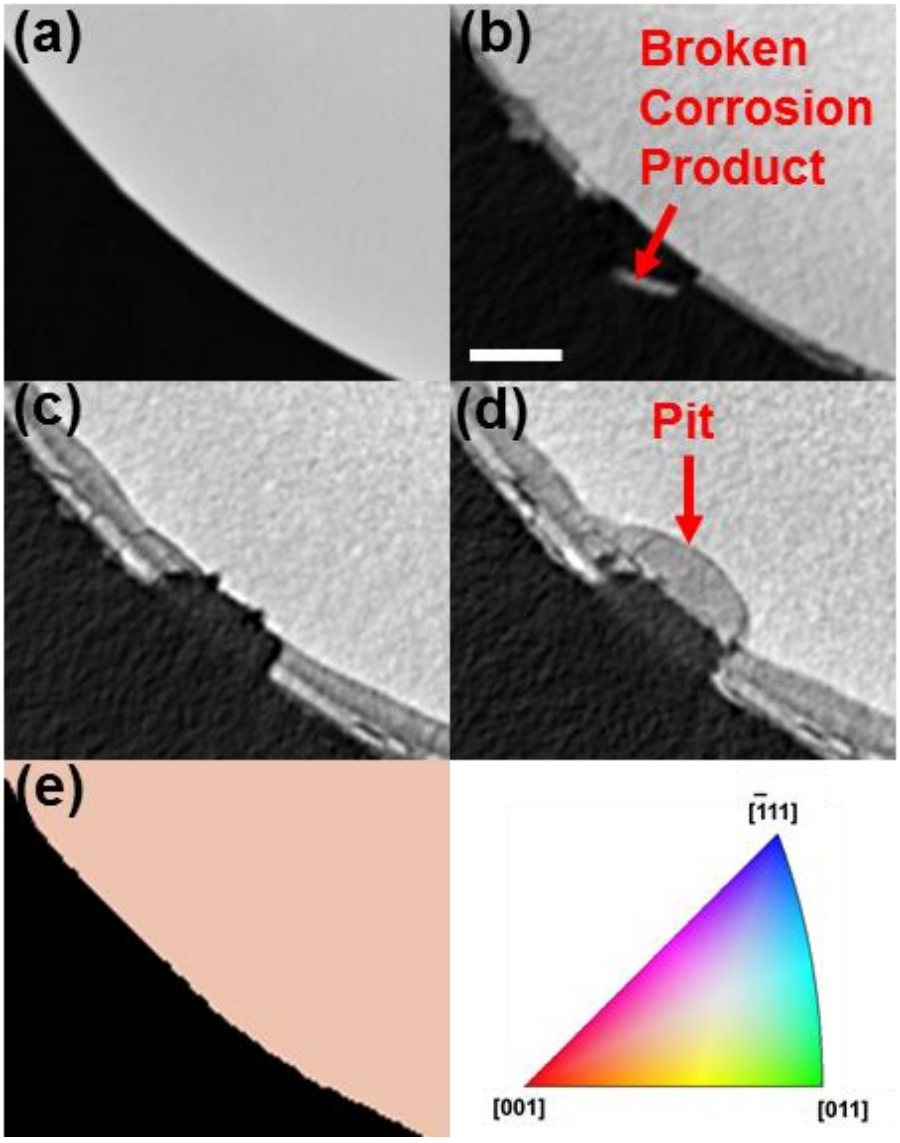

Figure 46: (a) 2D slice of absorption contrast data before corrosion. (b) After 14 days of corrosion, a portion of the corrosion product cracked away. (c) After 60 days, the corrosion product surrounding the cracked area grew to form a crevice. (d) After 90 days, a pit formed in the crevice left behind at the cracked region. (d) DCT slice showing this pit occurred within the bulk of a grain. The scale bar width is 50 μm.

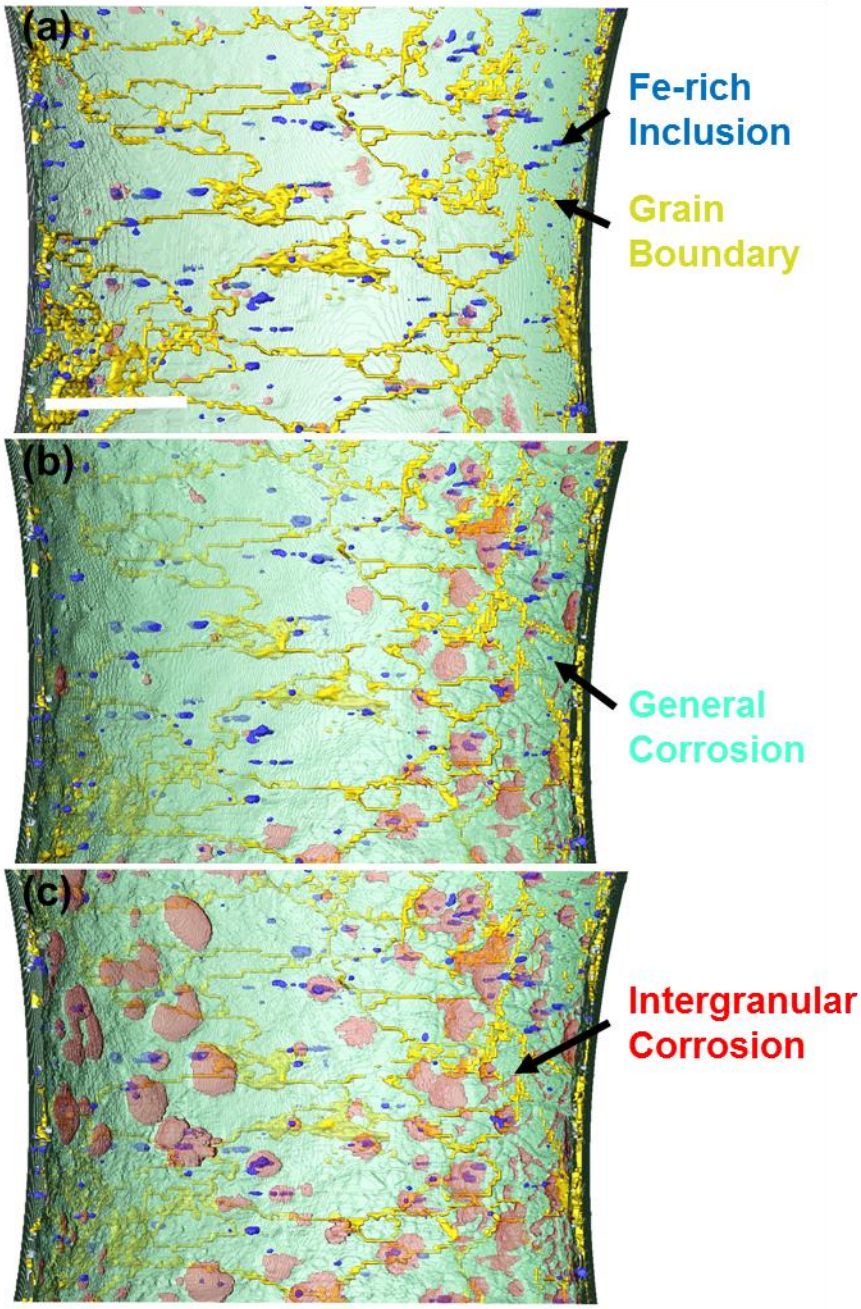

Figure 47: Inside-out view of near-surface grain boundaries, inclusions, corrosion products, and corrosion pits. (a) 14 days corrosion damage, (b) 60 days corrosion damage, (c) 90 days corrosion damage. The scale bar width is 200 μm.

Table 7: Proportions of inclusions and grain boundaries touching the corroded surfaces after 14, 60, and 90 days corrosion compared to the number of pits touching grain boundaries or triple points and inclusions.

Exposure Time (Days)	**14**	**60**	**90**
Inclusions Touching Corroded Surface (%)	1.20%	0.70%	0.60%
Boundaries Touching Corroded Surface (%)	13.00%	12.00%	11.70%
Inclusions Intersecting Grain Boundaries and Surface (%)	0.17%	0.08%	0.08%
Pits Touching Inclusions (%)	14.90%	33.70%	35.50%
Pits Touching Grain Boundaries (%)	54.10%	59.40%	69.90%
Pits Touching Grain Boundaries and Inclusions (%)	4.10%	13.10%	10.80%

The pit depth histogram in Figure 48 shows that the pits depth increased over time. The skewness values were computed for the three time points to understand the change in the distribution of pit depths. Values of 0.61, 1.35, and 1.82 were calculated for 14, 60, and 90 days immersion, respectively. Therefore, the corrosion pit depths became increasingly skewed towards deeper depths with increasing time. distribution across increasing corrosion time with a slight skew toward higher corrosion values. Additionally, kurtosis values of 2.75, 4.99, and 6.97 for 14, 60, and 90 days, meaning that the potential for large, deep outlier pits increased with increasing exposure time for the

peak-aged alloy. With other heat-treating conditions such as over-aged 7XXX series alloy, the pit depth distributions may have even higher kurtosis of the pit depth, with larger and less frequent pits[70].

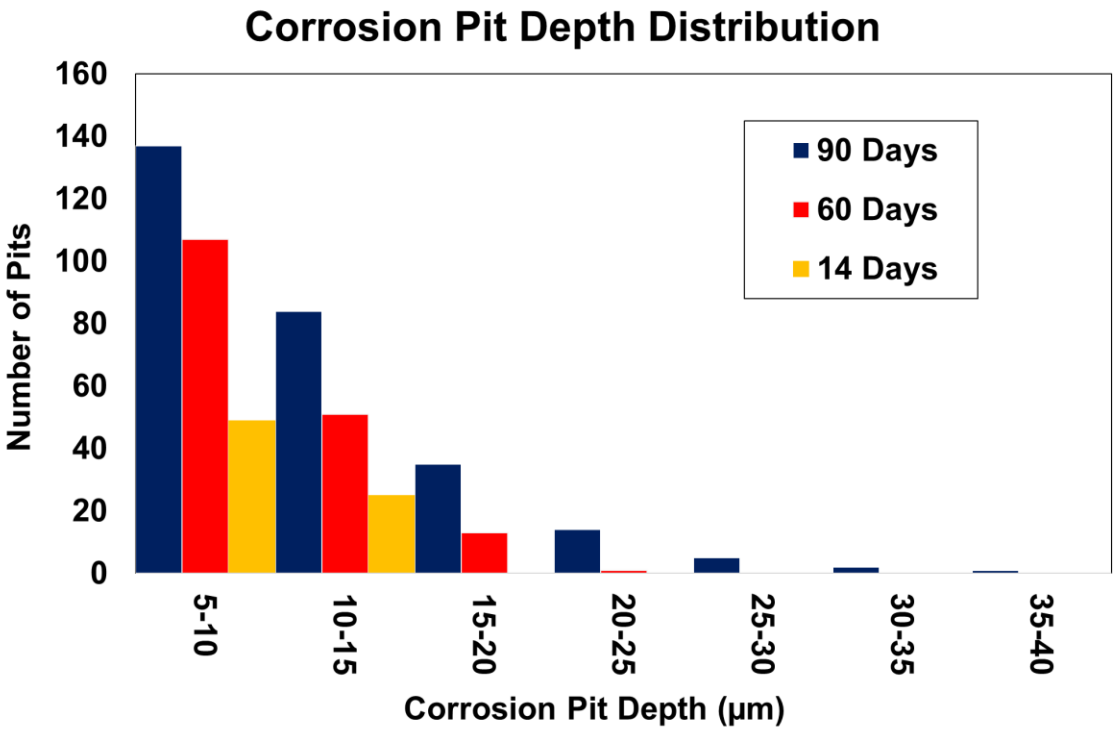

Figure 48: Distribution of corrosion pit depths after 14, 60, and 90 days of corrosion.

7.4 Summary

Based on the information gathered from this large quantity of 3D data, the sites with the lowest activation energy for corrosion in 7XXX alloy are grain boundaries intersecting with inclusions, followed by inclusions, and then grain boundaries. This is evident when examining the proportion of grain boundaries, inclusions, and inclusions intersecting with grain boundaries on the sample surface at any given point during the

corrosion process. The pits showed increasing dependence on inclusions, with the pits being 12x more likely to initiate at inclusions than the rest of the sample surface after 14 days, and 61x more likely after 90 days. The pits were ~4-6x more likely to initiate at grain boundaries than the rest of the surface over the course of corrosion. The confluence of grain boundaries and inclusions showed the greatest propensity for corrosion, with 24x likelihood for corrosion pit formation after 14 days of exposure, and ~150x likelihood for 60 and 90 days corrosion. Clearly, grain boundaries points and inclusions together have a significant impact on the rate of corrosion in the aluminum alloys.

This trend can be explained based on the alloy solidification and formation mechanisms. During alloy solidification, the inclusions solidify first and serve as heterogeneous nucleation sites for precipitate nucleation and growth. Additionally, grain boundaries serve as high entropy sites, leading to lower activation energy for precipitate nucleation and growth during age-hardening treatments. The combination of inclusions and triple points would provide the greatest chances for precipitate nucleation and growth, as well as higher propensity for lattice defects at the surface such as edge and screw dislocations, which may also cause defects in the passive layer. Additionally, the chemistry and structure of the precipitates can change as the aging increases[176,207]. The chemical composition of the precipitates which nucleate early may also be different, causing larger differences in electrochemical potentials and a faster rate of corrosion. Nonetheless, this study solidifies our understanding of the relevant microstructural features for corrosion pit growth in aluminum alloys.

These experimental findings provide useful insights about how corrosion pitting occurs in aluminum alloys. Corrosion pitting occurred primarily at triple points and inclusions. These findings can be used to engineer more corrosion and cracking-resistant aerospace aluminum alloys by engineering the grain size and impurity particles. As corrosion progress proceeds, a decrease in the dependence of low activation energy sites for pitting is found.

8 CONCLUSIONS

8.1 Summary of Research Findings

1. The pit geometry and fatigue crack growth progress were examined in 3D for a pitted peak-aged 7075 aluminum sample. *In situ* synchrotron tomography showed directly that pre-existing cracks within the corrosion product serve as preferential fatigue crack initiation sites due to their high stress concentration and attachment to the underlying aluminum metal matrix. Comparison between time-resolved 3D data and *post mortem* FIB-SEM-EDS fractography suggested that a significant portion of the evolved bubbles may come from preferential dissolution of Mg from the Mg_2Si particles.
2. 7075 samples of different aging conditions were prepared by corrosion in 3.5 wt% NaCl solution for 15 days, then fatigue tested *in situ* using X-ray synchrotron tomography. The pit geometry and fatigue crack growth progress were examined and compared in 3D.

a. Highly overaged 7075 has much larger pits than peak-aged and overaged 7075 when corroded in uncovered 3.5 wt% NaCl solution.
b. A correspondence between rolling orientation and pit shape was observed. This lead to different stress concentrations at the center for pits on the longitudinal face, and stress concentrations at the side of the pits for the transverse face.
c. A change in fatigue crack failure mechanism from brittle failure with a sharp crack tip to microvoid formation ahead of a blunt crack tip was observed with increased aging of the samples.
d. The fatigue crack growth rates showed increasing scatter with increased aging.

3. Corrosion-fatigue of corrosion pitted 7475-T6 was analyzed within the fatigue cycles. The fatigue crack initiated from a pre-existing crack within the corrosion product, which also contained a pit underneath. The pit had a sharp tip, or "jut-in," which the crack initiated from. Additionally, the crack appeared to follow along the corrosion pits on the sample surface. The crack face also showed significant presence of river markings, indicating that this sample's fracture may have been more dependent upon crystallographic features such as grain shapes and orientations than the 7075 alloy, which had a much flatter crack face with many inclusions and secondary cracks clearly visible on the fracture surface. Analysis of the

bubble volume changes within the crack during a fatigue cycle near crack initiation and near failure suggested that the bubble positions and volumes change significantly during a fatigue cycle.

4. Pre-corrosion SEM imaging, EBSD, and EDS were coupled with interrupted corrosion and VSLI scanning, as well as post-mortem FIB-SEM cross-sectioning to view the height changes due to corrosion of multiple microstructural features. Several useful observations were found:
    a. Corrosion initiation was observed to occur at a ~200 nm distance from Fe-bearing inclusions.
    b. Corrosion was observed within Fe-bearing inclusions, which may have been due to the presence of discreet phases with different electrochemical potentials.
    c. The local elevation changes surrounding Mg-bearing inclusions were minimally effected, but an increased corrosion rate surrounding the Mg_2Si inclusion was observed after ~20 minutes of corrosion corresponding to Mg depletion from the inclusion.
    d. After ~60 minutes of corrosion, reduced elevation changes were observed at the grain boundaries. This may have corresponded to Mg depletion from the $Mg(Cu_xZn_{1-x})_2$ precipitates at the grain boundaries.
5.

8.2 Future Work

The extensive literature review performed for this work, combined with the work involved in gaining the experimental data discussed above, have led to a few ideas for future work:

1. Further analysis should quantify the bubble's relationships dependence on crack tip opening displacement, and also use focused-ion beam to measure the corrosion product depth at selected locations along the crack face to examine the relationships between localized crack face corrosion product volumes and bubble volumes. Such an analysis could lead to improved understandings of crack tip chemistry and its effect on local crack growth rates.
2. A focus on using advances in computer science and synchrotron X-ray tomography could allow real time 3D imaging of every aspect of corrosion fatigue damage, removing any uncertainty regarding bubble mechanisms. A future study, technology permitting, should examine the corrosion-fatigue crack growth properties in real time to view every detail of the damage evolution mechanisms.
3. The 7XXX alloy's microstructural features are extremely sensitive to processing conditions and minor alloy composition changes. Therefore, extreme care should be taken in sample preparation of the latest alloys to accurately view the damage evolution mechanisms. In this manner, one can determine exactly how the fine changes used to evolve the newer generations of 7XXX alloys, e.g., from 7075 to 7475 and 7085, lead to improved performance. Such information, combined with proper thermodynamic and damage modelling, could lead to significant performance improvements for future generations of aerospace alloys.

9 REFERENCES

[1] G.H. Koch, M.P.H. Brongers, N.G. Thompson, P. Virmani, J.H. Payer, Corrosion Costs and Preventative Strategies in the United States, 2002.

[2] S.J. Findlay, N.D. Harrison, Why aircraft fail, Mater. Today. 5 (2002) 18–25. doi:10.1016/S1369-7021(02)01138-0.

[3] L. Molent, Managing airframe fatigue from corrosion pits - A proposal, Eng. Fract. Mech. 137 (2015) 12–25. doi:10.1016/j.engfracmech.2014.09.001.

[4] S.A. Barter, L. Molent, Service fatigue cracking in an aircraft bulkhead exposed to a corrosive environment, Eng. Fail. Anal. 34 (2013) 181–188. doi:10.1016/j.engfailanal.2013.07.036.

[5] L. Molent, Fatigue crack growth from flaws in combat aircraft, Int. J. Fatigue. 32 (2010) 639–649. doi:10.1016/j.ijfatigue.2009.09.002.

[6] E.A. Starke, J.T. Staley, Application of Modern Aluminum Alloys to Aircraft, 32 (1996) 131–172.

[7] A.S. Heller, R.. Heller, A.M. Freudenthal, Random Fatigue Failure of a Multiple Load Path Redundant Structure AD0604125, 1944.

[8] J.Y. Buffière, E. Maire, P. Cloetens, G. Lormand, R. Fougères, Characterization of internal damage in a MMC_p using X-ray synchrotron phase contrast microtomography, Acta Mater. 47 (1999) 1613–1625. doi:10.1016/s1359-6454(99)00024-5.

[9] J.Y. Buffiere, E. Ferrie, H. Proudhon, W. Ludwig, Three-dimensional visualisation of fatigue cracks in metals using high resolution synchrotron X-ray micro-tomography, Mater. Sci. Technol. 22 (2006) 1019–1024.

doi:10.1179/174328406X114135.

[10] P. Hruby, S.S. Singh, J.J. Williams, X. Xiao, F. De Carlo, N. Chawla, Fatigue crack growth in SiC particle reinforced Al alloy matrix composites at high and low R-ratios by in situ X-ray synchrotron tomography, Int. J. Fatigue. 68 (2014) 136–143. doi:10.1016/j.ijfatigue.2014.05.010.

[11] A. Bonakdar, F. Wang, J.J. Williams, N. Chawla, Environmental Effects on Fatigue Crack Growth in 7075 Aluminum Alloy, Metall. Mater. Trans. A. 43 (2011) 2799–2809. doi:10.1007/s11661-011-0810-0.

[12] S.S. Singh, C. Schwartzstein, J.J. Williams, X. Xiao, F. De Carlo, N. Chawla, 3D microstructural characterization and mechanical properties of constituent particles in Al 7075 alloys using X-ray synchrotron tomography and nanoindentation, J. Alloys Compd. 602 (2014) 163–174. doi:10.1016/j.jallcom.2014.03.010.

[13] T.J. Marrow, J.Y. Buffiere, P.J. Withers, G. Johnson, D. Engelberg, High resolution X-ray tomography of short fatigue crack nucleation in austempered ductile cast iron, Int. J. Fatigue. 26 (2004) 717–725. doi:10.1016/j.ijfatigue.2003.11.001.

[14] P.J. Withers, M. Preuss, Fatigue and Damage in Structural Materials Studied by X-Ray Tomography, Annu. Rev. Mater. Res. 42 (2012) 81–103. doi:10.1146/annurev-matsci-070511-155111.

[15] S.S. Singh, J.J. Williams, T.J. Stannard, X. Xiao, F. De Carlo, N. Chawla, Measurement of localized corrosion rates at inclusion particles in AA7075 by in situ three dimensional (3D) X-ray synchrotron tomograpphy, Corros. Sci. 104 (2016) 330–335. doi:http://dx.doi.org/10.1016/j.corsci.2015.12.027.

[16] S.S. Singh, J.J. Williams, X. Xiao, F. De Carlo, N. Chawla, In Situ Three Dimentional (3D) X-Ray Synchrotron Tomography of Corrosion Fatigue in Al7075 Alloy, Fatigue Mater. II Adv. Emergences Underst. (2012) 17–25.

doi:10.1002/9781118533383.ch2.

[17] S.S. Singh, T.J. Stannard, X. Xiao, N. Chawla, In Situ X-ray Microtomography of Stress Corrosion Cracking and Corrosion Fatigue in Aluminum Alloys, Jom. (2017). doi:10.1007/s11837-017-2413-8.

[18] S.S. Singh, J.J. Williams, M.F. Lin, X. Xiao, F. De Carlo, N. Chawla, *In Situ* Investigation of High Humidity Stress Corrosion Cracking of 7075 Aluminum Alloy by Three-Dimensional (3D) X-ray Synchrotron Tomography, Mater. Res. Lett. 2 (2014) 217–220. doi:10.1080/21663831.2014.918907.

[19] S.P. Knight, M. Salagaras, A.M. Wythe, F. De Carlo, A.J. Davenport, A.R. Trueman, In situ X-ray tomography of intergranular corrosion of 2024 and 7050 aluminium alloys, Corros. Sci. 52 (2010) 3855–3860. doi:10.1016/j.corsci.2010.08.026.

[20] S.P. Knight, M. Salagaras, A.R. Trueman, The study of intergranular corrosion in aircraft aluminium alloys using X-ray tomography, Corros. Sci. 53 (2011) 727–734. doi:10.1016/j.corsci.2010.11.005.

[21] S.P. Knight, A.D. Sudholz, A. Butler, S. Palanisamy, M.S. Dargusch, A.R. Trueman, The effect of droplet size on the localized corrosion of high-strength aluminum alloys, Mater. Corros. 67 (2016) 1294–1307. doi:10.1002/maco.201609045.

[22] Properties of Wrought Aluminum and Aluminum Alloys, Properties and Selection: Nonferrous Alloys and Special Purpose Materials, in: ASM Handb., ASM International, Materials Park, OH, 1990: pp. 62–122.

[23] J.R. Davis, ed., ASM Specialty Handbook: Aluminum and Aluminum Alloys, Materials Park, Ohio, 1993.

[24] V.K. Gupta, S.R. Agnew, Fatigue crack surface crystallography near crack initiating particle clusters in precipitation hardened legacy and modern Al-Zn-Mg-Cu alloys, Int. J. Fatigue. 33 (2011) 1159–1174. doi:10.1016/j.ijfatigue.2011.01.018.

[25] S.S. Singh, E. Guo, H. Xie, N. Chawla, Mechanical properties of intermetallic inclusions in Al 7075 alloys by micropillar compression, Intermetallics. 62 (2015) 69–75. doi:10.1016/j.intermet.2015.03.008.

[26] J.T. Staley, Microstructure and toughness of high-strength aluminum alloys, Prop. Relat. to Fract. Toughness. (1976) 71–96.

[27] D.S. Mackenzie, Metallurgy of Heat Treatable Aluminum Alloys, Heat Treating of Nonferrous Alloys, in: ASM Handb., ASM International, Materials Park, Ohio, 2016: pp. 65–113.

[28] W. Callister, D. Rethwisch, Materials science and engineering: an introduction, 2007. doi:10.1016/0025-5416(87)90343-0.

[29] J. Banhart, Age Hardening of Aluminum Alloys Al-Zn-Mg-Cu Alloys Age Hardening of Aluminum Alloys, in: ASM Handb., ASM International, Materials Park, Ohio, 2016: pp. 214–239.

[30] S.K. Maloney, K. Hono, I.J. Polmear, S.P. Ringer, THE CHEMISTRY OF PRECIPITATES IN AN AGED Al-2.1Zn-1 .7Mg at .% ALLOY, Acta Metall. 41 (1999) 1031–1038. doi:10.1016/S1359-6462(99)00253-5.

[31] R. Goswami, S. Lynch, N.J.H. Holroyd, S.P. Knight, R.L. Holtz, Evolution of grain boundary precipitates in Al 7075 upon aging and correlation with stress corrosion cracking behavior, Metall. Mater. Trans. A Phys. Metall. Mater. Sci. 44 (2013) 1268–1278. doi:10.1007/s11661-012-1413-0.

[32] Heat Treating of Aluminum Alloys, Heat Treating, in: ASM Handb., ASM International, Materials Park, OH, 2015: pp. 841–879.

[33] M.C. Reboul, B. Baroux, Metallurgical aspects of corrosion resistance of aluminium alloys, Mater. Corros. 62 (2011) 215–233. doi:10.1002/maco.201005650.

[34] H. Bohni, Breakdown of Passivity and Localized Corrosion Processes, Langmuir. 3 (1987) 924–930. doi:10.1021/la00078a010.

[35] K.D. Ralston, N. Birbilis, M. Weyland, C.R. Hutchinson, The effect of precipitate size on the yield strength-pitting corrosion correlation in Al-Cu-Mg alloys, Acta Mater. 58 (2010) 5941–5948. doi:10.1016/j.actamat.2010.07.010.

[36] J. Soltis, Passivity breakdown, pit initiation and propagation of pits in metallic materials - Review, Corros. Sci. 90 (2015) 5–22. doi:10.1016/j.corsci.2014.10.006.

[37] Z. Szklarska-Smialowska, Pitting corrosion of aluminum, Corros. Sci. 41 (1999) 1743–1767.

[38] K.P. Wong, R.C. Alkire, Local Chemistry and Growth of Single Corrosion Pits in Aluminum, J. Electrochem. Soc. 137 (1990) 3010–3015. doi:10.1149/1.2086150.

[39] E. McCafferty, Sequence of steps in the pitting of aluminum by chloride ions, Corros. Sci. 45 (2003) 1421–1438. doi:10.1016/S0010-938X(02)00231-7.

[40] T. Hagyard, J.R. Williams, Potential of aluminium in aqueous chloride solutions. Part 1, Trans. Faraday Soc. 57 (1961) 2288. doi:10.1039/tf9615702288.

[41] D.A. Vermilyea, Concerning the Critical Pitting Potential, 118 (1970) 529–531.

doi:10.1149/1.2408104.

[42] F.S. Bovard, Environmentally Induced Cracking of an Al-Zn-Mg-Cu Alloy, University of Pittsburgh, 2005.

[43] J.O. Park, Influence of Fe-Rich Intermetallic Inclusions on Pit Initiation on Aluminum Alloys in Aerated NaCl, J. Electrochem. Soc. 146 (1999) 517. doi:10.1149/1.1391637.

[44] P.N.. Unwin, R.. Nicholson, The nucleation and initial stages of growth of grain boundary precipitates in Al-Zn-Mg and Al-Mg alloys, Acta Metall. 17 (1969) 1379–1393. doi:10.1016/0001-6160(69)90155-2.

[45] W. Ren, J. Li, Z. Zheng, W.-J. Chen, Localized corrosion mechanism associated with precipitates containing Mg in Al alloys, Trans. Nonferrous Met. Soc. China. 17 (2007) 727–732.

[46] G. Svenningsen, M.H. Larsen, J.C. Walmsley, J.H. Nordlien, K. Nisancioglu, Effect of artificial aging on intergranular corrosion of extruded AlMgSi alloy with small Cu content, Corros. Sci. 48 (2006) 1528–1543. doi:10.1016/j.corsci.2005.05.045.

[47] F.L. Zeng, Z.L. Wei, J.F. Li, C.X. Li, X. Tan, Z. Zhang, Z.Q. Zheng, Corrosion mechanism associated with Mg 2Si and Si particles in Al-Mg-Si alloys, Trans. Nonferrous Met. Soc. China (English Ed. 21 (2011) 2559–2567. doi:10.1016/S1003-6326(11)61092-3.

[48] K.D. Ralston, N. Birbilis, M.K. Cavanaugh, M. Weyland, B.C. Muddle, R.K.W. Marceau, Role of nanostructure in pitting of Al-Cu-Mg alloys, Electrochim. Acta. 55 (2010) 7834–7842. doi:10.1016/j.electacta.2010.02.001.

[49] N. Birbilis, R.G. Buchheit, Investigation and Discussion of Characteristics for

Intermetallic Phases Common to Aluminum Alloys as a Function of Solution pH, J. Electrochem. Soc. 155 (2008) C117. doi:10.1149/1.2829897.

[50] P.C. King, I.S. Cole, P. a. Corrigan, A.E. Hughes, T.H. Muster, S. Thomas, FIB/SEM study of AA2024 corrosion under a seawater drop, part II, Corros. Sci. 55 (2012) 116–125. doi:10.1016/j.corsci.2011.10.012.

[51] P.C. King, I.S. Cole, P. a. Corrigan, A.E. Hughes, T.H. Muster, FIB/SEM study of AA2024 corrosion under a seawater drop: Part I, Corros. Sci. 53 (2011) 1086–1096. doi:10.1016/j.corsci.2010.12.004.

[52] G.S. Chen, M. Gao, R.P. Wei, Microconstituent-Induced Pitting Corrosion in Aluminum Alloy 2024-T3, Corrosion. 52 (1996) 8–15.

[53] F. Eckermann, T. Suter, P.J. Uggowitzer, A. Afseth, P. Schmutz, The influence of MgSi particle reactivity and dissolution processes on corrosion in Al-Mg-Si alloys, Electrochim. Acta. 54 (2008) 844–855. doi:10.1016/j.electacta.2008.05.078.

[54] N. Birbilis, M.K. Cavanaugh, R.G. Buchheit, Electrochemical behavior and localized corrosion associated with Al7Cu2Fe particles in aluminum alloy 7075-T651, Corros. Sci. 48 (2006) 4202–4215. doi:10.1016/j.corsci.2006.02.007.

[55] R.G. Buchheit, A Compilation of Corrosion Potentials Reported for Intermetallic Phases in Aluminum Alloys, J. Electrochem. Soc. 142 (1995) 3994–3996.

[56] R.K. Gupta, N.L. Sukiman, K.M. Fleming, M.A. Gibson, N. Birbilis, Electrochemical Behavior and Localized Corrosion Associated with Mg2Si Particles in Al and Mg Alloys, ECS Electrochem. Lett. 1 (2012) C1–C3. doi:10.1149/2.002201eel.

[57] W. Tian, S. Li, B. Wang, J. Liu, M. Yu, Pitting corrosion of naturally aged AA 7075 aluminum alloys with bimodal grain size, Corros. Sci. 113 (2016) 1–16.

doi:10.1016/j.corsci.2016.09.013.

[58] P.S. Pao, S.J. Gill, C.R. Feng, ON FATIGUE CRACK INITIATION FROM CORROSION PITS IN 7075-T7351 ALUMINUM ALLOY, Scr. Mater. 43 (2000) 391–396.

[59] G.L. Song, A. Atrens, Corrosion Mechanisms of Magnesium Alloys, Adv. Eng. Mater. 1 (1999) 11–33.

[60] G. Song, D.S.T. John, J. Nairn, the Anodic Dissolution of Magnesium and Sulphate Solutions in Chloride, Corros. Sci. 39 (1997) 1981–2004. doi:http://dx.doi.org/10.1016/S0010-938X(97)00090-5.

[61] S.S. Singh, J.J. Loza, A.P. Merkle, N. Chawla, Three dimensional microstructural characterization of nanoscale precipitates in AA7075-T651 by focused ion beam (FIB) tomography, Mater. Charact. 118 (2016) 102–111. doi:10.1016/j.matchar.2016.05.009.

[62] S.P. Knight, N. Birbilis, B.C. Muddle, A.R. Trueman, S.P. Lynch, Correlations between intergranular stress corrosion cracking, grain-boundary microchemistry, and grain-boundary electrochemistry for Al-Zn-Mg-Cu alloys, Corros. Sci. 52 (2010) 4073–4080. doi:10.1016/j.corsci.2010.08.024.

[63] T. Marlaud, a. Deschamps, F. Bley, W. Lefebvre, B. Baroux, Influence of alloy composition and heat treatment on precipitate composition in Al–Zn–Mg–Cu alloys, Acta Mater. 58 (2010) 248–260. doi:10.1016/j.actamat.2009.09.003.

[64] X.Y. Sun, B. Zhang, H.Q. Lin, Y. Zhou, L. Sun, J.Q. Wang, E.H. Han, W. Ke, Atom probe tomographic study of elemental segregation at grain boundaries for a peak-aged Al-Zn-Mg alloy, Corros. Sci. 79 (2014) 1–4. doi:10.1016/j.corsci.2013.10.027.

[65] X.Y. Sun, B. Zhang, H.Q. Lin, Y. Zhou, L. Sun, J.Q. Wang, E.H. Han, W. Ke, Correlations between stress corrosion cracking susceptibility and grain boundary microstructures for an Al-Zn-Mg alloy, Corros. Sci. 77 (2013) 103–112. doi:10.1016/j.corsci.2013.07.032.

[66] K.D. Ralston, D. Fabijanic, N. Birbilis, Effect of grain size on corrosion of high purity aluminium, Electrochim. Acta. 56 (2011) 1729–1736. doi:10.1016/j.electacta.2010.09.023.

[67] N. Birbilis, Y.M. Zhu, S.K. Kairy, M.A. Glenn, J.F. Nie, A.J. Morton, Y. Gonzalez-Garcia, H. Terryn, J.M.C. Mol, A.E. Hughes, A closer look at constituent induced localised corrosion in Al-Cu-Mg alloys, Corros. Sci. 113 (2016) 160–171. doi:10.1016/j.corsci.2016.10.018.

[68] M. Yasuda, Pitting Corrosion of Al and Al-Cu Single Crystals, J. Electrochem. Soc. 137 (1990) 3708. doi:10.1149/1.2086291.

[69] B.W. Davis, P.J. Moran, P.M. Natishan, Metastable pitting behavior of aluminum single crystals, Corros. Sci. 42 (2000) 2187–2192. doi:10.1016/S0010-938X(00)00032-9.

[70] S. Dey, S.K. Das, A. Basumallick, I. Chattoraj, The effect of pitting on fatigue lives of peak-aged and overaged 7075 aluminum alloys, Metall. Mater. Trans. A Phys. Metall. Mater. Sci. 41 (2010) 3297–3307. doi:10.1007/s11661-010-0395-z.

[71] P.S. Pao, S.J. Gill, C.R. Feng, on Fatigue Crack Initiation From Corrosion Pits in 7075-T7351 Aluminum Alloy, 43 (2000) 391–396.

[72] P.S. Pao, C.R. Feng, S.J. Gill, Corrosion Fatigue Crack Initiation in Aluminum Alloys 7075 and 7050, (2000) 1022–1031. doi:10.5006/1.3294379.

[73] T.D. Burleigh, The Postulated Mechanisms for Stress Corrosion Cracking of

Aluminum Alloys A Review of the Literature 1980-1989, (1991) 89–98.

[74] N.J.H. Holroyd, G.M. Scamans, Crack Propagation During Sustained-Load Cracking of Al-Zn-Mg-Cu Aluminum Alloys Exposed to Moist Air or Distilled Water, Metall. Mater. Trans. A. 42 (2011) 3979–3998. doi:10.1007/s11661-011-0793-x.

[75] J.T. Burns, S. Kim, R.P. Gangloff, Effect of corrosion severity on fatigue evolution in Al-Zn-Mg-Cu, Corros. Sci. 52 (2010) 498–508. doi:10.1016/j.corsci.2009.10.006.

[76] P.S. Pao, R.L. Holtz, NRL/MR/6355--14-9582 Corrosion-Fatigue Cracking in Al 7075 Alloys, Washington, DC, 2014.

[77] K.K. Sankaran, R. Perez, K.V. Jata, Effects of pitting corrosion on the fatigue behavior of aluminum alloy 7075-T6: modeling and experimental studies, Mater. Sci. Eng. A. 297 (2001) 223–229. doi:10.1016/S0921-5093(00)01216-8.

[78] S.P. Lynch, Environmentally assisted cracking: Overview of evidence for an adsorption-induced localised-slip process, Acta Metall. 36 (1988) 2639–2661. doi:10.1016/0001-6160(88)90113-7.

[79] S.P. Lynch, Hydrogen embrittlement phenomena and mechanisms, Corros. Rev. 30 (2012) 105–123.

[80] R. Byrnes, N. Goldsmith, M. Knop, S. Lynch, Corrosion-Fatigue Crack Growth in Age-Hardened Al Alloys: Examples of Failures and Explanations for Fractographic Observations, Adv. Mater. Res. 891–892 (2014) 248–253. doi:10.4028/www.scientific.net/AMR.891-892.248.

[81] R.M. Pelloux, R.E. Stoltz, J.A. Moskovitz, Corrosion fatigue, Mater. Sci. Eng. A. 25 (1976) 193–200.

[82] K.R. Cooper, R.G. Kelly, Crack tip chemistry and electrochemistry of environmental cracks in AA 7050, Corros. Sci. 49 (2007) 2636–2662. doi:10.1016/j.corsci.2006.12.001.

[83] A.J. Sedriks, J.A.S. Green, D.L. Novak, On the chemistry of the solution at the tips of stress corrosion cracks in Al alloys, Corrosion. 27 (1971) 198–202.

[84] B.F. Brown, C.T. Fujii, E.P. Dahlberg, Methods for Studying the Solution Chemistry Within Stress Corrosion Cracks, J. Electrochem. Soc. 116 (1969) 218. doi:10.1149/1.2411799.

[85] Y. Xue, H. El Kadiri, M.F. Horstemeyer, J.B. Jordon, H. Weiland, Micromechanisms of multistage fatigue crack growth in a high-strength aluminum alloy, Acta Mater. 55 (2007) 1975–1984. doi:10.1016/j.actamat.2006.11.009.

[86] J. Payne, G. Welsh, R.J. Christ, J. Nardiello, J.M. Papazian, Observations of fatigue crack initiation in 7075-T651, Int. J. Fatigue. 32 (2010) 247–255. doi:10.1016/j.ijfatigue.2009.06.003.

[87] D.G. Harlow, J. Nardiello, J. Payne, The effect of constituent particles in aluminum alloys on fatigue damage evolution: Statistical observations, Int. J. Fatigue. 32 (2010) 505–511. doi:10.1016/j.ijfatigue.2009.02.036.

[88] A.M. Products, Alcoa Mill Products Alloy 7075 Plate and Sheet Highest Toughness / Strength, (n.d.).

[89] Alcoa Mill Products Alloy 7475 Plate and Sheet Highest Toughness / Strength, n.d.

[90] S. Kim, J.T. Burns, R.P. Gangloff, Fatigue crack formation and growth from localized corrosion in Al-Zn-Mg-Cu, Eng. Fract. Mech. 76 (2009) 651–667. doi:10.1016/j.engfracmech.2008.11.005.

[91] K. Van Der Walde, J.R. Brockenbrough, B.A. Craig, B.M. Hillberry, Multiple fatigue crack growth in pre-corroded 2024-T3 aluminum, Int. J. Fatigue. 27 (2005) 1509–1518. doi:10.1016/j.ijfatigue.2005.06.026.

[92] K. van der Walde, B.M. Hillberry, Initiation and shape development of corrosion-nucleated fatigue cracking, Int. J. Fatigue. 29 (2007) 1269–1281. doi:10.1016/j.ijfatigue.2006.10.010.

[93] Y. Huang, C. Wei, L. Chen, P. Li, Quantitative correlation between geometric parameters and stress concentration of corrosion pits, Eng. Fail. Anal. 44 (2014) 168–178. doi:10.1016/j.engfailanal.2014.05.020.

[94] D. Najjar, T. Magnin, T.. Warner, Influence of critical surface defects and localized competition between anodic dissolution and hydrogen effects during stress corrosion cracking of a 7050 aluminium alloy, Mater. Sci. Eng. A. 238 (1997) 293–302. doi:10.1016/S0921-5093(97)00369-9.

[95] H.K. Birnbaum, C. Buckley, F. Zeides, E. Sirois, P. Rozenak, S. Spooner, J.S. Lin, Hydrogen in aluminum, 254 (1997) 260–264.

[96] C.E. Buckley, H.K. Birnbaum, Characterization of the charging techniques used to introduce hydrogen in aluminum, 332 (2002) 649–653.

[97] R.P. Gangloff, Hydrogen-assisted Cracking, in: J. Petit, P. Scott, I. Milne, R.O. Ritchie, B. Karihaloo (Eds.), Compr. Struct. Integr. I, Vol. 6, Elsevier Sci, New York, NY, 2003: pp. 31–101.

[98] L.B. Pfeil, The Effect of Occluded Hydrogen on the Tensile Strength of Iron, Proc. R. Soc. A Math. Phys. Eng. Sci. 112 (1926) 182–195. doi:10.1098/rspa.1926.0103.

[99] R.A. Oriani, A Mechanistic Theory of Hydrogen Embrittlement of Steels, Berichte Der Bunsen-Gessellschaft Fur Phys. Chemie. 76 (1972) 848–857.

[100] A.R. Troiano, The Role of Hydrogen and Other Interstitials in the Mechanical Behavior of Metals: (1959 Edward De Mille Campbell Memorial Lecture), Metallogr. Microstruct. Anal. 5 (2016) 557–569. doi:10.1007/s13632-016-0319-4.

[101] W.H. Johnson, On Some Remarkable Changes Produced in Iron and Steel by the Action of Hydrogen and Acids, Proc. R. Soc. London. 23 (1874) 168–179. doi:10.1098/rspl.1874.0024.

[102] C.D. Beachem, A New Model for Hydrogen-Assisted Cracking, Metall. Mater. Trans. A. 3 (1972) 437–455.

[103] P.J. Ferreira, I.M. Robertson, H.K. Birnbaum, HYDROGEN EFFECTS ON THE CHARACTER OF DISLOCATIONS IN HIGH-PURITY ALUMINUM, Acta Mater. 47 (1999) 2991–2998.

[104] I.M. Robertson, The effect of hydrogen on dislocation dynamics, Eng. Frac. 64 (1999) 649–673.

[105] I.M. Robertson, P.J. Ferreira, R. Hull, E.A. Stach, Visualizing the Behavior of Dislocations — Seeing Is Believing, MRS Bull. 33 (2008) 122–131.

[106] G.M. Bond, I.M. Robertson, H.K. Birnbaum, On the Determination of the Hydrogen Fugacity in an Environmental Cell TEM Facility, Scr. Metall. 20 (1986) 0–5.

[107] S.P. Lynch, ENVIRONMENTALLY ASSISTED CRACKING: OVERVIEW OF EVIDENCE FOR AN ADSORPTION-INDUCED PROCESS, Acta Metall. 36 (1988) 2639–2661.

[108] N.J. Petch, The Lowering of Fracture Stress due to Surface Adsorption, Philos. Mag. 1 (1956) 331–337.

[109] H.K. Birnbaum, P. Sofronis, Hydrogen-enhanced localized plasticity--a mechanism for hydrogen- related fracture, Mater. Sci. Eng. A. 176 (1994) 191–202.

[110] C. Woodward, D. Trinkle, L. Hector, D. Olmsted, Prediction of Dislocation Cores in Aluminum from Density Functional Theory, Phys. Rev. Lett. 100 (2008) 45507. doi:10.1103/PhysRevLett.100.045507.

[111] G. Lu, Q. Zhang, N. Kioussis, E. Kaxiras, Hydrogen-Enhanced Local Plasticity in Aluminum: An Ab Initio Study, Phys. Rev. Lett. 87 (2001) 95501. doi:10.1103/PhysRevLett.87.095501.

[112] P. Sofronis, The Influence of Mobility of Dissolved Hydrogen on the Elastic Response of a Metal, J. Mech. Phys. Solids. 43 (1995) 1385–1407.

[113] P.J. Ferreira, I.M. Robertson, H.K. Birnbaum, Hydrogen effects on the interaction between dislocations, Acta Mater. 46 (1998) 1749–1757. doi:10.1016/S1359-6454(97)00349-2.

[114] A.K. Vasudevan, K. Sadananda, Role of Slip Mode on Stress Corrosion Cracking Behavior, Metall. Mater. Trans. A. 42 (2010) 405–414. doi:10.1007/s11661-010-0471-4.

[115] Burleigh T.D, The postulated mechanisms for stress corrosion cracking of aluminium alloys- a review of the literature 1980-1989, Corrosion. 47 (1991) 89.

[116] N.J.H. Holroyd, G.M. Scamans, Stress Corrosion Cracking in Al-Zn-Mg-Cu Aluminum Alloys in Saline Environments, Metall. Mater. Trans. A. 44 (2012) 1230–1253. doi:10.1007/s11661-012-1528-3.

[117] R.F. Steigerwald, N.D. Greene, The Anodic Dissolution of Binary Alloys, J. Electrochem. Soc. 109 (1962) 1026. doi:10.1149/1.2425230.

[118] C. Wagner, W. Traud, Uner die Deutung von Korrosionsvorgangen durch Uberlagerung von elektrochemischen Teilvorgangen und uber die Potentialbildung an Mischelektroden, Zeitschrift Fur Elektrochemie Und Angew. Phsikalische Chemie. 44 (1938) 391–402.

[119] J. Zahavi, A. Zangvil, M. Metzger, Structure and Stability of Anodic Films Formed on Aluminum Containing Dispersed Al3Fe Phase, J. Electrochem. Soc. 125 (1978) 438–444. doi:10.1149/1.2131469.

[120] W.K. Johnson, Recent Developments in the Pitting Corrosion of Aluminum, Br. Corros. J. 6 (1971) 200–204.

[121] J. Diggle, T. Downie, C. Goulding, Anodic oxide films on aluminum, Chem. Rev. 66 (1969) 365. doi:10.1021/cr60259a005.

[122] K. Nisancioglu, K.Y. Davanger, O. Strandmyr, H. Holtan, Cathodic Behavior of Aluminum in Aqueous Medi, J. Electrochem. Soc. 128 (1981) 1523.

[123] R.C. Newman, C. Healey, Stability, validity, and sensitivity to input parameters of the slip-dissolution model for stress-corrosion cracking, Corros. Sci. 49 (2007) 4040–4050. doi:10.1016/j.corsci.2007.05.001.

[124] R.C. Newman, Developments in the Slip-Dissolution Model of Stress Corrosion Cracking, Corrosion. 50 (1994) 682–686. doi:https://doi.org/10.5006/1.3293544.

[125] N.E.C. Co, J.T. Burns, Effects of macro-scale corrosion damage feature on fatigue crack initiation and fatigue behavior, Int. J. Fatigue. 103 (2017) 234–247. doi:10.1016/j.ijfatigue.2017.05.028.

[126] J.J. Medved, M. Breton, P.E. Irving, Corrosion pit size distributions and fatigue lives - A study of the EIFS technique for fatigue design in the presence of corrosion, Int. J. Fatigue. 26 (2004) 71–80. doi:10.1016/S0142-1123(03)00069-0.

[127] E.J. Tuegel, INVESTIGATION OF THE EFFECT OF CORROSION PITTING ON FATIGUE LIFE OF ALUMINUM STRUCTURE, 2003.

[128] B.R. Crawford, C. Loader, Q. Liu, T.J. Harrison, P.K. Sharp, Can pitting corrosion change the location of fatigue failures in aircraft?, Int. J. Fatigue. 61 (2014) 304–314. doi:10.1016/j.ijfatigue.2013.10.017.

[129] J.J. Williams, Z. Flom, A.A. Amell, N. Chawla, X. Xiao, F. De Carlo, Damage evolution in SiC particle reinforced Al alloy matrix composites by X-ray synchrotron tomography, Acta Mater. 58 (2010) 6194–6205. doi:10.1016/j.actamat.2010.07.039.

[130] J.J. Williams, K.E. Yazzie, N. Connor Phillips, N. Chawla, X. Xiao, F. Carlo, N. Iyyer, M. Kittur, On the Correlation Between Fatigue Striation Spacing and Crack Growth Rate: A Three-Dimensional (3-D) X-ray Synchrotron Tomography Study, Metall. Mater. Trans. A. 42 (2011) 3845–3848. doi:10.1007/s11661-011-0963-x.

[131] T. Nakayama, F. Yuse, Y. Tsubokawa, Direct observation of corrosion fatigue cracks in aluminum alloy using ultra-bright synchrotron radiation, Corros. Sci. 49 (2007) 130–138. doi:10.1016/j.corsci.2006.05.030.

[132] S.S. Singh, J.J. Williams, P. Hruby, X. Xiao, F. De Carlo, N. Chawla, In situ experimental techniques to study the mechanical behavior of materials using X-ray synchrotron tomography, Integr. Mater. Manuf. Innov. 3 (2014) 9. doi:10.1186/2193-9772-3-9.

[133] Y. Nakai, D. Shiozawa, Observations of corrosion pits and cracks in corrosion fatigue of high strength aluminum alloy by computed-tomography using synchrotron radiation, EPJ Web Conf. 6 (2010) 35004. doi:10.1051/epjconf/20100635004.

[134] S.S. Singh, J.J. Williams, T.J. Stannard, X. Xiao, F. De Carlo, N. Chawla, Measurement of Localized Corrosion Rates at Inclusion Particles in AA7075 by in

situ Three Dimensional (3D) X-ray Synchrotron Tomography, Corros. Sci. 104 (2016) 330–335. doi:10.1007/978-3-319-48105-0_2.

[135] B.J. Connolly, D.A. Horner, S.J. Fox, A.J. Davenport, C. Padovani, S. Zhou, A. Turnbull, M. Preuss, N.P. Stevens, T.J. Marrow, J.-Y. Buffiere, E. Boller, A. Groso, M. Stampanoni, X-ray microtomography studies of localised corrosion and transitions to stress corrosion cracking, Mater. Sci. Technol. 22 (2006) 1076–1085. doi:10.1179/174328406X114199.

[136] D.A. Horner, B.J. Connolly, S. Zhou, L. Crocker, A. Turnbull, Novel images of the evolution of stress corrosion cracks from corrosion pits, Corros. Sci. 53 (2011) 3466–3485. doi:10.1016/j.corsci.2011.05.050.

[137] A. Turnbull, Corrosion pitting and environmentally assisted small crack growth., Proc. Math. Phys. Eng. Sci. 470 (2014) 20140254. doi:10.1098/rspa.2014.0254.

[138] G01: Standard Practice for Preparing, Cleaning, and Evaluating Corrosion Test Specimens, in: ASTM International, West Conshoken, PA, n.d.

[139] T. Ohnishi, K. Yoshimura, Corrosion Fatigue of 7075 Aluminum Alloy, J. Japan Inst. Light Met. 37 (1986) 127–133.

[140] S.M. Ghahari, A.J. Davenport, T. Rayment, T. Suter, J.-P. Tinnes, C. Padovani, J. a. Hammons, M. Stampanoni, F. Marone, R. Mokso, In situ synchrotron X-ray micro-tomography study of pitting corrosion in stainless steel, Corros. Sci. 53 (2011) 2684–2687. doi:10.1016/j.corsci.2011.05.040.

[141] D.A. Horner, B.J. Connolly, S. Zhou, L. Crocker, A. Turnbull, Novel images of the evolution of stress corrosion cracks from corrosion pits, Corros. Sci. 53 (2011) 3466–3485. doi:10.1016/j.corsci.2011.05.050.

[142] H. Toda, T. Hidaka, M. Kobayashi, K. Uesugi, a. Takeuchi, K. Horikawa, Growth

behavior of hydrogen micropores in aluminum alloys during high-temperature exposure, Acta Mater. 57 (2009) 2277–2290. doi:10.1016/j.actamat.2009.01.026.

[143] H. Toda, S. Yamamoto, M. Kobayashi, K. Uesugi, H. Zhang, Direct measurement procedure for three-dimensional local crack driving force using synchrotron X-ray microtomography, Acta Mater. 56 (2008) 6027–6039. doi:10.1016/j.actamat.2008.08.022.

[144] H. Toda, E. Maire, S. Yamauchi, H. Tsuruta, T. Hiramatsu, M. Kobayashi, In situ observation of ductile fracture using X-ray tomography technique, Acta Mater. 59 (2011) 1995–2008. doi:10.1016/j.actamat.2010.11.065.

[145] J.J. Williams, K.E. Yazzie, E. Padilla, N. Chawla, X. Xiao, F. De Carlo, Understanding fatigue crack growth in aluminum alloys by in situ X-ray synchrotron tomography, Int. J. Fatigue. 57 (2013) 79–85. doi:10.1016/j.ijfatigue.2012.06.009.

[146] H. Toda, I. Sinclair, J.-Y. Buffière, E. Maire, T. Connolley, M. Joyce, K.H. Khor, P. Gregson, Assessment of the fatigue crack closure phenomenon in damage-tolerant aluminium alloy by *in-situ* high-resolution synchrotron X-ray microtomography, Philos. Mag. 83 (2003) 2429–2448. doi:10.1080/1478643031000115754.

[147] A. King, G. Johnson, D. Engelberg, W. Ludwig, J. Marrow, Observations of Intergranular stress corrosion cracking in a grain-mapped polycrystal, Science (80-.). 321 (2008) 382–386.

[148] J.J. Williams, K.E. Yazzie, E. Padilla, N. Chawla, X. Xiao, F. De Carlo, Understanding fatigue crack growth in aluminum alloys by in situ X-ray synchrotron tomography, Int. J. Fatigue. 57 (2013) 79–85. doi:10.1016/j.ijfatigue.2012.06.009.

[149] F. De Carlo, B. Tieman, High-Throughput X-ray Microtomography System at the

Advanced Photon Source Beamline 2-BM, in: Dev. X-Ray Tomogr. IV, 2004: pp. 644–651. doi:10.1117/12.559223.

[150] D. Gursoy, F. De Carlo, X. Xiao, C. Jacobsen, TomoPy: A framework for the analysis of synchrotron tomographic data, J. Synchrotron Radiat. 21 (2014) 1188–1193. doi:10.1107/S1600577514013939.

[151] J. Schindelin, I. Arganda-carreras, E. Frise, V. Kaynig, M. Longair, T. Pietzsch, S. Preibisch, C. Rueden, S. Saalfeld, B. Schmid, J. Tinevez, D.J. White, V. Hartenstein, K. Eliceiri, P. Tomancak, A. Cardona, Fiji : an open-source platform for biological-image analysis, 9 (2012). doi:10.1038/nmeth.2019.

[152] R. Adams, L. Bischof, Seeded region growing - Pattern Analysis and Machine Intelligence, IEEE Transactions on, 16 (1994) 641–647.

[153] S.P. Knight, K. Pohl, N.J.H. Holroyd, N. Birbilis, P.A. Rometsch, B.C. Muddle, R. Goswami, S.P. Lynch, Some effects of alloy composition on stress corrosion cracking in Al-Zn-Mg-Cu alloys, Corros. Sci. 98 (2015) 50–62. doi:10.1016/j.corsci.2015.05.016.

[154] I.S. Raju, J.C. Newman, Stress-Intensity Factors for Circumferential Surface Cracks in Pipes and Rods under Tension and Bending Loads, Fract. Mech. ASTM STP 905. 17 (1986) 789–805.

[155] N. Takano, Hydrogen diffusion and embrittlement in 7075 aluminum alloy, 484 (2008) 336–339. doi:10.1016/j.msea.2006.08.144.

[156] S. Lynch, Hydrogen embrittlement phenomena and mechanisms, Corros. Rev. 30 (2012) 105–123. doi:10.1515/corrrev-2012-0502.

[157] I.M. Robertson, H.K. Birnbaum, HYDROGEN EFFECTS ON THE INTERACTION BETWEEN DISLOCATIONS, 46 (1998) 1749–1757.

[158] I.M. Robertson, The e € ect of hydrogen on dislocation dynamics q , qq, 65 (2001) 671–692.

[159] Y. Liang, P. Sofronis, N. Aravas, On the effect of hydrogen on plastic instabilities in metals, Acta Mater. 51 (2003) 2717–2730. doi:10.1016/S1359-6454(03)00081-8.

[160] G.O. Ilevbare, O. Schneider, J.R. Scully, R.G. Kelly, In Situ Confocal Laser Scanning Microscopy of AA 2024-T3 Corrosion Metrology I. Localized Corrosion of Particles, J. Electrochem. Soc. 151 (2004) B453. doi:10.1149/1.1764781.

[161] O. Schneider, G.O. Ilevbare, J.R. Scully, R.G. Kelly, In Situ Confocal Laser Scanning Microscopy of AA 2024-T3 Corrosion Metrology II. Trench Formation Around Particles, J. Electrochem. Soc. 151 (2004) B465. doi:10.1149/1.1764781.

[162] C. Larignon, J. Alexis, E. Andrieu, G. Odemer, C. Blanc, Propagation of Intergranular Corrosion Defects in AA 2024-T351 Evaluated by a Decrease in Mechanical Resistance, J. Electrochem. Soc. 161 (2014) C339–C348. doi:10.1149/2.090406jes.

[163] C.-M. Liao, J.M. Olive, M. Gao, R.P. Wei, In-Situ Monitoring of Pitting Corrosion in Aluminum Alloy 2024, Corrosion. 54 (1998) 451–458. doi:10.5006/1.3284873.

[164] Y. Yang, H.G. Zheng, Z.J. Shi, Q.M. Zhang, Effect of orientation on self-organization of shear bands in 7075 aluminum alloy, Mater. Sci. Eng. A. 528 (2011) 2446–2453. doi:10.1016/j.msea.2010.12.050.

[165] T.J. Stannard, H.A. Bale, N. Gueninchault, J.J. Williams, A.P. Merkle, E. Lauridsen, N. Chawla, Three dimensional time-resolved quantification of inclusion and grain boundary effects on corrosion pit evolution in an aerospace aluminum alloy, Prep. (2017).

[166] M.T. Benediktsson, K.K.G. Mýrdal, P. Maurya, A. Pedersen, Stability and mobility of vacancy-H complexes in Al., J. Phys. Condens. Matter. 25 (2013) 375401. doi:10.1088/0953-8984/25/37/375401.

[167] G. Song, A. Atrens, D. StJohn, J. Nairn, Y. Li, The electrochemical corrosion of pure magnesium in 1N NaCl, Corros. Sci. 39 (1997) 855–875.

[168] T.J. Stannard, J.J. Williams, S.S. Singh, A.S.S. Singaravelu, X. Xiao, N. Chawla, 3D Time-Resolved Observations of Fatigue Crack Initiation and Growth from Corrosion Pits in Al7075 Alloys Using Synchrotron X-ray Tomography Tyler Stannard, Submitted. (2017).

[169] T. Ohnishi, K. Yoshimura, Effects of Orientation of Specimen on Fatigue and Corrosion Fatigue Properties in 7475 Aluminum Alloy, J. Japan Inst. Light Met. 37 (1987) 277–284.

[170] Z. Ren, M. Ulbin, B. Zafošnik, Z. Ren, M. Ulbin, J. Flašker, Evaluation of stress intensity factors using finite elements, Lab. Comput. Aided Eng. Fac. Mech. Eng. Univ. Maribor, Maribor, Slov. (2000).

[171] J.T. Burns, J.M. Larsen, R.P. Gangloff, Driving forces for localized corrosion-to-fatigue crack transition in Al-Zn-Mg-Cu, Fatigue Fract. Eng. Mater. Struct. 34 (2011) 745–773. doi:10.1111/j.1460-2695.2011.01568.x.

[172] Y. Li, L. Kovarik, P.J. Phillips, Y.-F. Hsu, W.-H. Wang, M.J. Mills, High-resolution characterization of the precipitation behavior of an Al – Zn – Mg – Cu alloy, Philos. Mag. Lett. 92 (2012) 166–178.

[173] A. Deschamps, A. Bigot, F. Livet, P. Auger, Y. Brechet, D. Blavette, A Comparative Study of Precipitate Composition and Volume Fraction in an Al–Zn–Mg Alloy using Tomographic Atom Probe and Small-Angle X-ray Scattering, Philos. Mag. A. 81 (2001) 2391–2414. doi:10.1080/01418610110038439.

[174] W. Lefebvre, F. Danoix, G. Da Costa, F. De Geuser, H. Hallem, A. Deschamps, M. Dumont, 3DAP measurements of Al content in different types of precipitates in aluminium alloys, Surf. Interface Anal. 39 (2007) 206–212. doi:10.1002/sia.2516.

[175] M. Dumont, W. Lefebvre, B. Doisneau-Cottignies, A. Deschamps, Characterisation of the composition and volume fraction of η′ and η precipitates in an Al-Zn-Mg alloy by a combination of atom probe, small-angle X-ray scattering and transmission electron microscopy, Acta Mater. 53 (2005) 2881–2892. doi:10.1016/j.actamat.2005.03.004.

[176] T. Engdahl, V. Hansen, P.J. Warren, K. Stiller, Investigation of fine scale precipitates in Al – Zn – Mg alloys after various heat treatments, Mater. Sci. Eng. A. 327 (2002) 59–64.

[177] C.J.S. J. Gjønnes†, An electron microscope investigation of the microstructure in an aluminum-zinc-magnesium alloy, Acta Metall. 18 (1970) 881–890.

[178] T. Marlaud, A. Deschamps, F. Bley, W. Lefebvre, B. Baroux, Influence of alloy composition and heat treatment on precipitate composition in Al – Zn – Mg – Cu alloys, Acta Mater. 58 (2010) 248–260. doi:10.1016/j.actamat.2009.09.003.

[179] A. Turnbull, The environmentally small/short crack growth effect: Current understanding, Corros. Rev. 30 (2012) 1–17. doi:10.1515/corrrev-2012-0003.

[180] R.O. Ritchie, M. Engineering, J. Lankford, S. Antonio, - ~~~ k t h rl s hol d log L ~ K , o, 84 (1986) 11–16.

[181] J. Petit, C. Sarrazinbaudoux, An overview on the influence of the atmosphere environment on ultra-high-cycle fatigue and ultra-slow fatigue crack propagation, Int. J. Fatigue. 28 (2006) 1471–1478. doi:10.1016/j.ijfatigue.2005.06.057.

[182] W. Schaef, M. Marx, H. Vehoff, A. Heckl, P. Randelzhofer, A 3-D view on the

mechanisms of short fatigue cracks interacting with grain boundaries, Acta Mater. 59 (2011) 1849–1861. doi:10.1016/j.actamat.2010.11.051.

[183] A.K. Vasudevan, K. Sadananda, Role of slip mode on stress corrosion cracking behavior, Metall. Mater. Trans. A Phys. Metall. Mater. Sci. 42 (2011) 405–414. doi:10.1007/s11661-010-0471-4.

[184] R.G. Song, W. Dietzel, B.J. Zhang, W.J. Liu, M.K. Tseng, a. Atrens, Stress corrosion cracking and hydrogen embrittlement of an Al–Zn–Mg–Cu alloy, Acta Mater. 52 (2004) 4727–4743. doi:10.1016/j.actamat.2004.06.023.

[185] H.K. Birnbaum, G.M. Bond, I.M. Robertson, The influence of hydrogen on deformation and fracture processes in high-strength aluminum alloys, Acta Metall. 35 (1987) 2289–2296.

[186] J.S. Warner, R.P. Gangloff, Alloy induced inhibition of fatigue crack growth in age-hardenable Al-Cu Alloys, Int. J. Fatigue. 42 (2012) 35–44. doi:10.1016/j.ijfatigue.2011.04.013.

[187] J.T. Burns, J.M. Larsen, R.P. Gangloff, Effect of initiation feature on microstructure-scale fatigue crack propagation in Al-Zn-Mg-Cu, Int. J. Fatigue. 42 (2012) 104–121. doi:10.1016/j.ijfatigue.2011.08.001.

[188] K.M. Gruenberg, B.A. Craig, B.M. Hillberry, R.J. Bucci, A.J. Hinkle, Predicting fatigue life of pre-corroded 2024-T3 aluminum, Int. J. Fatigue. 26 (2004) 629–640. doi:10.1016/j.ijfatigue.2003.10.011.

[189] A. Boag, A.E. Hughes, A.M. Glenn, T.H. Muster, D. McCulloch, Corrosion of AA2024-T3 Part I: Localised corrosion of isolated IM particles, Corros. Sci. 53 (2011) 17–26. doi:10.1016/j.corsci.2010.09.009.

[190] A.E. Hughes, A. Boag, A.M. Glenn, D. McCulloch, T.H. Muster, C. Ryan, C. Luo,

X. Zhou, G.E. Thompson, Corrosion of AA2024-T3 Part II: Co-operative corrosion, Corros. Sci. 53 (2011) 27–39. doi:10.1016/j.corsci.2010.09.030.

[191] A.M. Glenn, T.H. Muster, C. Luo, X. Zhou, G.E. Thompson, A. Boag, A.E. Hughes, Corrosion of AA2024-T3 Part III: Propagation, Corros. Sci. 53 (2011) 40–50. doi:10.1016/j.corsci.2010.09.035.

[192] G.S. Chen, K.-C. Wan, M. Gao, R.P. Wei, T.H. Flournoy, Transition from pitting to fatigue crack growth—modeling of corrosion fatigue crack nucleation in a 2024-T3 aluminum alloy, Mater. Sci. Eng. A. 219 (1996) 126–132. doi:10.1016/S0921-5093(96)10414-7.

[193] E. Linardi, R. Haddad, L. Lanzani, Stability Analysis of the Mg2Si Phase in AA 6061 Aluminum Alloy, Procedia Mater. Sci. 1 (2012) 550–557. doi:10.1016/j.mspro.2012.06.074.

[194] S.S. Singh, J.J. Loza, A.P. Merkle, N. Chawla, Three dimensional microstructural characterization of nanoscale precipitates in AA7075-T651 by focused ion beam (FIB) tomography, Mater. Charact. 118 (2016) 102–111. doi:10.1016/j.matchar.2016.05.009.

[195] J.K. Park, A.J. Ardell, Microchemical analysis of precipitate free zones in 7075-A1 in the T6, T7 and RRA tempers, Acta Metall. Mater. 39 (1991) 591–598. doi:10.1016/0956-7151(91)90127-M.

[196] D.J. Jensen, E.M. Lauridsen, L. Margulies, H.F. Poulsen, S. Schmidt, H.O. Sørensen, G.B.M. Vaughan, X-ray microscopy in four dimensions, Mater. Today. 9 (2006) 18–25. doi:10.1016/S1369-7021(05)71334-1.

[197] S.A. Mcdonald, P. Reischig, C. Holzner, E.M. Lauridsen, P.J. Withers, A.P. Merkle, Non-destructive mapping of grain orientations in 3D by laboratory X-ray microscopy, Nat. Publ. Gr. (n.d.) 1–11. doi:10.1038/srep14665.

[198] S.A. Mcdonald, C. Holzner, E.M. Lauridsen, P. Reischig, A.P. Merkle, P.J. Withers, Microstructural evolution during sintering of copper particles studied by laboratory diffraction contrast tomography (LabDCT), Sci. Rep. 7 (2017) 5251. doi:10.1038/s41598-017-04742-1.

[199] A. King, P. Reischig, J. Adrien, S. Peetermans, W. Ludwig, Polychromatic diffraction contrast tomography, Mater. Charact. 97 (2014) 1–10. doi:10.1016/j.matchar.2014.07.026.

[200] A. King, W. Ludwig, M. Herbig, J.Y. Buffire, A.A. Khan, N. Stevens, T.J. Marrow, Three-dimensional in situ observations of short fatigue crack growth in magnesium, Acta Mater. 59 (2011) 6761–6771. doi:10.1016/j.actamat.2011.07.034.

[201] G. Johnson, A. King, M.G. Honnicke, J. Marrow, W. Ludwig, X-ray diffraction contrast tomography: A novel technique for three-dimensional grain mapping of polycrystals. II. The combined case, J. Appl. Crystallogr. 41 (2008) 310–318. doi:10.1107/S0021889808001726.

[202] A.D. Spear, S.F. Li, J.F. Lind, R.M. Suter, A.R. Ingraffea, Three-dimensional characterization of microstructurally small fatigue-crack evolution using quantitative fractography combined with post-mortem X-ray tomography and high-energy X-ray diffraction microscopy, Acta Mater. 76 (2014) 413–424. doi:10.1016/j.actamat.2014.05.021.

[203] M. Herbig, A. King, P. Reischig, H. Proudhon, E.M. Lauridsen, J. Marrow, J.Y. Buffire, W. Ludwig, 3-D growth of a short fatigue crack within a polycrystalline microstructure studied using combined diffraction and phase-contrast X-ray tomography, Acta Mater. 59 (2011) 590–601. doi:10.1016/j.actamat.2010.09.063.

[204] H.F. Poulsen, S.F. Nielsen, E.M. Lauridsen, S. Schmidt, R.M. Suter, U. Lienert, T. Lorentzen, D.J. Jensen, Three-dimensional maps of grain boundaries and the stress state of individual grains in polycrystals and powders, J. Appl. Crystallogr. 34 (2001) 751–756.

[205] R.C. Dorward, K.R. Hasse, K. Aluminium, C. Corp, The Fractography of Long-Transverse Stress Corrosion Cracking in Al-Zn-Mg Cu Alloys, Corrosion. 22 (1982) 251–257.

[206] X. Liu, G.S. Frankel, B. Zoofan, S.I. Rokhlin, Transition from Intergranular Corrosion to Intergranular Stress Corrosion Cracking in AA2024-T3, J. Electrochem. Soc. 153 (2006) B42. doi:10.1149/1.2142288.

[207] R. Goswami, S. Lynch, N.J.H. Holroyd, S.P. Knight, R.L. Holtz, Evolution of Grain Boundary Precipitates in Al 7075 Upon Aging and Correlation with Stress Corrosion Cracking Behavior, Metall. Mater. Trans. A. 44 (2012) 1268–1278. doi:10.1007/s11661-012-1413-0.